Patient Modeling for Simulation Guided Head and Neck Hyperthermia

René Verhaart

Patient Modeling for Simulation Guided Head and Neck Hyperthermia

René Verhaart

Patient Modeling for Simulation Guided Head and Neck Hyperthermia

Patient modellering voor simulatie gestuurde hoofd-hals hyperthermie

Proefschrift

ter verkrijging van de graad van doctor aan de
Erasmus Universiteit Rotterdam
op gezag van de
rector magnificus

Prof.dr. H.A.P. Pols

en volgens besluit van het College voor Promoties.

De openbare verdediging zal plaatsvinden op
dinsdag 4 oktober 2016 om 15:30 uur

door

Renatus Franciscus Verhaart

geboren te Westvoorne

Promotiecommissie

Promotoren:	Prof.dr.ing. G.C. van Rhoon
Overige leden:	Prof.dr. A. van der Lugt
	Prof.dr. B.W. Raaymakers
	Prof.dr. B.J.M. Heijmen
Copromotor:	Dr.ir. M.M. Paulides

Contents

CHAPTER 1

Introduction

1.1   Head and neck cancer

Cancer figure among the leading causes of morbidity and mortality worldwide[3]. Of the patients suffering from cancer worldwide approximately 5% have tumors in the head and neck (H&N) region[1]. In the Netherlands H&N cancer incidence represents approximately 3% of all cancers[2]. H&N cancers are often categorized based on the region in which they originate, resulting in five regions, as illustrated in Figure 1.1:

1. oral cavity

2. pharynx, including the nasopharynx, oropharynx and hypopharynx

3. larynx

4. paranasal sinusus and nasal cavity

5. salivary glands
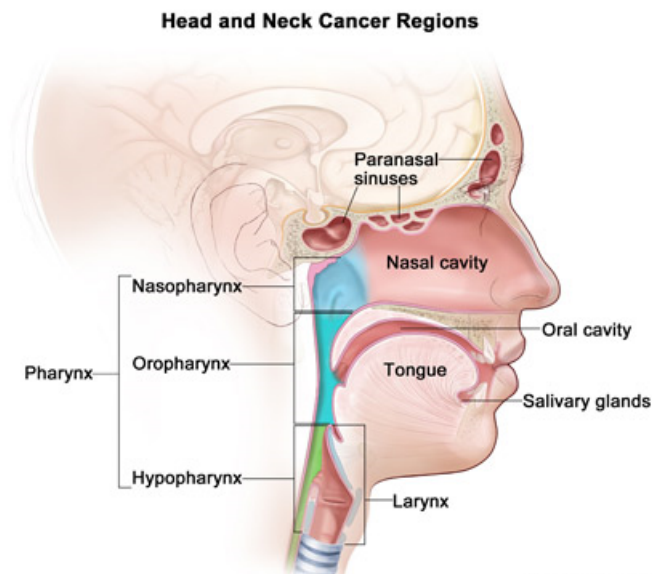
Figure 1.1: Head and neck cancer regions. Image from www.cancer.gov

The prognosis for patients with advanced H&N cancer is very poor and treatment is challenging[18,70]. These patients are standardly treated with radiotherapy with or without chemotherapy. The treatments are associated with a high treatment toxicity. Side effects often reported are loss of swallowing and salivary function leading to difficulties in speaking and eating[18,68].

1.2 Hyperthermia treatment

In a hyperthermia treatment, electromagnetic (EM) energy is transferred into the patient to obtain a therapeutic result. The treatment can be for superficial targets (upto 4 cm depth from the skin surface) or deep targets (deeper than 4 cm from the skin surface), depending on the technique that is used[111]. Deep hyperthermia can be applied in the pelvic region or in the H&N region. The goal of a hyperthermia treatment is to elevate the target temperature to $39-44$°C where the optimum temperature is around 43°C[105]. It is known that hyperthermia causes a number of biological and physiological effects such as DNA repair inhibition and changes in blood flow and oxygenation[11,50,54,58,65]. For multiple tumor sites, clinical studies have shown that the addition of a local hyperthermia treatment to a (chemo)radiation treatment signifcantly improves the treatment outcome without increasing treatment late toxicity[37,57,103]. For H&N hyperthermia, several prospective randomized phase III trials indicate that adding a hyperthermia treatment to the standard (chemo)radiation treatment improves clinical outcome without adding extra toxicity[23,51,53,100,113]. An overview of the findings of these studies for H&N hyperthermia can be found in Table 1.1.

Table 1.1: Overview of phase III clinical trials that show the effect on H&N cancers of adding a hyperthermia treatment to the conventional chemoradiation treatment. CR: complete response, LC: local control, OS: overall survival, RT: radiotherapy, CRT: chemoradiation, HT: hyperthermia, Loc. Adv.: local advanced, SCC: squamous cell carcinoma, Nr. P: Number of patients included in the study.

Study	Nr. P	Tumor	(C)RT	(C)RT only	(C)RT +**HT**	Toxicity
Datta[23]	65	SCC (stage III − IV)	RT	CR: 10%	CR: 50%	−
Valdagni[100]	41	Loc. adv. H&N cancer + N3 nodes	RT	LC(5y): 24% OS(5y): 0%	LC(5y): 69% OS(5y): 54%	Similar
Huilgol[53]	56	Loc. Adv. H&N cancer	RT	CR: 42%	CR: 79%	Similar
Hua[51]	180	Nasopharynx	RT	CR: 81% LC(5y): 79%	CR: 96% LC(5y): 91%	Similar
Zhao[113]	83	Nasopharynx	CRT	OS(3y): 54%	OS(3y): 73%	Similar

In a recent study, the results of these randomized H&N studies as well as several controlled non-randomized trials are summarized[24]. This review reported in a total of 717 patients with H&N cancer a statistical significant difference ($p < 0.001$) in favor of the hyperthermia group, i.e. complete local response was 50.3% (183/364) for (chemo)-radiation versus 75.3% (266/353) for (chemo)-radiation combined with hyperthermia, with an odds ratio of 3.71 (95% confidence interval, 2.55 - 5.38). This means that the probability of a

local response in a (chemo)-radiation treatment including hyperthermia is 3.71x higher compared to probability of a local response in a (chemo)-radiation treatment without hyperthermia. For H&N cancers, Zhao et al. also reports an improvement in quality of life and overall survival when using hyperthermia[113]. These findings plea for the addition of hyperthermia to a H&N (chemo)-radiation treatment.

For long, heating of H&N tumors was only possible at superficial locations. In 2007, the Erasmus MC developed the first hyperthermia applicator for the treatment of deep H&N cancers[78]. With this applicator it was possible to heat tumors deeper than 4 cm from the skin surface, using EM waves originating from multiple antenna elements[79]. This applicator was called the HYPERcollar of which images are shown in Figure 1.2a and 1.2b. Note that all the work in this thesis is done for the HYPERcollar, since at the time of the research all patients were treated with that applicator. Recently, an improved version of the HYPERcollar is developed called HYPERcollar3D[90,99] as shown in Figure 1.2c. However, since the HYPERcollar3D can heat target regions even more conformal and precise, the impact of the work described in this thesis for this device will be even greater.

(a) (b) (c)
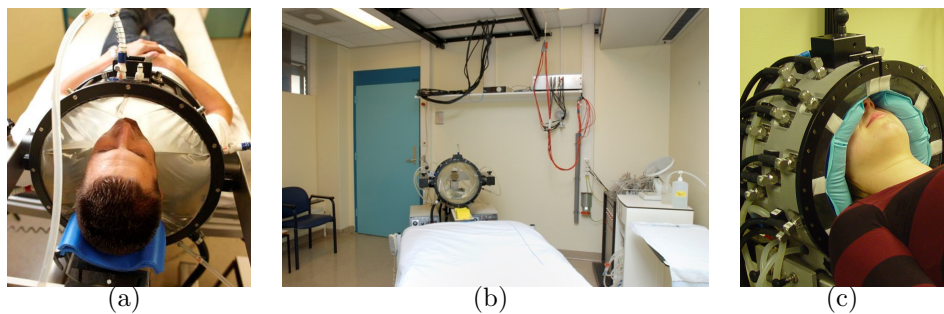
Figure 1.2: The HYPERcollar(a), the treatment room(b) and the HYPERcollar3D(c)

1.3 Hyperthermia treatment planning (HTP)

1.3.1 HTP rationale

The development of the HYPERcollar resulted in the technological possibility of heating deeply seated tumors in the H&N region. The clinical use of the HYPERcollar requires hyperthermia treatment planning (HTP) for multiple reasons. First, the H&N region includes many thermosensitive tissues in which the temperature increase should remain under specific thresholds, like 40ºC for the spinal cord[48]. Second, the H&N region includes many different tissues and since each tissue affects the EM and temperature distribution differently, HTP is crucial for an accurate estimation of these distributions. Third, due to the many different tissues there are many tissue transitions that cause heterogeneities in the SAR distribution which can be predicted with HTP. Fourth, the applicator includes

twelve antenna elements from which the EM waves originate. Due to this multi-channel applicator, HTP is required to optimise amplitude and phase settings for each individual channel. Last, dosimetry using thermometry sensors is limited and HTP can give an estimate of the 3D dose distribution. Therefore, in the clinical use of the HYPERcollar, HTP is not only used for pre-treatment and real-time treatment optimization, but also for treatment monitoring, treatment evaluation and tissue dose assessment[79,89].

1.3.2 HTP procedure

In HTP, EM and temperature simulations are used to predict the EM or temperature distribution inside the patient. Input for these simulations is a 3D distribution of the (EM and temperature) tissue properties. In current clinical practise, literature tissue property values are assigned to 3D tissue regions that are segmented from Computed Tomography (CT) or Magnetic Resonance Imaging (MRI) scans. On these scans the normal, critical and target tissues are delineated, which results in a full 3D patient model. This patient model is positioned inside a detailed 3D model of the HYPERcollar applicator such that it matches the actual treatment situation. The EM field for each of the twelve antennas of the HYPERcollar is simulated pretreatment. The amplitude and phase of each antenna is optimized such that the absorbed power, called the specific absorption rate (SAR), is the highest in the target while sparing the normal and critical (thermo-sensitive) tissues from an excessive thermal dose. An illustration of this proces is illustrated in Figure 1.3.
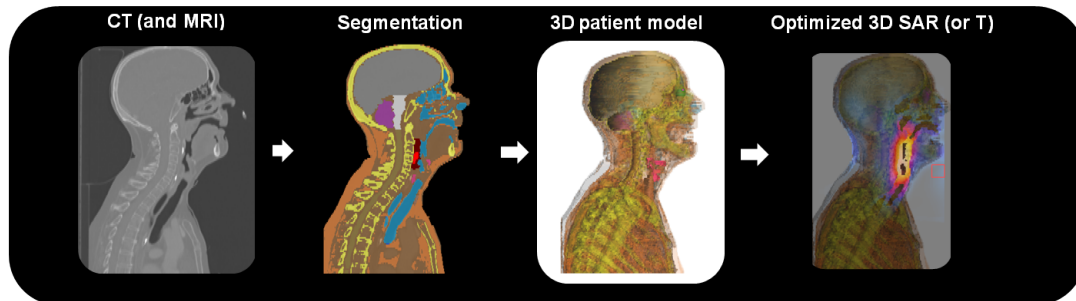
Figure 1.3: The hyperthermia treatment planning proces: start with CT (and MRI) images, delineate the tissues, create a 3D patient model, optimize 3D SAR based on the EM simulations and simulate the 3D temperature (T).

1.3.3 Application of HTP

Hyperthermia treatment planning can be used for many purposes. In the past it was mainly used to design new hyperthermia applicators[78,90,99] or to determine the effect of a parameter on the treatment outcome in sensitivity studies[14,101]. Until recent, it was not standard to use imaging data as input for the treatment plan and therefore general shapes[77] or a model of another patient was used as input[62]. When computer power

increased and images were routinely acquired, patient-specific modeling became the standard. Further developments made it even possible to apply real-time optimisation during treatment in complaint-adaptive hyperthermia[89].

1.3.4 HTP status

At the start of the project, HTP was being used for the treatment of patients with tumors in the H&N region. At that time, 3D patient models for HTP were created using manual and/or semi-automatic procedures for segmenting tissues on CT images. The standard method included Hounsfield unit (HU) based thresholding of muscle, fat and bone tissues while critical tissues were segmented manually. Due to the manual aspect of tissue segmentation, the intra- and interobserver variation affect the accuracy of the patient model. The proces of generating a full 3D patient model of the H&N region took usually about one working day (5-8 hours). The commercially available tool iSeg was used for this proces, which is part of the EM simulation platform SEMCAD X (Schmid & Partner Engineering AG (SPEAG), Zurich, Switzerland). iSeg includes algorithms for manual and semi-automatic segmentation of images. It has more advanced tools compared to the more widely used HTP platform Sigma HyperPlan, that is specifically designed for deep hyperthermia with the commercial BSD 2000 applicator[43].

At the start of this project, no temperature simulations were used for HTP. It was fully based on SAR predictions. For H&N HTP these predictions were done in SEM-CAD X. This platform includes EM and thermal solvers similar to HyperPlan, while also providing some extra functionalities like Discrete Vascular (DIVA) modeling.

1.4 Approach

The aim of this project was the development of accurate and efficient patient model generation for patient-specific HTP based on EM and temperature modeling.

1.4.1 3D patient modeling

The first step in the accurate and efficient patient modeling was the 3D solid model generation. Hereto we developed and validated an atlas-based automatic segmentation tool. This automatic segmentation should replace most of the manual and semi-automatic procedures, reduce the segmentation workload of 5-8 hours, be at least as accurate as manual segmentations but more reproducible since manual segmentations are prone to intra- and interobserver variability. First, the relevant tissues that have to be segmented by the tool were determined. Hereto the following points were considered: 1) the contrast and visibility of the tissue on the image; 2) the relative difference in tissue property values with respect to other tissues; 3) the relevance of the tissue type for the optimization algorithm, i.e. the organs at risk.

To further improve patient model accuracy, we explored the possibility of including MRI information. In radiotherapy treatment planning, MRI has shown to be a useful supplement to the CT data especially for more accurate target[46,88,98] and soft-tissue delineation[5,42]. Using MRI still requires CT images as they are geometrically more accurate than MRI and they provide crucial proton density information for radiotherapy treatment planning. Typically, the requirements for the detail of segmentation for hyperthermia are higher than, for example, in radiotherapy, as more tissues need to be distinguished to correctly capture the important impact of dielectric and thermal tissue properties. Thus, by combining CT and MRI and introducing sophisticated atlas-based registration and segmentation algorithms[34], the aim was to replace the manual operations and facilitate a fast, accurate and reproducible generation of patient specific patient models for HTP. This is the topic of chapter 2 and 3 of this thesis.

1.4.2 Temperature modeling

The accuracy of the 3D patient model is not only dependent on the location of the tissue obtained from the segmentation tool, but also on the tissue property values that are assigned to the tissues. Hence, a 3D patient model consists of a number of segmented tissues and per tissue a definition of the tissue property values. The accuracy of EM and temperature simulations is dependent on those tissue property values because they can vary between patients, within the patient, within each tissue, over time and as a non-linear function of tissue temperature. Upto now in HTP, EM simulations are used to predict the SAR in the patient. However, since clinical studies have shown that treatment outcome is related to thermal-dose[38,94], we decided in the project to focus on the accuracy improvement of temperature simulations. This is the topic of chapter 4 and 5 of this thesis, where we choose to optimize thermal tissue property values using the input of temperature sensors and simulations.

1.5 Scope and outline of this thesis

The research presented in this thesis is the result of a close collaboration between the Hyperthermia Unit (Erasmus MC - Cancer Institute) and the Biomedical Imaging Group Rotterdam (Erasmus MC - BIGR), which is a cooperation between the departments of Radiology and Medical Informatics. This thesis focuses on one hand on the validation of image processing tools developed for H&N patient model generation from CT and MRI and on the other hand on improving temperature simulations in HTP for H&N cancer patients.

In **chapter 2** the automatic tissue segmentation tool is validated by comparing the impact of manual and automatic normal and critical tissue segmentation on HTP. The impact was evaluated using both the SAR dose distribution and the HTP quality. In addition, the effect of tissue segmentation was compared to other sources of patient model uncertainties, such as the grid step and uncertainties in tissue properties.

In **chapter 3** the relevance of including MRI in addition to CT images for H&N patient modeling is investigated. To quantify this relevance, the predicted maximum temperature and the corresponding SAR in the segmented tissues of CT based patient models were compared to CT and MRI based patient models.

In **chapter 4** the first step in improving temperature simulations for H&N HTP is described. A technique is developed for patient-group specific optimization of thermal tissue properties based on invasively measured temperatures.

In **chapter 5** the technique of chapter 4 is improved further and used to assess the feasibility of 3D dosimetry based on patient-specific temperature simulations and sensory feedback.

In **chapter 6** the general conclusions and future perspectives are provided to finalize the scientific content of the thesis.

CHAPTER 2

CT-based patient modeling:
manual vs. automatic tissue segmentation

Abstract

__Purpose:__ Clinical trials have shown that hyperthermia, as adjuvant to radiotherapy and/or chemotherapy, improves treatment of patients with locally advanced or recurrent head and neck (H&N) carcinoma. In Rotterdam, hyperthermia treatment planning (HTP) guided H&N hyperthermia is being investigated, which requires patient specific 3D patient models derived from Computed Tomography (CT)-images. To decide whether a recently developed automatic-segmentation algorithm can be introduced in the clinic, we compared the impact of manual- and automatic normal-tissue-segmentation variations on HTP quality.

__Materials and methods:__ CT images of seven patients were segmented automatically and manually by four observers, to study inter-observer and intra-observer geometrical variation. To determine the impact of this variation on HTP quality, HTP was performed using the automatic and manual segmentation of each observer, for each patient. This impact was compared to other sources of patient model uncertainties, i.e. varying gridsizes and dielectric tissue properties.

__Results:__ Despite geometrical variations, manual and automatic generated 3D patient models resulted in an equal, i.e. 1%, variation in HTP quality. This variation was minor with respect to the total of other sources of patient model uncertainties, i.e. 11.7%.

__Conclusion:__ Automatically generated 3D patient models can be introduced in the clinic for H&N HTP.

2.1 Introduction

Hyperthermia, i.e. raising tissue temperature to $39-44^{\circ}$C, has been shown to improve clinical outcome when added to radiotherapy or chemotherapy for several tumor sites[37,57,103], including the head and neck[6,51,52]. We recently developed a hyperthermia applicator to investigate the benefit of deep local heating of head and neck tumors[78,79]. The clinical use of this device requires hyperthermia treatment planning (HTP) based on electromagnetic simulations for pre-treatment and real-time treatment optimization and tissue dose assessment. Crucial input for HTP are full 3D patient models incorporating all normal tissues and the gross tumor volume (GTV). These models are generated by segmenting tissue regions on computed tomography (CT) images[80]. We recently developed an automatic-segmentation algorithm for head and neck HTP that has shown to be accurate, reproducible and substantially reduces operator time[34]. A clinical introduction of the algorithm requires a comparison of the impact of automatic segmentation on the hyperthermia treatment quality with the actual clinical standard, which is based on manual segmentations. Manual segmentations are prone to observer variation, and the patient model influences the accuracy of HTP for deep hyperthermia in the pelvic region[15,110]. Due to the large number of small tissue regions in the head and neck region, observer variation in tissues segmentation may have a substantial impact on the hyperthermia treatment quality, but, this impact has never been quantified.

CT-based observer variation in tissue segmentation has already been assessed for head and neck radiotherapy treatment planning[12,74]. However, while HTP requires a full 3D patient model, these studies included only a limited number of tissues, and many reported either inter-observer or intra-observer variation. But, although not complete, these studies provide an excellent reference to compare the results for separate organs.

Assessments of the exposure by electromagnetic sources of the human body also involve 3D human models. These studies often summarize causes of simulation uncertainties in an uncertainty budget, which includes uncertainties such as variations in dielectric tissue properties and variations in the gridsize[7,73]. Observer dependent tissue segmentation might also influence the simulated electromagnetic field, however this confounding influence usually is not included in the uncertainty budget.

In this paper we report the manual and automatic CT-based segmentation variation for the tissues included in the 3D patient models for head and neck HTP. In addition, we compared the impact of the manual and automatic segmentation variation on the HTP outcomes, i.e. the planned hyperthermia dose and HTP quality. To quantify the importance of segmentation variations, we compare their influence to those of other sources of patient-modeling variation, i.e. gridsize and dielectric tissue-property uncertainties. The decision, whether or not to introduce the automatic-segmentation algorithm into the clinic, can be based on these results.

2.2 Methods

2.2.1 Patient selection

The analysis presented in this paper covers 7 of the 34 patients treated with head and neck hyperthermia thus far. The patients were selected to represent the patient population eligible for head and neck hyperthermia, i.e. the patients included were balanced per tumor site, and both small (T2) and large (T4) tumors were included (Supplementary Table 2.1).

2.2.2 Computed Tomography (CT) images

CT scans acquired for radiotherapy treatment planning were used for HTP, leading to advantages in logistics and target region assignment. To make the group of patients for our study as representative as possible, we included CT scans of patients with distinct characteristics to span the entire patient population variability.

CT scans of the patients were obtained using a Somatom Sensation Open (Siemens AG, Erlangen, Germany), except for patient 3, who was scanned with a PQ 5000 (Philips Healthcare, Best, the Netherlands). The slice spacing varied from $1.5 - 2.5$ mm and the in-plane resolution varied from 0.7 x 0.7 mm to 1.0 x 1.0 mm, with a scan matrix of 512 x 512. For patients $1-5$, an intravenous injection of 100 ml contrast agent (Omnipaque 300, GE Healthcare Inc.) was administered with an injection rate of 1.8 ml/s, and imaging was performed 45 seconds after injection.

2.2.3 Segmentation protocol

All CT slices are segmented into several normal tissues and the target volume. We used the clinical target volume (CTV) as the hyperthermia target volume (HTV), and segmented the GTV in order to assign tumor dielectric tissue properties to this region. The list of segmented tissues was based on the visibility on CT and the dielectric (and thermal) property contrast with adjacent tissues. The brain, spinal cord and eyes were segmented since these are highly thermo-sensitive tissues. Therefore, the thermal dose should be restricted in these tissues. Note that thresholds were not used in the optimization, and are only relevant in online steering since absolute SAR level calculations requires the clinically applied power.

First, an in-house developed tool (implemented in MevisLab v.2.2.1, MeVis Medical Solutions AG, Bremen, Germany) was used to remove non-patient structures, such as the patient bed and the patients immobilization mask. Second, Hounsfield (HU) thresholds were applied to segment bone (HU: 200 to 3000), muscle (HU: 0 to 200), fat (HU: -300 to 0), lungs and internal air (HU: -1000 to -300)[49]. The lungs were separated from the internal air by applying the threshold only to the slices that contain lung tissue. Third, the automatically segmented bone was manually corrected in case of streak artifacts, and when blood vessels were incorrectly assigned as bone due to the presence of contrast agent. Fourth, the tissues in the brain (cerebrum, cerebellum, brainstem), the spinal cord

(myelum), the eyes (sclera, lens, vitreous humor, optical nerve) and the other head and neck tissues (thyroid gland, thyroid and cricoid cartilage) were segmented manually using iSeg (v.3.1, Zurich Med Tech AG, Zurich, Switzerland) and automatically using a multi-atlas approach combined with intensity modeling[34]. Fifth, the HTV and GTV were both manually segmented in Focal (v.4.64, Elekta AB, Stockholm, Sweden) by a head and neck radiation oncologist.

2.2.4   Hyperthermia treatment planning (HTP)

Hyperthermia treatment planning was performed as described by Rijnen et al.[89]. For electromagnetic field simulations, a uniform gridsize of 2 mm was chosen. Dielectric tissue properties, i.e. relative permittivity (ϵ_r), effective conductivity (σ_eff) and volume density of mass (ρ) were assigned to each tissue[40,56] (Supplementary Table 2.2). The commenly used 1g-averaged and 10g-averaged specific absorption rate (SAR) standards [IEEE/IEC62704-1] as calculated in SEMCAD X (v.14.8.1, Schmid & Partner Engineering AG, Zurich, Switzerland) were used for SAR dosimetry.

For the tissue property sensitivity study, we reduced computational time twelve-fold by performing only one simulation, i.e. a simulation with all antennas exited using optimized phase and amplitude settings instead of a simulation per antenna and a subsequent weighted summation of the fields. The validity of this approximation for the sensitivity analysis was verified for three variations (ϵ_r: $+6\%$, σ_eff: $+6\%$, ρ: $+3\%$), in which we observed an average error in HTP quality ($|\Delta\mathrm{HTQ}|$) of only 0.2% (min $-$ max: $0.02 - 0.6\%$).

2.2.5   Segmentation evaluation

Three trained medical radiation technologists (observer 1, observer 2, observer 3) and one radiation oncologist (reference) manually segmented per patient the ten tissues, see Figure 2.1 for segmentation examples. The reference segmented the seven patient models only once, while the 3 other observers segmented them twice to investigate intra-observer variation. The manual tissue segmentation of one patient took on average 5-6 hours, all segmentations were done within 4 weeks and the time between first and second segmentation of the same patient varied between 1-15 days. The images were anonymized and supplied in a random order to minimize bias in the manual segmentations. The automatic-segmentation algorithm took on average 1 hour per patient (3.3 GHz Intel Core i7-980 processor, with 24 GB of RAM, running 64 bit Windows 7). Since the segmentation of the radiation oncologist is assumed as most accurate, variations from that segmentation are reported as segmentation inaccuracies. The observer-reference variations (inter-observer variation: reference-observer 1, reference-observer 2, reference-observer 3), the variation between two segmentations per observer (intra-observer variation: observer 1-observer 1, observer 2-observer 2, observer 3-observer 3) and the automatic-reference variations were determined. Observer variation was quantified using the Dice similarity coefficient[30] and the mean surface distance (MSD)(itkContourMeanDistanceImageFilter,

www.itk.org), i.e. the average distance between two volumes. Since DSC measures the overlap between volumes, the variation is quantified using 1-DSC. We used DSC instead of 1-DSC to compare our results to other studies.

(a) Cerebrum   (b) Cerebellum   (c) Brainstem   (d) Myelum & Cartilage

(e) Vitreous Humor & Lens   (f) Sclera   (g) Optical Nerve   (h) Thyroid
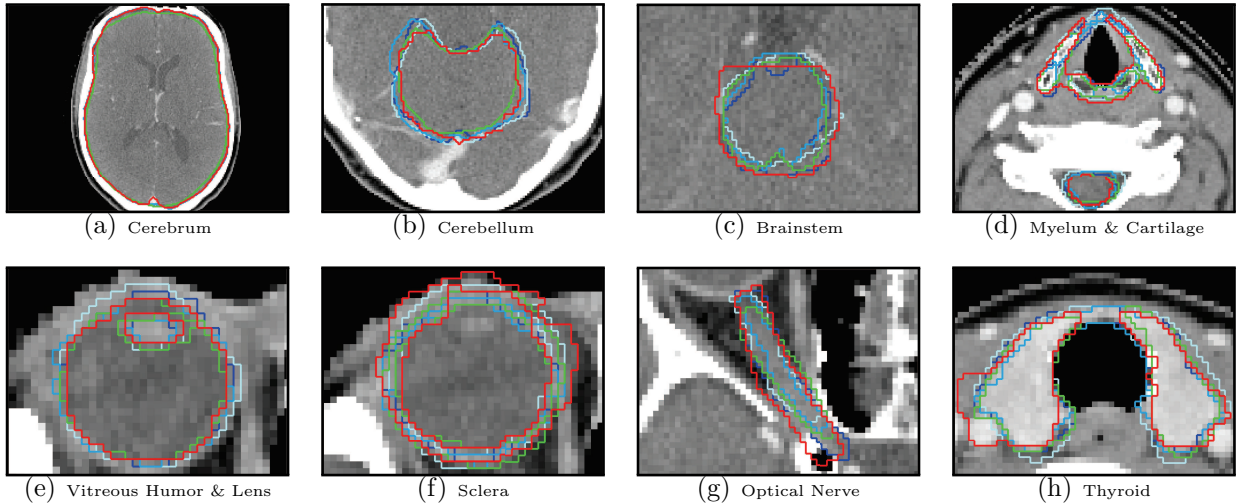
Figure 2.1: The segmentations of observer 1 (dark-blue), observer 2 (light-blue), observer 3 (blue), reference (green) and the auto-segmentation (red). The tissues were segmented on each transverse slice of the image set. For the head and neck HTP, these segmentations are stacked on top of each other to generate the 3D patient model. The 3D SAR dose distribution is calculated on the basis of this model.

2.2.6   Dosimetric evaluation

As temperature dose predictions still come with high uncertainties, we quantified the effect of segmentation variation on the planned hyperthermia dose using the absolute SAR difference expressed in two SAR parameters, i.e. $|\Delta SAR_{1g}|$ and $|\Delta SAR_{10g}|$, and on HTP quality using $|\Delta HTQ|$.

$|\Delta SAR_{1g}|$ and $|\Delta SAR_{10g}|$ are computed per tissue and defined as the SAR difference between two treatment plans, normalized for 1W total input power. Both values were averaged over the tissue volume and observers, and were the mean over the seven patients. Furthermore, the relative difference with respect to the average SAR in the reference is reported. Absolute SAR values were obtained per power level by multiplication with the total input power level[78].

HTQ is computed by using the SAR_{1g} only, and is defined as the average SAR in the first percentile of the SAR in the healthy tissue, i.e. the average over the highest SAR values, divided by the average SAR in the target volume[14]. The HTQ error ($|\Delta HTQ|$) is defined as the absolute difference in HTQ between two treatment plans.

A non-parametric Wilcoxon signed rank test was used to test for statistical significant differences (p<0.05).

2.2.7 Sensitivity analysis

The variation in HTP prediction per observer-dependent segmentation was compared with other sources of 3D patient modeling variation, i.e. gridsize variation and dielectric tissue property uncertainties. The uncertainty is quantified in $|\Delta HTQ|$ to assess the impact on HTP quality and in $|\Delta SAR_{10g}|$ to compare our results to other studies.

For all seven patients, the effect of the gridsize was investigated by increasing gridsize ($\Delta grid$), i.e. from 1 to 5 mm. For each gridsize, $|\Delta HTQ|$ and $|\Delta SAR_{10g}|$ were determined by using the HTP with $\Delta grid = 1$ mm as reference.

Dielectric tissue properties in patients deviate from literature values, e.g. due to age-dependency[83,84,92], post-mortem changes[13,93], and measurement uncertainty[39,41,72], as summarized in Supplementary Table 2.2. The impact of this deviation on HTP quality was determined in seven patients, for fourteen tissues. For each tissue property, three different HTPs were generated, i.e. using average and $\pm$ one standard deviation of the literature value. $|\Delta HTQ|$ was determined by using the HTP for the average literature value as reference. The individual uncertainty per tissues was obtained by taking the square-root of the sum of squares of the mean value over seven patients.

The individual standard uncertainty (u_i) of the gridsize, segmentation variation and dielectric properties was obtained by determining the confidence interval from plus to minus one standard deviation. The square-root of the sum of squares was applied to the individual uncertainties to obtain the combined standard uncertainty (u_c). A coverage factor (k) of 2 was used to obtain the expanded uncertainty U leading to the 95% confidence interval[97]. The uncertainties were determined based on the assumption that the applied variations can be described by a Gaussian probability function.

2.3 Results

Table 2.1 compares manual (inter-observer) and automatic segmentation variation per tissue (MSD) and the impact of this variation on simulated hyperthermia dose ($|\Delta SAR_{1g}|$). It shows for cerebellum, spinal cord, optical nerve, cartilage and thyroid gland a non-significant difference between manual and automatic generated 3D models in both segmentation variation and tissue specific dose, while a significant difference was found for cerebrum, brainstem, sclera, lens and vitreous humor (the latter two tissues with respect to segmentation only).

Local tissue SAR differences varied among both SAR parameters used, e.g. the manual (inter-observer) segmentation variation of the lens resulted in a $|\Delta SAR_{1g}|$ of 15 mW/kg (12%) but in a lower $|\Delta SAR_{10g}|$ of 3.5 mW/kg (3.8%) ($|\Delta SAR_{10g}|$ is shown in Supplementary Table 2.3).

Figure 2.2 shows that simulation accuracy substantially decreased when HTP was

Table 2.1: Manual (inter-observer) and auto-segmentation variation for the ten selected tissues. The segmentation variation is quantified by the mean distance (MSD). The impact of this variation on the simulated hyperthermia dose is quantified in $|\Delta \text{SAR}_{1g}|$, normalized at 1 W total input power. The statistical significant difference between manual- and auto-segmentation is indicated with a $^\nabla$. Note that both the manual and auto-segmentation variation are defined with respect to the reference observer.

	Manual Segmentation mean, min−max mean (rel. diff.)	Auto Segmentation mean, min−max mean (rel. diff.)
Cerebrum		
MSD [mm]	2.4, 2.0−2.9	2.9^∇, 2.5−3.2
$|\Delta \text{SAR}_{1g}|$ [mW/kg]	0.32 (1.2%)	0.44^∇ (1.6%)
Cerebellum		
MSD [mm]	2.2, 1.8−2.5	1.9, 1.3−3.4
$|\Delta \text{SAR}_{1g}|$ [mW/kg]	0.92 (3.1%)	0.94 (3.2%)
Brainstem		
MSD [mm]	1.7, 1.1−2.4	2.2^∇, 1.7−3.1
$|\Delta \text{SAR}_{1g}|$ [mW/kg]	0.87 (6.3%)	1.3^∇ (9.3%)
Spinal Cord (Myelum)		
MSD [mm]	1.0, 0.81−1.3	1.5, 0.82−2.4
$|\Delta \text{SAR}_{1g}|$ [mW/kg]	0.84 (5.7%)	0.86 (5.8%)
Sclera		
MSD [mm]	0.87, 0.63−1.8	1.8^∇, 1.0−3.8
$|\Delta \text{SAR}_{1g}|$ [mW/kg]	3.4 (4.2%)	4.8^∇ (6.0%)
Lens		
MSD [mm]	0.66, 0.44−1.2	1.6^∇, 0.75−2.9
$|\Delta \text{SAR}_{1g}|$ [mW/kg]	15 (12%)	15 (12%)
Vitreous Humor		
MSD [mm]	0.70, 0.54−1.1	1.2^∇, 0.87−1.8
$|\Delta \text{SAR}_{1g}|$ [mW/kg]	3.3 (3.3%)	4.3 (4.3%)
Optical Nerve		
MSD [mm]	0.94, 0.62−1.7	1.0, 0.76−1.4
$|\Delta \text{SAR}_{1g}|$ [mW/kg]	0.92 (2.9%)	1.2 (3.8%)
Cartilage		
MSD [mm]	4.5, 3.1−6.1	5.0, 3.0−6.9
$|\Delta \text{SAR}_{1g}|$ [mW/kg]	5.8 (6.4%)	6.0 (6.6%)
Thyroid Gland		
MSD [mm]	1.9, 0.54−4.7	5.1, 1.1−9.3
$|\Delta \text{SAR}_{1g}|$ [mW/kg]	0.39 (1.7%)	0.68 (3.0%)

based on a gridsize of 3 mm or larger. Because the simulation accuracy was stable for a gridsize in the range of $1.3 - 2.5$ mm, we chose a gridsize of 2 mm as trade-off between HTQ error and simulation time.
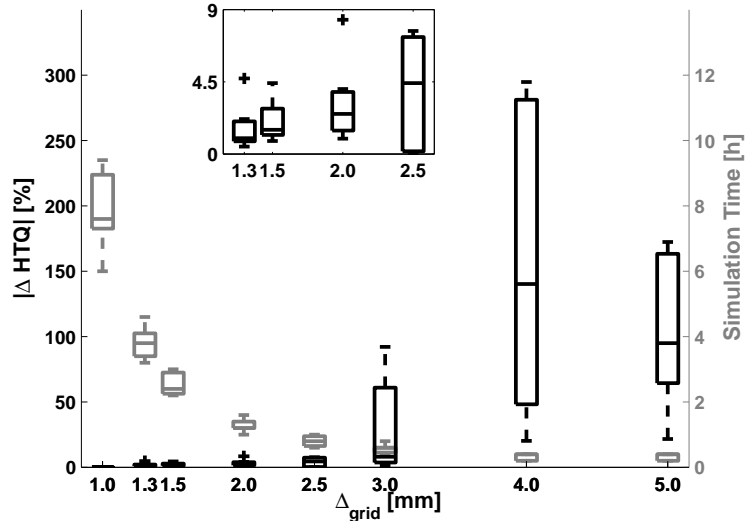
Figure 2.2: The error in hyperthermia-treatment quality parameter ($|\Delta\text{HTQ}|$), and simulation time as a function of gridsize (Δgrid). The boxplot indicates the range of the error over seven patients. The insert shows a zoom-in of Δgrid 1.3-2.5 mm. Note that ($|\Delta\text{HTQ}|$) is determined using the patient model with Δgrid 1mm as the reference. On each box of the boxplot, the central mark is the median, the edges are the 25th and 75th percentiles, the whiskers extend to the most extreme data points not considered outliers (99.3%), and outliers are plotted individually(+).

Figure 2.3 shows the impact of tissue property uncertainties on HTP quality ($|\Delta\text{HTQ}|$), for one patient. HTP quality appeared to be most sensitive to inaccuracies in the dielectric tissue properties of muscle, fat, and bone regions.

Table 2.2 summarizes the influences of the patient modeling parameters on $|\Delta\text{HTQ}|$, for the seven patients ($|\Delta\text{SAR}_{10g}|$ is shown in Supplementary Table 2.4). The $|\Delta\text{HTQ}|$ due to inter-observer variation (1.0%), intra-observer variation (1.0%) (Supplementary Table 2.3) and automatic-segmentation (1.0%) was similar, but substantially smaller that the uncorrelated standard combined uncertainty (11.7%) and the expanded uncertainty (23.4%) for the uncertainties studied.

2.4 Discussion

In this study, we report the CT-based normal-tissue-segmentation variations and the impact of these variations on HTP, i.e. the planned hyperthermia dose and HTP quality,
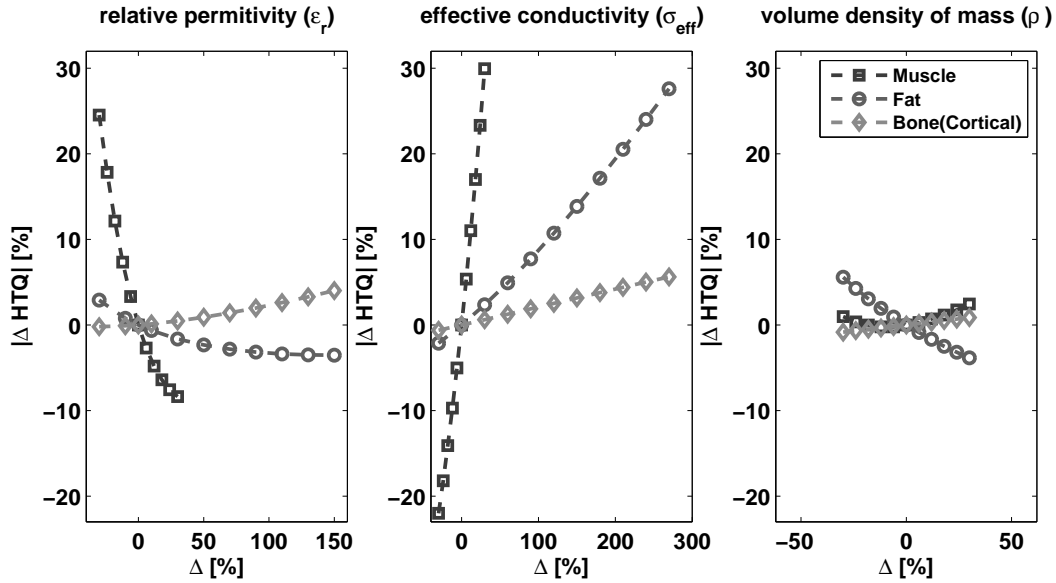
Figure 2.3: The error in hyperthermia-treatment quality parameter ($|\Delta$HTQ$|$) as a function of the relative tissue property variation Δ, for patient 5. Only the tissues with an individual standard uncertainty > 1.0% are shown.

Table 2.2: Influence of patient modeling parameters on the uncorrelated standard uncertainty (u_c) and the expanded uncertainty (U) as measured with $|\Delta$HTQ$|$. k: coverage factor, u_i: individual standard uncertainty

	u_i [%]
Gridsize (Δgrid)	4.0
Tissue segmentation	
(a) Manual segmentation	
(a$_1$) Inter-observer	1.0
(a$_2$) Intra-observer	1.0
(b) Auto-segmentation	1.0
Dielectric tissue properties	
(a) Relative permittivity (ϵ_r)	4.1
(b) Effective conductivity (σ_{eff})	10.0
(c) Volume density of mass (ρ)	1.0
u_c (k=1)	11.7
U (k=2)	23.4

for both manual- and automatic-segmented tissues. For all segmented tissues, the local tissue SAR differences varied among SAR parameters, i.e. $|\Delta$SAR$_{1g}|$ and $|\Delta$SAR$_{10g}|$. This makes tissue dose assessment with these parameters difficult, which forms the rationale to investigate the impact on simulated temperatures, as soon as temperature simulations are validated. Although half of the segmented tissues were significantly different after

manual or auto-segmentation, the impact on HTP quality was similar, but, this impact was minor compared to the total HTP uncertainty. Furthermore, a considerable reduction in operator time per patient was achieved when using the automatic segmentation ($\pm$ 1 hour) instead of the manual segmentation (5-6 hours). Thus, the recently developed automatic-segmentation algorithm can be introduced in the clinic for pre-treatment and real-time treatment optimization.

Previous studies that quantified the variations in tissue segmentation for head and neck radiotherapy treatment planning provide an excellent reference for our results. Brouwer et al.[12] reported in an inter-observer study with five observers that the thyroid gland can be segmented as accurate as the spinal cord, while we found a difference in accuracy between these two tissues. This difference can be explained by a difference in the segmentation protocol, i.e. we segmented the thyroid and cricoid cartilage as one structure, which may have led to larger segmentation inaccuracies. Recently, Nelms et al.[74] quantified the inter-observer agreement for the brainstem, brain and spinal cord. For the brainstem (31 observers) they found a lower DSC (mean $\pm$ std) of 0.66 ± 0.17, compared to a DSC of 0.78 ± 0.04 found in our study (Supplementary Table 2.3). For the spinal cord (29 observers) they found 0.80 ± 0.07 compared to 0.79 ± 0.04 in our study and for the brain (10 observers) they found 0.98 ± 0.01 compared to 0.94 ± 0.01 for the cerebrum in our study. In general, despite some minor differences, the variations in tissue segmentation reported in our study are similar to the results of previous studies.

In the design of this study, we faced the common difficulty of defining HTP quality[80]. Hyperthermia outcome has been correlated to the temperatures, or temperature dose, achieved[38,94]. However, temperature simulations are unsuitable since they have not been validated yet for head and neck hyperthermia. In pre-treatment and real-time HTP for head and neck hyperthermia, we therefore optimize the target SAR. For simulated SAR, Paulides et al. verified from treatment data of three patients, on a per-patient basis, a linear relation with measured temperatures ($R^2 = 0.59 - 0.94$)[79]. For HTQ, Canters et al.[14] showed for deep hyperthermia in the pelvis a linear correlation with simulated steady state temperatures. Hence, in the absence of validated temperature predictions, both parameters: 1) HTQ to quantify HTP quality, and 2) the standardly used averaged-tissue SAR to quantify tissue dose, have potential as surrogate for simulated temperatures.

The dose differences reported in Table 2.1 were all determined for 1 W total input power. An average input power of 400 W is applied during a standard head and neck treatment[79]. Hence, the reported dose values should be multiplied by 400 if the results need to be translated to a standard head and neck treatment. For example, the maximum $|\Delta SAR_{1g}|$ was found in the lens: 0.0151 W/kg, which leads to a $|\Delta SAR_{1g}|$ of 6.0 W/kg at 400W. Note that in this case the maximum SAR_{1g} in the lens is 254.7 W/kg. Future studies are needed to clarify if the resultant temperatures go beyond the defined thermal thresholds.

The reported individual standard uncertainty in $|\Delta SAR_{10g}|$ of the gridsize was estimated as 3.2% (Supplementary Table 2.4), which is lower than the 6.2% (0.26 dB) found by Murbach et al.[73] and the 5.5% found by Bakker et al.[7]. However, the frequency and gridsizes studied (64 MHz and $1.5 - 3$ mm[73], $10 - 5600$ MHz and $0.7 - 10$ mm[7]) differed

from our settings, limiting the comparability. Our estimation of the individual standard uncertainty in $|\Delta \mathrm{SAR}_{10g}|$ for dielectric tissue parameters (ϵ_r: 3.4%, σ_eff: 6.2%) was in agreement with previously reported values (ϵ_r: 2.1%[73], 8.7%[7], σ_eff: 3.5%[73], 8.7%[7]). Our individual standard uncertainty in $|\Delta \mathrm{SAR}_{10g}|$ for ρ (4.4%) is lower than previously reported values (6.2%[73], 5%[7]). The differences in uncertainty for the dielectric tissue properties and ρ can also be explained by the difference in frequency, but probably also because we employed tissue specific uncertainties while others applied one common uncertainty for all tissues. We expected the uncertainty in segmentation variation and gridsize to be in the same range, since both are changing the 3D patient model. From other studies[7,73], we know that especially dielectric tissue properties have a high influence, but this had never been shown for head and neck HTP.

2.5   Conclusion

As the uncertainty in HTP quality for manual and automatic segmentation is similar and minor when comparing it to the total HTP uncertainty, we conclude that the recently developed automatic-segmentation algorithm can be introduced in the clinic for pre-treatment and real-time treatment optimization. However, tissue dose assessment, used for safety assessment and pre-treatment and real-time decision making, remains difficult since local tissue SAR estimates vary among different SAR parameters. This forms a rationale for future studies to investigate the impact on simulated temperatures, as soon as temperature simulations are validated.

2.6 Supplementary Tables

Supplementary Table 2.1: Patient, tumor and treatment characteristics. F: female, M: male, r: recurrent, c: clinical, p: pathology, CBK: cyberknife, IMRT: intensity modulated radiation therapy, BT: brachytherapy

Patient	Gender	Age	Tumor Site	TNM classification	Hyperthermia	Radiotherapy
1	F	38	Nasal Cavity	rT4bN0M0	3x	5x5.5 Gy (CBK)
2	F	58	Thyroid	rT4N1bM0	4x	16x3.13 Gy (IMRT)
3	F	74	Nasopharynx	rT4N0M0	3x	6x6 Gy (CBK)
4	M	51	Oropharynx	cT2N0M0	6x	4, 10x3, 4 Gy (BT)
5	F	59	Oropharynx	cT2N0M0	9x	35x2 Gy (IMRT)
6	M	60	Thyroid	pT4aN1bM0	4x	16x3.13 Gy (IMRT)
7	M	54	Oropharynx	rT2N0M0	1x	6x5.5 Gy (CBK)

Supplementary Table 2.2: Dielectric tissue properties and their uncertainties at 434 MHz. ϵ_r: relative permittivity, σ_{eff}: effective conductivity, ρ: volume density of mass, GTV: gross target volume, σ: standard deviation.

Tissue	ϵ_r [-]	ϵ_r [%] Range(3σ)	ϵ_r [%] Range(σ)	Range Studied [%]	σ_{eff} [S m^{-1}]	σ_{eff} [%] Range(3σ)	σ_{eff} [%] Range(σ)	Range Studied [%]	ρ [kg m^{-3}]	ρ [%] Range(3σ)	ρ [%] Range(σ)	Range Studied [%]
Muscle	56.9	-10−18	-3−6	-30−30	0.81	-10−18	-3−6	-30−30	1041	±10	±3	-30−30
Fat	11.6	-10−120	-3−40	-30−150	0.08	-10−250	-3−83	-30−270	916	±10	±3	-30−30
Bone	13.1	-10−90	-3−30	-30−150	0.09	-10−190	-3−63	-30−270	1990	±10	±3	-30−30
Lung	23.6	-10−18	-3−6	-30−30	0.38	-10−18	-3−6	-30−30	655	±50	±17	-60−60
Air	1.00	−	−	−	0.00	−	−	−	1.2	−	−	−
Cerebrum	56.8	-10−18	-3−6	-30−30	0.75	-10−18	-3−6	-30−30	1039	±10	±3	-30−30
Cerebellum	55.1	-10−18	-3−6	-30−30	1.05	-10−18	-3−6	-30−30	1040	±10	±3	-30−30
Brainstem	41.7	-10−20	-3−7	-30−40	0.45	-10−20	-3−7	-30−78	1039	±10	±3	-30−30
Spinal Cord (Myelum)	35.0	-10−30	-3−10	-30−40	0.46	-10−40	-3−13	-30−78	1038	±10	±3	-30−30
Sclera	57.4	-10−18	-3−6	-30−30	1.01	-10−18	-3−6	-30−30	1032	±10	±3	-30−30
Lens	37.3	-10−39	-3−13	-30−40	0.38	-10−75	-3−25	-30−78	1090	±10	±3	-30−30
Vitreous Humor	69.0	-10−18	-3−6	-30−30	1.53	-10−18	-3−6	-30−30	1009	±10	±3	-30−30
Optical Nerve	35.0	-10−30	-3−10	-30−40	0.46	-10−40	-3−13	-30−78	1038	±10	±3	-30−30
Thyroid Gland	61.3	-10−18	-3−6	-30−30	0.89	-10−18	-3−6	-30−30	1050	±10	±3	-30−30
Cartilage	45.1	-10−18	-3−6	-30−30	0.60	-10−18	-3−6	-30−30	1100	±10	±3	-30−30
GTV	59.0	−	−	−	0.89	−	−	−	1050	−	−	−
Deionized Water	78.0	−	−	−	0.04	−	−	−	1000	−	−	−

Supplementary Table 2.3: Manual (inter-observer and intra-observer) and auto-segmentation variation for the ten selected tissues. The segmentation variation is quantified by the 1- Dice similarity coefficient (1-DSC) and the mean distance (MSD). The difference in simulated hyperthermia dose ($|\Delta SAR_{1g}|$ and $|\Delta SAR_{10g}|$, normalized at 1 W total input power) in each tissue is shown. The statistical significant difference between inter-observer and intra-observer variation($\diamond$) and between auto-segmentation and inter-observer($\triangledown$) or intra-observer(*) variation is determined using a non-parametric Wilcoxon signed rank test. Note that the inter-observer and auto-segmentation variation is defined with respect to the reference observer.

	Manual (inter-observer) mean, min−max mean, min−max mean (rel. diff.) & mean (rel. diff.)	Manual (intra-observer) mean, min−max mean, min−max mean (rel. diff.) & mean (rel. diff.)	Auto-Segmentation mean, min−max mean, min−max mean (rel. diff.) & mean (rel. diff.)
Cerebrum			
1-DSC	0.059, 0.052−0.069	0.010$^\diamond$, 0.010−0.013	0.058*, 0.050−0.068
MSD [mm]	2.4, 2.0−2.9	0.43$^\diamond$, 0.36−0.54	2.9*$^{,\triangledown}$, 2.5−3.2
$|\Delta SAR_{1g}|$&$|\Delta SAR_{10g}|$ [mW/kg]	0.32 (1.2%) & 0.23 (0.90%)	0.24$^\diamond$ (0.87%) & 0.18 (0.70%)	0.44*$^{,\triangledown}$ (1.6%) & 0.35*$^{,\triangledown}$ (1.4%)
Cerebellum			
1-DSC	0.14, 0.12−0.16	0.065$^\diamond$, 0.046−0.086	0.13*, 0.088−0.20
MSD [mm]	2.2, 1.8−2.5	0.88$^\diamond$, 0.62−1.2	1.9*, 1.3−3.4
$|\Delta SAR_{1g}|$&$|\Delta SAR_{10g}|$ [mW/kg]	0.92 (3.1%) & 0.60 (2.2%)	0.63$^\diamond$ (2.1%) & 0.40$^\diamond$ (1.5%)	0.94* (3.2%) & 0.57* (2.1%)
Brainstem			
1-DSC	0.22, 0.15−0.27	0.16$^\diamond$, 0.15−0.18	0.24*, 0.19−0.32
MSD [mm]	1.7, 1.1−2.4	1.1$^\diamond$, 0.92−1.2	2.2*$^{,\triangledown}$, 1.7−3.1
$|\Delta SAR_{1g}|$&$|\Delta SAR_{10g}|$ [mW/kg]	0.87 (6.3%) & 0.59 (3.7%)	0.68 (4.9%) & 0.45 (2.8%)	1.27*$^{,\triangledown}$ (9.3%) & 0.69* (4.3%)
Spinal Cord (Myelum)			
1-DSC	0.21, 0.16−0.27	0.15$^\diamond$, 0.13−0.16	0.24*, 0.18−0.34
MSD [mm]	1.0, 0.81−1.3	0.55$^\diamond$, 0.51−0.60	1.5*, 0.82−2.4
$|\Delta SAR_{1g}|$&$|\Delta SAR_{10g}|$ [mW/kg]	0.84 (5.7%) & 0.42 (3.6%)	0.43 (2.9%) & 0.18 (1.6%)	0.86* (5.8%) & 0.35 (3.0%)
Sclera			
1-DSC	0.52, 0.44−0.70	0.37$^\diamond$, 0.33−0.38	0.62*$^{,\triangledown}$, 0.45−0.76
MSD [mm]	0.87, 0.63−1.8	0.51$^\diamond$, 0.45−0.60	1.8*$^{,\triangledown}$, 1.0−3.8
$|\Delta SAR_{1g}|$&$|\Delta SAR_{10g}|$ [mW/kg]	3.4 (4.2%) & 1.6 (2.4%)	1.9$^\diamond$ (2.4%) & 0.84 (1.3%)	4.8*$^{,\triangledown}$ (6.0%) & 2.1* (3.1%)
Lens			
1-DSC	0.32, 0.24−0.45	0.20$^\diamond$, 0.15−0.25	0.50*$^{,\triangledown}$, 0.34−0.64
MSD [mm]	0.66, 0.44−1.2	0.32$^\diamond$, 0.23−0.44	1.6*$^{,\triangledown}$, 0.75−2.9
$|\Delta SAR_{1g}|$&$|\Delta SAR_{10g}|$ [mW/kg]	15 (12%) & 3.5 (3.8%)	3.4$^\diamond$ (2.6%) & 1.3 (1.3%)	15* (12%) & 4.1 (4.4%)
Vitreous Humor			
1-DSC	0.14, 0.11−0.18	0.086$^\diamond$, 0.076−0.096	0.20*$^{,\triangledown}$, 0.16−0.28
MSD [mm]	0.70, 0.54−1.1	0.38$^\diamond$, 0.35−0.43	1.2*$^{,\triangledown}$, 0.87−1.8
$|\Delta SAR_{1g}|$&$|\Delta SAR_{10g}|$ [mW/kg]	3.3 (3.3%) & 2.0 (2.6%)	1.9$^\diamond$ (1.9%) & 1.0$^\diamond$ (1.3%)	4.3* (4.3%) & 2.5 (3.2%)
Optical Nerve			
1-DSC	0.40, 0.34−0.50	0.30$^\diamond$, 0.24−0.35	0.42*, 0.37−0.51

Continued on next page

Supplementary Table 2.3 – *Continued from previous page*

	Manual (inter-observer)	Manual (intra-observer)	Auto-Segmentation
	mean, min−max	mean, min−max	mean, min−max
	mean, min−max	mean, min−max	mean, min−max
	mean (rel. diff.) & mean (rel. diff.)	mean (rel. diff.) & mean (rel. diff.)	mean (rel. diff.) & mean (rel. diff.)
MSD [mm]	0.94, 0.62−1.7	0.57$^\diamond$, 0.36−0.71	1.0*, 0.76−1.4
$\|\Delta SAR_{1g}\|\&\|\Delta SAR_{10g}\|$ [mW/kg]	0.92 (2.9%) & 0.39 (0.90%)	0.59$^\diamond$ (1.9%) & 0.33 (0.80%)	1.2* (3.8%) & 0.63 (1.4%)
Cartilage			
1-DSC	0.41, 0.28−0.54	0.22$^\diamond$, 0.12−0.29	0.51*,$^\triangledown$, 0.45−0.61
MSD [mm]	4.5, 3.1−6.1	0.67$^\diamond$, 0.35−1.2	5.0*, 3.0−6.9
$\|\Delta SAR_{1g}\|\&\|\Delta SAR_{10g}\|$ [mW/kg]	5.8 (6.4%) & 3.0 (2.9%)	1.4$^\diamond$ (1.6%) & 0.92$^\diamond$ (0.90%)	6.0* (6.6%) & 2.8* (2.7%)
Thyroid Gland			
1-DSC	0.24, 0.11−0.47	0.16, 0.085−0.29	0.43, 0.20−0.63
MSD [mm]	1.9, 0.54−4.7	0.80, 0.39−1.8	5.1, 1.1−9.3
$\|\Delta SAR_{1g}\|\&\|\Delta SAR_{10g}\|$ [mW/kg]	0.39 (1.7%) & 0.33 (1.2%)	0.37 (1.6%) & 0.32 (1.2%)	0.68 (3.0%) & 0.47 (1.7%)

Supplementary Table 2.3 shows a complete overview of the results, including the intra-observer variation and the parameters (1-DSC and $\|\Delta SAR_{10g}\|$). This table shows that the cerebellum, brainstem, spinal cord and vitreous humor could be segmented with a mean 1-DSC of ≤ 0.24 and a mean MSD of ≤ 2.2 mm, leading to a mean $\|\Delta SAR_{1g}\|$ and $\|\Delta SAR_{10g}\|$ up to 4.3 mW/kg (4.3%). The cerebrum, sclera, lens, optical nerve, cartilage and thyroid gland were segmented less accurate with a mean 1-DSC of ≥ 0.24 and/or a mean MSD ≥ 2.2 mm, corresponding to a higher mean $\|\Delta SAR_{1g}\|$ and $\|\Delta SAR_{10g}\|$ up to 15.1 mW/kg (11.7%). For most tissues, the intra-observer variation caused significantly less segmentation and tissue specific dose variation compared to the inter-observer variation. Local tissue SAR differences varied among both SAR parameters used, e.g. the inter-observer variation of the lens resulted in a $\|\Delta SAR_{1g}\|$ of 15 mW/kg (12%) but in a lower $\|\Delta SAR_{10g}\|$ of 3.5 mW/kg (3.8%).

Supplementary Table 2.4: Influence of patient modeling parameters on the uncorrelated standard uncertainty (u_c) and the expanded uncertainty (U) as measured with $|\Delta\text{HTQ}|$ and $|\Delta\text{SAR}_{10\text{g}}|$. k: coverage factor.

	(u_i) [%]	
	$|\Delta\text{HTQ}|$	$|\Delta\text{SAR}_{10\text{g}}|$
Gridsize (Δgrid)	4.0	3.2
Tissue segmentation		
(a) Manual segmentation		
(a$_1$) Inter-observer	1.0	1.5
(a$_2$) Intra-observer	1.0	1.2
(b) Auto-segmentation	1.0	2.0
Dielectric tissue properties		
(a) Relative permittivity (ϵ_r)	4.1	3.4
(b) Effective conductivity (σ_eff)	10.0	6.2
(c) Volume density of mass (ρ)	1.0	4.4
u_c (k=1)	11.7	9.3
U (k=2)	23.4	18.7

Relevance of MRI for H&N HTP:
CT vs CT&MRI based patient models

Abstract

Purpose: *In current clinical practice, head and neck (H&N) hyperthermia treatment planning (HTP) is solely based on computed tomography (CT) images. Magnetic resonance imaging (MRI) provides superior soft-tissue contrast over CT. The purpose of our study is to investigate the relevance of using MRI in addition to CT for patient modeling in H&N HTP.*

Materials and methods: *CT and MRI scans were acquired for eleven patients in an immobilisation mask. Three observers manually segmented on CT, MRI T1 weighted (MRI-T1w) and MRI T2 weighted (MRI-T2w) images the following thermo-sensitive tissues: cerebrum, cerebellum, brainstem, myelum, sclera, lens, vitreous humor and the optical nerve. For these tissues that are used for patient-modeling in H&N HTP, the inter-observer variation of manual tissue segmentation in CT and MRI was quantified with the mean surface distance (MSD).*

Next, we compared the impact of CT and CT & MRI based patient models on the predicted temperatures. For each tissue, we selected the modality that led to the lowest observer variation and inserted this in the combined CT & MRI based patient model (CT & MRI), after a deformable image registration. In addition, a patient model with a detailed segmentation of brain tissues (including white matter, grey matter and cerebrospinal fluid) was created (CT & MRI$_{\mathrm{db}}$). To quantify the relevance of MRI based segmentation for H&N HTP we compared the predicted maximum temperatures in the segmented tissues ($T_{\max}$) and the corresponding specific absorption rate (SAR) of the patient models based on 1) CT, 2) CT & MRI and 3) CT & MRI$_{\mathrm{db}}$.

Results: *In MRI, a similar or reduced inter-observer variation was found compared to CT (maximum of median MSD in CT: 0.93 mm, MRI-T1w: 0.72 mm, MRI-T2w: 0.66 mm). Only for the optical nerve the inter-observer variation is significantly lower in CT compared to MRI (median MSD in CT: 0.58 mm, MRI-T1w: 1.27 mm, MRI-T2w: 1.40 mm). Patient models based on CT ($T_{\max} : 38.0^{\mathrm{o}}\mathrm{C}$) and CT & MRI ($T_{\max} : 38.1^{\mathrm{o}}\mathrm{C}$) result in similar simulated temperatures, while CT & MRI$_{\mathrm{db}}$ ($T_{\max} : 38.5^{\mathrm{o}}\mathrm{C}$) resulted in significantly higher temperatures. The SAR corresponding to these temperatures did not differ significantly.*

Conclusions: *Although MRI reduces the inter-observer variation in most tissues, it does not affect simulated local tissue temperatures. However, the improved soft-tissue contrast provided by MRI allows generating a detailed brain segmentation, which has a strong impact on the predicted local temperatures and hence may improve simulation guided hyperthermia.*

3.1 Introduction

During hyperthermia, the tumor temperature is elevated towards $39-44$ºC to sensitize it for chemo- or radiotherapy. Clinical studies have proven that hyperthermia improves treatment outcome in several tumor sites[6,37,51,52,57,103], without adding toxicity. These studies stimulated the development of a hyperthermia applicator, called the HYPERcollar, which is specificly designed and validated for the non-invasive treatment of patients with a head and neck (H&N) tumor[78,79]. A HYPERcollar treatment requires hyperthermia treatment planning (HTP) for pre-treatment and real-time treatment optimization and tissue dose assessment[89]. Crucial input for HTP is a full 3D patient model, which is usually created by a manual, slice-by-slice tissue segmentation of computed tomography (CT) images. The generated 3D patient model together with a detailed model of the applicator are used to calculate the distribution of the electric field and the specific absorption rate (SAR) in the patient. This SAR distribution can be used as input for a temperature model to predict the temperature distribution. To effectively improve temperature simulation accuracy, we recently presented H&N hyperthermia patient-group specific tissue property values[107]. Further, H&N HTP was recently improved by the development and clinical validation of a CT-based automatic-segmentation tool for H&N HTP. This tool has shown to be a fast, reproducible and accurate replacement of the current tedious manual procedure[34,106]. The purpose of this study is to investigate whether tissue segmentation on magnetic resonance imaging (MRI) may further improve CT-based H&N HTP.

MRI is used more and more for hyperthermia, especially due to the development of non-invasive 3D MRI thermometry for treatment control[44,81,96]. Anatomical MRI scans may be usefull to improve tissue segmentation for patient model generation in HTP. The advantage of using MRI instead of CT images for segmentation is the superior soft-tissue contrast in MRI. Other advantages are the reduction of dental-inlay artefacts compared with CT images and improved target segmentation[5,32,88]. A disadvantage of MRI for segmentation is the relatively long scan-time, making MRI more prone to motion artifacts caused by swallowing and tongue movements. Other disadvantages are the susceptibility artifacts caused by air-tissue interfaces and the decreasing non-uniformity of the main magnetic field outside the center of the scanner leading to geometrical incorrectness in the regions distal from the center of the scanner. Hence, being aware of these disadvantages of MRI, there is a potential benefit to add MRI data to CT-based H&N HTP.

Although the relevance of MRI in radiotherapy treatment planning (RTP) has been shown previously, this study is the first to report on the relevance of MRI for HTP. Most RTP studies focused on the relevance of MRI for improving the segmentation of the target volume[46,88,98], while only a limited number were focused on the improvement for other tissues[5,42]. Typically, requirements for normal tissue delineation in HTP are far higher than for RTP, as more tissues need to be distinguished to correctly capture the impact of strong dielectric and thermal tissue property gradients between tissues[67,80]. Nevertheless, the limited subset of studies on normal tissue delineation for RTP serves as an excellent reference to compare the results for matching tissues in our more extensive tissue list.

In clinical practice, H&N HTP is currently based on the prediction of the SAR inside the patient. However, clinical outcome and toxicity is related to the thermal dose in the target and normal tissues[38,94]. Hence, temperature predictions may provide a better assessment of the thermal dose in the target and normal tissues. We recently showed that, due to the strong thermo-regulatory response of H&N tissues, region specific thermal tissue properties are required to improve accuracy in temperature predictions. In the current study, we applied the tissue properties of that study to investigate the effect on temperature of using combined CT-MRI based segmentation. This allowed a much better assessment of the impact of segmentation uncertainties on treatment planning reproducibility.

In this paper, we determined the manual inter-observer segmentation variation in CT and MRI for tissues used in H&N HTP. From that result, we selected for each tissue the modality that led to the lowest observer variation for building a combined CT- and MRI based patient model. In addition, to study the benefit of using the better soft-tissue contrast of MRI, we generated a patient model that also included a detailed segmentation of the brain. To investigate whether MRI based segmentation is relevant for H&N HTP, we compared the predicted temperatures and the corresponding SAR of the patient models based on 1) CT, 2) CT-MRI and 3) CT-MRI including the detailed brain segmentation.

3.2 Methods

3.2.1 Patient data and scan protocols

CT and MRI scans from 11 patients with a tumor in the H&N region were included in this study. All patients were treated with radiotherapy, but the patients were selected such that they are representative for the patient-group eligible for hyperthermia, i.e. tumor sites oropharynx (8 patients) and nasopharynx (3 patients). During acquisition with both modalities and during treatment, a patient-specific immobilization mask was used to synchronize patient positioning. Informed consent was obtained from all patients included in the study.

CT scans were obtained using a Somatom Sensation Open (Siemens AG, Erlangen, Germany) system. Scans were preceded by a single injection of 100 ml contrast agent (Omnipaque 300, GE Healthcare Inc.) with an injection rate of 1.8 ml/s, and imaging was performed 45 s after injection. Scans parameters were: acquisition matrix: 512 x 512, slice-thickness: 3 mm, tube voltage: 120 kV, tube current: 150 mAs, pitch: 0.55 mm, rotation time: 1.0 s. The reconstructed voxel resolution was 0.98 x 0.98 x 2.5 mm.

Axial MRI-T1 weighted (MRI-T1w) and MRI-T2 weighted (MRI-T2w) images were acquired on a 1.5 T scanner (Optima MR450w, GE Healthcare, Waukesha, WI). In 8 patients, a six channel flex coil was used to synchronize imaging and treatment positioning. At the start of the study this coil was unavailable, therefore the images of the first 3 patients were acquired using a 24 channel H&N coil that required a modified immobilization mask. Halfway the study, we realized that a 250 mm field-of-view (FOV) in frequency

encoding direction was too small for large patients, therefore we increased it to 350 mm resulting in a change of the voxel resolution from 0.49 x 0.49 x 3 mm (5 patients) to 0.68 x 0.68 x 3 mm (6 patients). For the T1w scans we used a Fast Spin Echo sequence with TE/TR: 10.8/465 ms and for the T2w scans we used a Fast Recovery Fast Spin Echo sequence with TE/TR 106.8/7060 ms. The other scan parameters were: acquisition matrix: 384x224, number of slices: 66, Flip angle: 90°. The total scan duration for either the MRI-T1w or MRI-T2w scan was 6 minutes.

3.2.2 Segmentation protocol

Three trained medical radiation technologists (observer 1-3) manually segmented for each patient the following thermo-sensitive tissues in CT, MRI-T2w and MRI-T1w images using ITK-SNAP[112]: cerebrum, cerebellum, brainstem, myelum, sclera, lens, vitreous humor and the optical nerve. The medical radiation technologists were trained using a clear and strict delineation protocol that is defined in cooperation with a senior radiation oncologist specialized in H&N cancers and a senior radiologist specialized in H&N imaging. During segmentation of CT, the observers were blinded for the MRI and vice versa, however, MRI-T1w segmentations were obtained by using MRI-T2w as a starting point for time-saving reasons. The manual CT and MRI segmentations took on average 8h per patient. All segmentations were done within 5 weeks and the time between CT and MRI segmentation of the same patient was at least 6 days; the segmentation of MRI-T1w and MRI-T2w were done on the same day. The images were anonymized and supplied in a random order to minimize bias in the manual segmentations.

During segmentation of the tissues on CT images, the observers were asked to use fixed display windowing settings[49]. For the cerebrum, cerebellum, brainstem and myelum they used a window level (WL) of 0 houndsfield units (HU) and a window width (WW) of 80 HU. For the sclera, lens, vitreous humor and optical nerve they used a WL of -125 HU and a WW of 350 HU.

HTP requires a full 3D patient model, hence, besides the tissues segmented by the observers, also a segmentation is needed of the target volume and normal tissues such as muscle, fat, bone, air, lung, thyroid gland, cricoid and thyroid cartilage. The target volume was manually segmented using Focal (v.4.64, Elekta AB, Stockholm, Sweden) by a H&N radiation oncologist. The other tissues were obtained using our CT-based automatic segmentation tool based on a multi-atlas approach combined with intensity modeling[34].

To study the effect on the HTP of a detailed segmentation of the brain we used an existing automatic brain segmentation method[17,25] and applied it to the T2w images. The detailed automatic-segmentation included cerebro-spinal fluid (CSF), grey matter (GM), and white matter (WM), as shown in Figure 3.1. The cerebrum in the CT-MRI patient model generated by observer one was replaced by those three tissues to generate a 3D patient model with a detailed brain segmentation (CT & MRI$_{obs1,db}$). We also included the CSF surrounding the myelum into this model.
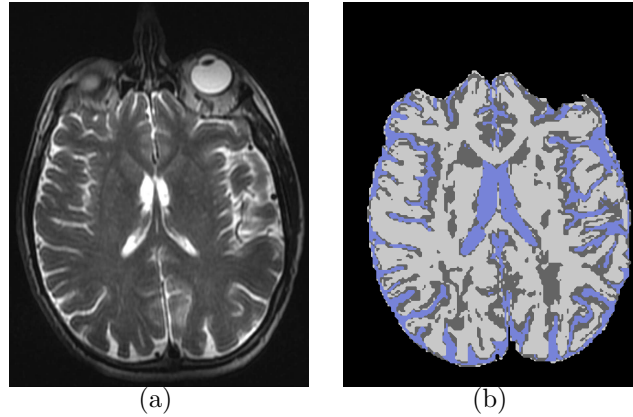
(a)   (b)

Figure 3.1: A slice of an MRI-T2w image (a) with the automatic detailed brain seg-
mentation (b), including white matter (white), grey matter (grey) and
cerebrospinal fluid (blue).

3.2.3   Temperature simulation settings

MRI-based models were compared to the current clinical standard, i.e. automatic CT-
based patient model generation (CT_{auto}), based on the predicted temperatures. For the
MRI-based models, we choose per tissue the imaging modality that led to the lowest
inter-observer variability to generate the combined CT and MRI based patient models,
using the manual segmentations either from observer 1 (CT & MRI_{obs1}), observer 2 (CT &
MRI_{obs2}) or observer 3 (CT & MRI_{obs3}). Together with the patient model with the detailed
brain segmentation (CT & $MRI_{obs1,db}$) this resulted in the following patient models:

1. CT_{auto},

2. CT & MRI_{obs1},

3. CT & MRI_{obs2},

4. CT & MRI_{obs3},

5. CT & $MRI_{obs1,db}$.

   The manual MRI segmentations of each observer were registered to the CT coordinate
system by a deformable image registration using optimized parameters for our image set[35].
HTP was performed as described by Rijnen et al.[89] and the gridsize was as in Verhaart et
al.[106]. Temperature simulations settings were equal to Verhaart et al.[107], and the dielectric
and thermal tissue properties are shown in Table 3.1. Since the thermal conductivity
(k) and perfusion (ω) of the segmented tissues under thermal stress is unknown, we
mimicked this increase by appling the same increase as the increase in muscle tissue when
going from a baseline value (no thermal stress)[47] to the optimized value under thermal

stress[107], leading to 11.7 fold (k) and 14.4 fold (ω) increase, resulting to the values shown in Table 3.1. For the HTP based on the $\mathrm{CT_{auto}}$ patient model, the total input power was increased until the simulated temperature in normal tissue exceeded 45 °C[60] or the manually segmented thermo-sensitive tissues exceeded 40 °C[48]. This optimized total input power was applied to the HTP based on the CT & MRI patient models.

Table 3.1: Electromagnetic and thermal tissue properties. *: value in [47] scaled 11.7 fold, +: value in [47] scaled 14.4 fold.

Tissue	ϵ_r	σ_eff	ρ	c	k	Q	ω
internal air	1.0	0.0	1.2	-	-	-	-
lung	23.6	0.38	394	-	-	-	-
muscle	56.9	0.81	1090	3421	5.75	0.96	563.6
fat	11.6	0.08	911	2348	0.38	0.51	76.7
bone	13.1	0.09	1908	1313	0.32	0.15	10.0
cerebrum	56.8	0.75	1045	3696	6.40*	15.5+	10992
grey matter	56.8	0.75	1045	3696	6.40*	15.5+	10992
white matter	41.7	0.45	1041	3583	5.63*	4.34+	3072
CSF	70.6	2.26	1007	4096	6.71*	-	-
cerebellum	55.1	1.05	1045	3653	5.92*	15.7+	11088
brainstem	41.7	1.05	1046	3630	6.00*	11.4+	8043
myelum	35.0	0.46	1075	3630	6.00*	2.48+	2309
sclera	57.4	1.01	1032	4200	6.79*	5.89+	5472
lens	37.3	0.38	1076	3133	4.97*	-	-
vitreous humor	69.0	1.53	1005	4047	6.96*	-	-
optical nerve	35.0	0.46	1075	3613	5.73*	2.48+	2309
cartilage	45.1	0.60	1100	3568	0.49	0.54	35.0
thyroid gland	61.3	0.89	1050	3609	0.52	87.1	5624.3
tumor	59.0	0.89	1050	3950	0.97	-	1146.0

ϵ_r: relative permittivity [-], σ_eff: effective conductivity [S m^{-1}],
ρ: density [kg m^{-3}], c: specific heat capacity [J kg^{-1} °C^{-1}],
k: thermal conductivity [W m^{-1} °C^{-1}], Q: metabolic heat
generation rate [W kg^{-1}], ω: perfusion rate [ml min^{-1} kg^{-1}],
GTV: gross tumor volume, Blood heat capacity ($\rho_\mathrm{b}c_\mathrm{b}$) =
$4.1 \cdot 10^6$ [J m^{-3} °C^{-1}].

3.2.4 Evaluation parameters

To quantify the inter-observer variation in tissue segmentation for each imaging modality, we used the modified 3D Hausdorff surface distance[31], which we will call mean surface distance (MSD). For each imaging modality, patient and tissue, MSD is determined for observer 1 - observer 2, observer 1 - observer 3 and observer 2 - observer 3. The average over these three MSD values was reported as the inter-observer variation of the tissue

segmented in that imaging modality. The range of this average value per patient was reported using a box plot.

To quantify the effect on HTP of the CT and CT & MRI based patient models, we evaluated different temperature measures, i.e. T_{max}, T_{mean}, T10, T20, T50 and T90. T_{max} and T_{mean} were defined as the maximum and mean temperature in the manually segmented thermo-sensitive tissues. The T10, T20, T50 and T90 were defined as the temperature which is exceeded by either 10%, 20%, 50% or 90% of the simulated temperatures values inside the manually segmented thermo-sensitive tissues. In case of the CT & $MRI_{obs1,db}$ patient model, the thermo-sensitive tissues also includes the grey matter and white matter, but not the CSF because there are no nerves in CSF and therefore we do not regard it as a thermo-sensitive tissue. Since SAR is the current clinical practice, we report along with these temperature measures the corresponding peak SAR, using the commonly used 1g-averaged standard [IEEE/IEC62704-1] as calculated in SEMCAD X (v. 14.8.6, Schmid & Partner Engineering AG, Zurich, Switzerland).

Similar to previous studies[5,42,106], statistical significant difference (p<0.05) was tested using a non-parametric Wilcoxon signed rank test[109].

3.3   Results

In Figure 3.2 the observer variation in segmentation of the tissues in CT, MRI-T1 and MRI-T2w images is quantified with the MSD. A significant reduction in segmentation variation was found when using MRI for: cerebellum (MRI-T1w or MRI-T2w), brainstem (MRI-T1w or MRI-T2w), myelum (MRI-T1w or MRI-T2w, but MRI-T2w was significantly lower than MRI-T1w) and vitreous humor (MRI-T2w). Segmenting the sclera on MRI-T2w images gave a significant reduction in segmentation variation compared to MRI-T1w images, but not compared to CT images. Using CT images for segmentation of the optical nerve significantly reduced segmentation variation compared to MRI-T1w and MRI-T2w images. Therefore, for the temperature simulations, we choose to segment all tissues from MRI-T2w images except the optical nerve since for this tissue a lower variation was obtained using CT images.

Figure 3.3 shows examples of the manual segmented tissues of observer 1, 2 and 3 on CT, MRI-T1w and MRI-T2w. Figure 3.3a-c illustrates that the cerebrum could be reproducibly segmented on all modalities. Figure 3.3d-f illustrates that the lowest variation in cerebellum and brainstem could be found in MRI-T1w and MRI-T2w images. Since cerebellum and brainstem were more reproducibly segmented on MRI, also the cerebrum was segmented more reproducible in this region, but this did not lead to significant differences for the segmentation of cerebrum. Figure 3.3g-i illustrates that the myelum could be segmented with the lowest variation in MRI-T2w images, which is probably due to the bright contrast of CSF surrounding the myelum. Figure 3.3j-l illustrates that there was not much difference between CT and MRI for segmentation of the lens. Further, it illustrates that the sclera and vitreous humor could be segmented most reproducible on MRI-T2w. Figure 3.3l illustrates that large observer variation in segmentation of the

optical nerve could be found when using MRI.

Figure 3.4. shows the maximum temperature (T_{max}) and the corresponding peak 1g-SAR in the eight manually segmented thermo-sensitive tissues for five different patient models: 1) CT_{auto}, 2-4) CT & MRI_{obs1-3}, 5) CT & $MRI_{obs,db}$. A significant difference in predicted temperature was obtained when including the detailed brain structures. This significant difference was not found in the corresponding SAR. We only report T_{max} since the evaluation of the other temperature measures led either to no significant changes (i.e. T10, T20, T50 and T90) or similar significances (T_{mean}) as for T_{max}. The reported temperatures were obtained after a, per-patient, optimization of the total input power, which was on average over all patients 617 ± 152 W (mean $\pm$ 1 standard deviation).

Figure 3.5 exemplifies the impact of tissue segmentation on the simulated temperature. It shows for one patient, the temperature profile overlaid on the CT scan for a patient model generated using CT only, CT & MRI and CT & MRI including a detailed brain segmentation. The temperature profile does not change when using either CT only or combined CT & MRI segmentation, however, the simulated profiles are effected when including also GM, WM and CSF to the CT & MRI segmentation.
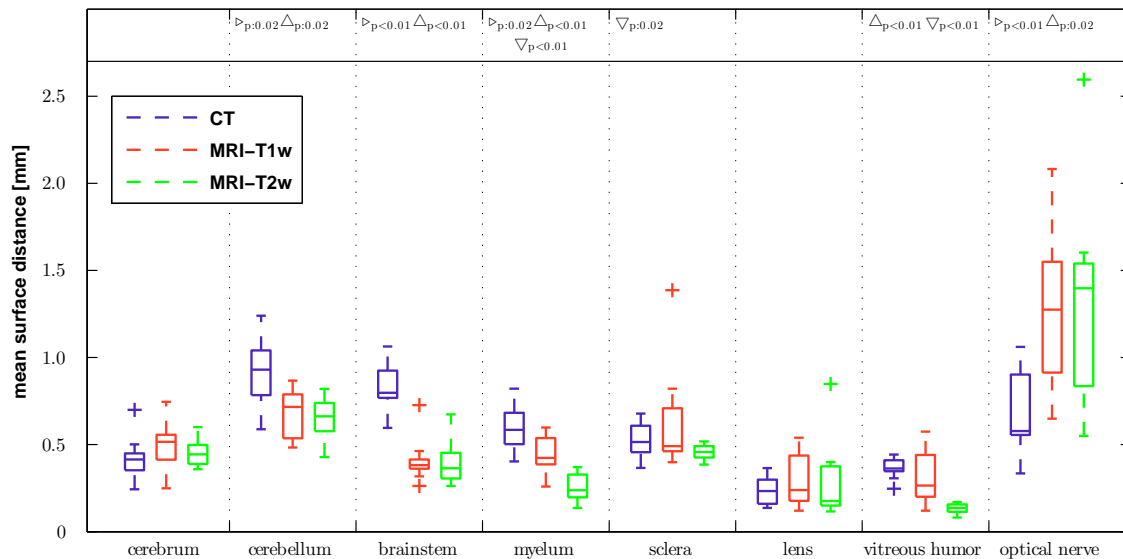

Figure 3.2: The manual inter-observer segmentation variation quantified by the mean surface distance for the cerebrum, cerebellum, brainstem, myelum, sclera, lens, vitreous humor and optical nerve. Statistical significant differences and p-values are indicated for CT vs. MRI-T1w ($\triangleright$), CT vs. MRI-T2w ($\triangle$), MRI-T1w vs. MRI-T2w ($\triangledown$). In the box-plots, the central mark is the median, the edges are the 25th and 75th percentiles, the whiskers extend to the most extreme data points not considered outliers (99.3%) and outliers are plotted individually (+).
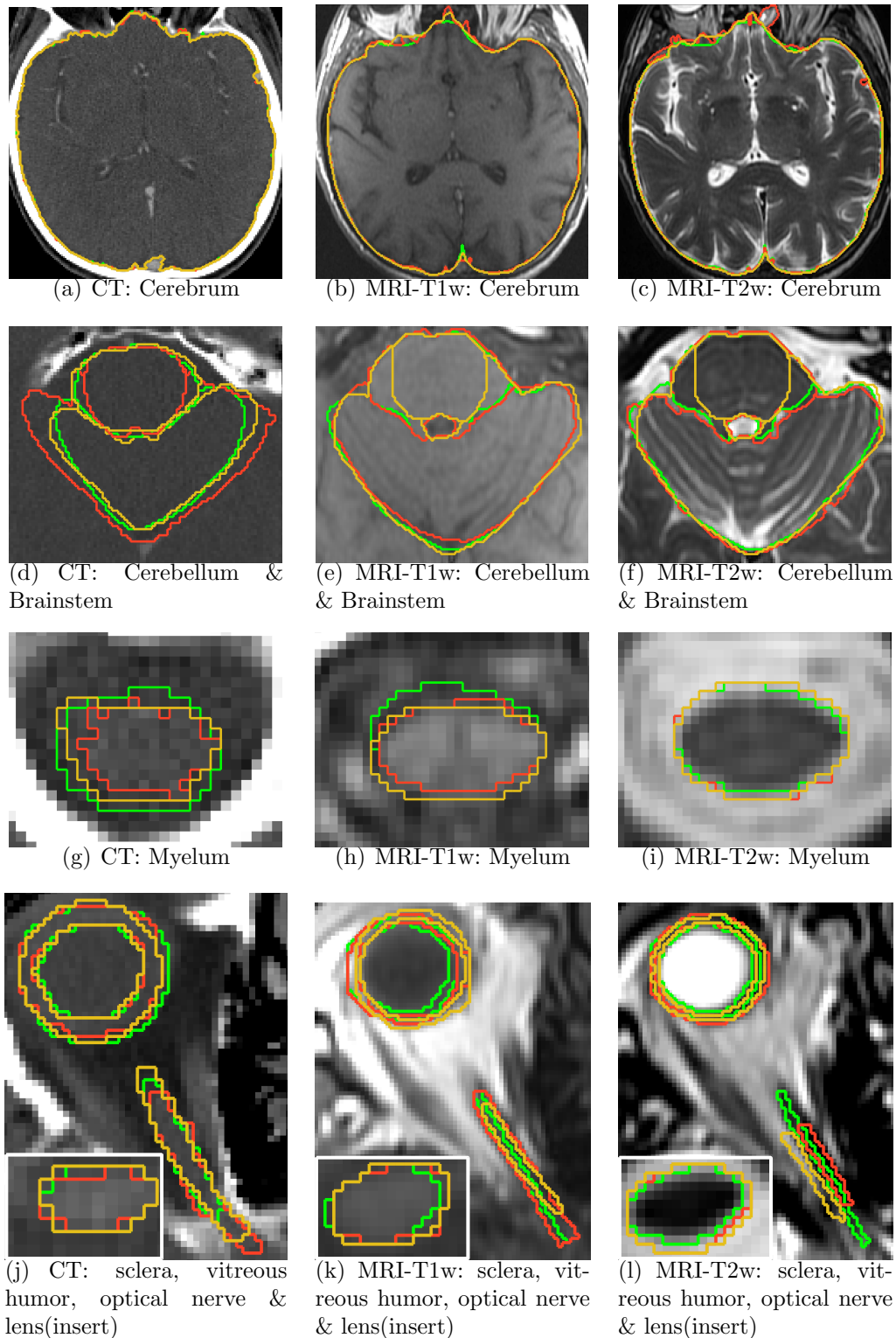
(a) CT: Cerebrum   (b) MRI-T1w: Cerebrum   (c) MRI-T2w: Cerebrum

(d) CT: Cerebellum & Brainstem   (e) MRI-T1w: Cerebellum & Brainstem   (f) MRI-T2w: Cerebellum & Brainstem

(g) CT: Myelum   (h) MRI-T1w: Myelum   (i) MRI-T2w: Myelum

(j) CT: sclera, vitreous humor, optical nerve & lens(insert)   (k) MRI-T1w: sclera, vitreous humor, optical nerve & lens(insert)   (l) MRI-T2w: sclera, vitreous humor, optical nerve & lens(insert)

Figure 3.3: Example of manual segmentations on CT, MRI-T1w and MRI-T2w images for cerebrum (a-c), cerebellum and brainstem (d-f), myelum (g-i) and for sclera, vitreous humor, optical nerve and lens (j-l). The colors indicate the segmentation of each observer: observer 1 (green), observer 2 (red), observer 3 (yellow).
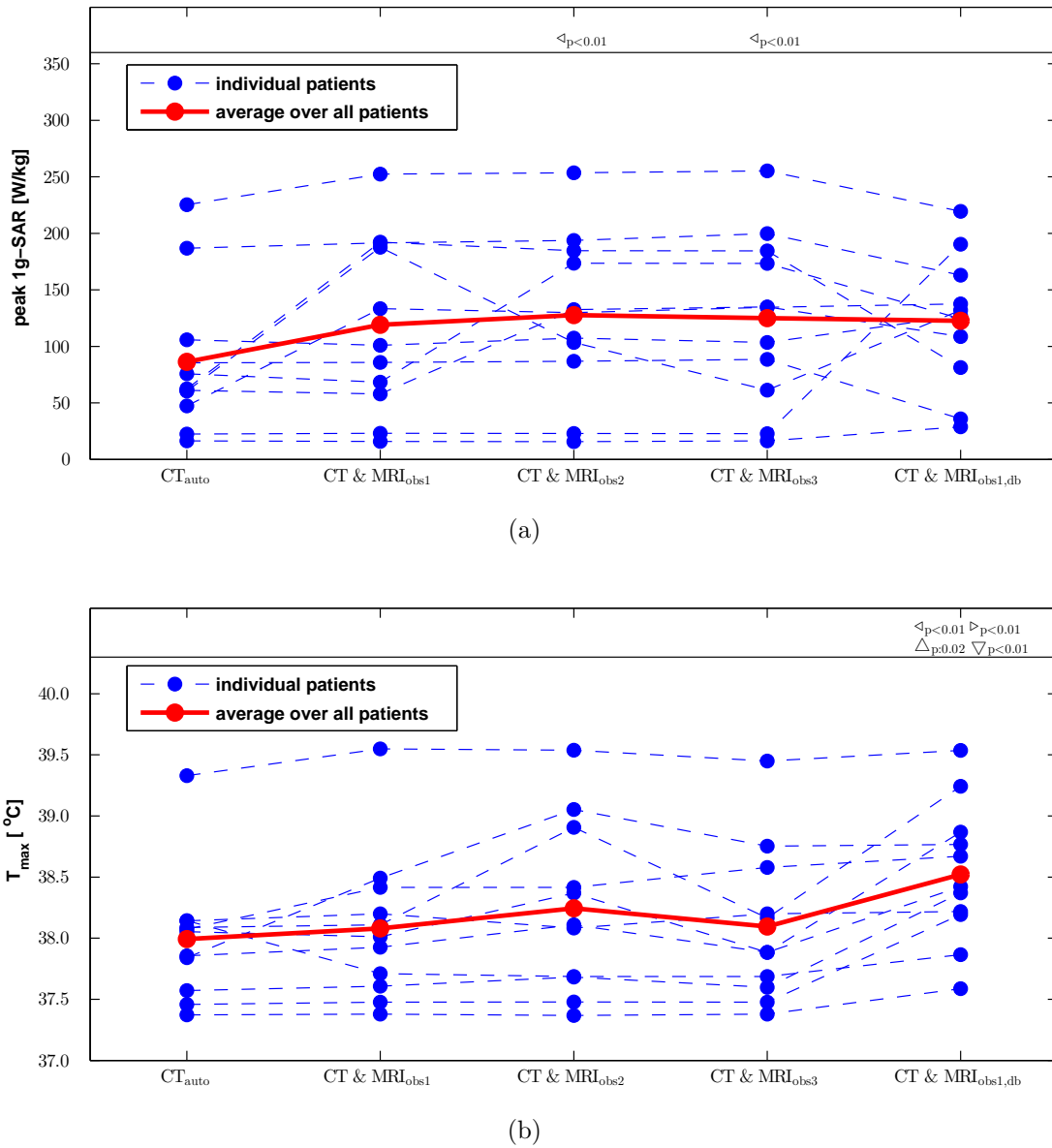
(a)

(b)

Figure 3.4: The patient-specific (blue) and patient-group averaged (red) values are shown for the specific absorption rate, SAR (a), and the maximum temperature, T_{max} (b), in the eight manually segmented thermo-sensitive tissues. The SAR and T_{max} are shown for patient models based on tissue segmentations from CT, CT & MRI observer 1, 2 and 3 (CT & MRI_{obs1}, CT & MRI_{obs2} and CT & MRI_{obs3}) and CT & MRI with detailed brain including white matter, grey matter and CSF (CT & $MRI_{obs1,db}$). In case of the CT & $MRI_{obs1,db}$ patient model, the thermo-sensitive tissues also includes the grey matter and white matter, but not the CSF because there are no nerves in CSF and therefore we do not regard it as a thermo-sensitive tissue. The reported SAR is the peak 1g-SAR corresponding to the reported T_{max}. Statistical significant differences and p-values are indicated with respect to CT ($\triangleleft$), CT & MRI_{obs1}($\triangleright$), CT & MRI_{obs2}($\triangle$) and CT & MRI_{obs3}($\triangledown$).

(a) SAR: CT_auto

(b) T: CT_auto (similar to CT & MRI_obs1−3)
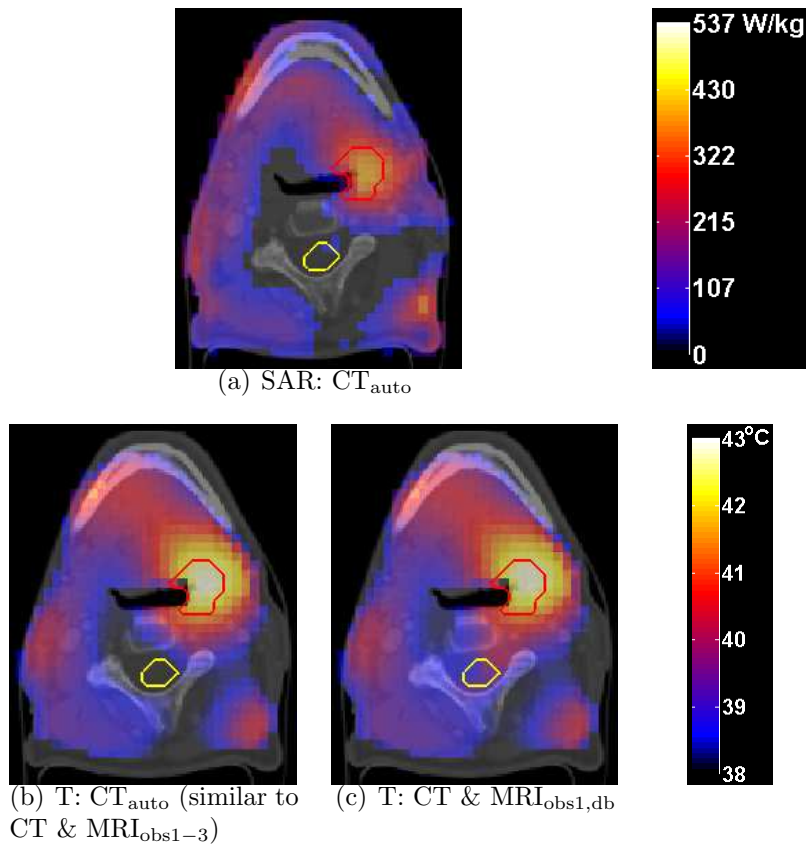
(c) T: CT & MRI_obs1,db

Figure 3.5: Example of simulated SAR (a) and temperature (T) (b,c) profiles projected on an axial slice of the CT. The red contour indicates the target and the yellow contour indicates the myelum. In the temperature maps three hotspots in normal tissue are visible: two at the bottom and one in the mandible caused by metal implants. In the temperature profile of CT & MRI_obs1,db the temperature in the myelum is increased due to the presence of GM, WM and CSF. Note that the SAR at the skin does not result in high temperatures at the skin due to cooling by the waterbolus. The colorscale of the SAR distribution is from black (0 W/kg) to white (537 W/kg) and for the T distribution from black (38 °C) to white (43 °C).

3.4   Discussion

In this study, we investigated the CT and MRI based inter-observer segmentation variation and the effect of this variation on the simulated temperature, using either CT or combined CT and MRI based patient models. MRI based segmentation led to a similar or higher reproducibility for segmentation of the cerebrum, cerebellum, brainstem, myelum, sclera, lens and vitreous humor, while CT-based segmentation is more reproducible for

the segmentation of the optical nerve. This could be explained, because the optical nerve appears different on MRI compared to CT. The layer surrounding the optical nerve, i.e. the dura, is also visible in MRI due to the improved soft-tissue contrast, while in CT the optical nerve and dura both have the same contrast, which leads to a lower segmentation variation when comparing CT with MRI. Although segmentation on MRI was more reproducible for most of the tissues, there was no significant difference in the simulated temperature between CT and MRI-based models. However, when extending the tissue list with GM, WM and CSF a significant change in the simulated temperature was found. The corresponding SAR did not change significantly. This indicates that the current clinical patient model generation for H&N HTP, i.e. automatic CT-based segmentation, can be improved by extending it with MRI based detailed brain segmentation when temperature predictions are used.

Previous studies that quantified the manual inter-observer variation for H&N radiotherapy treatment planning provide an excellent reference for our results regarding segmentation variation. Ahmed et al.[5] concluded that MRI-based segmentation of the brainstem and the myelum significantly improves organ definition, which is in agreement with our results. For the myelum, this advantage was also found by Geets et al.[42]. They quantified the inter-observer variation with a coefficient of variation (CV) which is defined as the ratio between the standard deviation and the mean of the tissue volume. A CV of 5.8% for MRI-T1w and 10.2% for CT based segmentation of myelum (19 patients, 3 observers) was reported, compared to a CV for MRI of 8.4% (MRI-T1w) and 7.0% (MRI-T2w) and from CT of 14.8%, as found in our study. For the cerebrum, de Boer et al.[25] report a manual inter-observer (6 patients and 2 observers) similarity coefficient[30] of 0.98 using MRI-T1w images, compared to 0.98 (MRI-T2w) and 0.97 (MRI-T1w) in our study. Note that we determined the evaluation measures CV and the similarity coefficient from our results and not report them in the results section, but only use them here to be able to compare our results with literature. In our previous study[106] the CT-based manual segmentation variation of the same tissues for H&N HTP were determined. When comparing those result (7 patients and 3 observers) with the current results, the inter-observer variation was significantly higher in the previous study for all tissues, except for the optical nerve. In that study, no fixed display windowing settings were applied, which might explain this difference. Hence, well-defined segmentation protocols reduce segmentation variation. In general, for those tissues that we could compare, the variations in tissue segmentation reported by our study are in agreement with the results of previous studies.

As evaluation parameter for HTP quality, we used a temperature based parameter instead of the more commonly used SAR based parameters. In a previous study[106], we showed that the effect of CT-based inter-observer variation on the SAR-based HTP quality was minor. The inter-observer segmentation variation in that study was even larger than reported in this study, both for CT as MRI-based segmentation. Therefore, we expected that the effects of CT and MRI-based inter-observer variation on SAR-based HTP quality would be negligible. In hyperthermia, temperature increase has been correlated with treatment outcome[38,94]. Further, temperature simulation accuracy has recently been improved by the introduction of optimized thermal tissue parameters[107]. Therefore, our

first choice evaluation parameter is not a SAR-based but a temperature based parameter. However, we do report SAR as it is still the current clinical practice.

In our previous study[106], we did find an effect, although minor, of segmentation variation on the local SAR dose. In the current study, for 2 out of 3 observers a significant but small increase in SAR was found. This increase was not present in the simulated temperature because thermal conduction spreads out local SAR peaks. This suggests that small variations in segmentation have more effect on the simulated local SAR than on the simulated local temperature.

In our results, we report a significant different temperature when comparing patient models based on CT (T_{max} : 38.0 °C) and CT-MRI (T_{max} : 38.1 °C) with patient models based on CT & $MRI_{obs1,db}$ (T_{max} : 38.5 °C). This means that the predicted temperature increases 0.5 °C with respect to CT based models, which is the current clinical standard. As the goal of hyperthermia is to heat tumors from 37 °C to 43 °C, this 0.5 °C is thus 8% of the total aimed temperature increase of 6 °C (43 - 37 °C), hence a clinically relevant increased predicted temperature[38]. Note that a 0.5 °C difference at 38 °C may not have clinical significance, but the temperature uncertainties obtained in this study can be relevant for treatment planning guided hyperthermia. The 0.5 °C is an average increase, and this increase can exceed 1 °C in specific patients. The relevance of this increase for treatment planning guided hyperthermia was demonstrated by simulations for an example patient with an advanced nasopharynx tumor close to thermo-sensitive tissues. Note that this patient is a representative example since nasopharynx tumors nearby one of the thermo-sensitive tissues are present in approximately 10% of the patients treated with head and neck hyperthermia combined with re-irradiation thus far. For this patient, total input power on the CT-based patient model was optimized using the thresholds as in the paper, i.e. 40 °C (thermo-sensitive tissue) and 45 °C (normal tissue). Optimization resulted in an optimized maximum temperature in the target of 42.9 °C, which was constrained by the threshold of 40 °C in thermo-sensitive tissue. Since no MRI was available for this patient, we applied a temperature difference of +0.5 °C and -0.5 °C on the threshold of the thermo-sensitive tissues to mimic the case of a MRI-based patient model including a detailed brain. This led to a maximum target temperature of 41.7 °C (-0.5 °C) and 44oC (+0.5 °C). Thus, as soon as thermo-sensitive tissues become a limiting factor in the total input power optimization, a 0.5 °C change can be detrimental for the thermal dose in the target. In general, we can state that subtle changes in predicted temperatures can strongly influence the predicted thermal dose in the target since thermal dose is exponentially dependent on temperatures above 43 °C, i.e. according to Arrhenius′ CEM43 dose[29,80]. Hence, even small errors in temperature predictions affect the effectiveness of dosimetry, and possibly optimization, in temperature simulation guided hyperthermia.

Although improved accuracy has not been validated using measurements, we hypothesize that adding brain tissues will increase accuracy since tissue heterogeneity, i.e. the number and location of tissue transitions, is more realistically captured[26,77,106]. In future studies, the actual tissue temperatures could be measured to verify our findings. Note that such validation is difficult by using the invasive probes that we now use in the clinic. 3D MRI thermometry may have more potential for capturing all influences of tissue

transitions, but such technology is currently unavailable for head and neck hyperthermia.

In previous studies, the uncertainty of tissue parameters on the predicted temperatures have been reported. For temperature simulations in deep hyperthermia in the pelvic region, Canters et al[16]. reported a temperature change of $\pm$ 1 °C caused by the uncertainty of thermal tissue parameter values that ranged from 1-30 %. In the same region, de Greef et al.[27] found deviations upto 2.9 °C when varying the tissue perfusion $\pm$ 25 % and $\pm$ 50 %. In another study, de Greef et al.[28] investigated the combined effect of perfusion and dielectric uncertainty on simulated temperature, which resulted in temperature increases of 0.5 upto 1.5 °C. In our study, the reported inter-observer variation in segmentation of MRI led to a temperature difference of 0.2 $\pm$ 0.2 °C (mean $\pm$ 1 standard deviation). This is obtained by computing the mean and 1 standard deviation over the differences in T_{max} using CT & MRI based patient models of observer 1, 2 and 3, as shown in Figure 3.4. In general, this uncertainty is slightly lower as the uncertainty caused by tissue property variations as reported in previous studies.

It could have been expected that the simulated temperatures increase in patient models that include a detailed brain segmentation. In patient models with a detailed brain segmentation, the cerebrum and cerebellum are replaced by GM, WM and CSF. The increased number of tissues results in more tissue inhomogeneities, and hence SAR hotspots at tissue transitions. Further, the perfusion in cerebrum (763.3 ml min^{-1} kg^{-1}) is equal or higher than the perfusion in GM (763.3 ml min^{-1} kg^{-1}), WM (213.3 ml min^{-1} kg^{-1}) and CSF (0 ml min^{-1} kg^{-1}). The effective conductivity of CSF is three times higher as in the cerebrum, resulting in an increased storage of energy, and probably a high local SAR in this tissue. Together with the lack of perfusion in CSF, this results in increased temperatures in this tissue and thus also in those patient models that include a detailed brain segmentation, as confirmed by our analysis.

3.4.1 Limitations of the study

A number of factors could have influenced our results. First, in our MRI protocol the first three patients were scanned with a H&N coil, while the other patients were scanned in a surface coil. In the surface coil, their is a considerable bias in image contrast in every slice, as can be seen in Figure 3.3, which could have influenced the manual segmentation. However, we found no significant difference in inter-observer variation when comparing those three patients to the others. In addition, the advantage of using this coil is that patients can be scanned in treatment position using the immobilization mask. Second, halfway the study we had to adapt the MRI protocol to increase the field of view for larger patients. This slightly changed the in-plane resolution of the MRI, which might have influenced the results. However, also no significant difference was observed in inter-observer segmentation variation when comparing the group with the lower in-plane resolution with the group with the higher in-plane resolution, indicating that also this influence was minor. Third, the T1w images were not segmented from scratch, but by using the MRI-T2w segmentation as a starting point, while CT and MRI-T2w images were segmented from scratch. Therefore, there might be a bias in the segmentation of

the MRI-T1w images with respect to the MRI-T2w images. Although these factors might have influenced our results, the conclusion that the use of MRI segmentation reduces inter-observer segmentation variation for most of the segmented tissues remains valid.

3.5   Conclusion

We investigated the relevance of using MRI in addition to CT for patient modeling in H&N HTP. Although MRI reduces the inter-observer variation in most tissues, we found no effect on the predicted local tissue temperatures and a minor effect on the local tissue SAR. Inclusion of detailed brain structures does not affect the SAR, however, it does affect the temperature predictions. These findings make MRI relevant for patient modeling in H&N HTP. Therefore, we will now develop a combined CT and MRI based auto-segmentation tool to improve the reproducibility, and possibly also the accuracy, of H&N HTP.

CHAPTER 4

Thermal tissue property optimization technique

Abstract

Purpose: *Hyperthermia treatment planning (HTP) is used in the head and neck (H&N) region for pre-treatment optimization, decision making and real-time HTP-guided adaptive application of hyperthermia. In current clinical practice, HTP is based on power-absorption predictions, but thermal-dose-effect relations advocate extension to temperature predictions. Exploitation of temperature simulations requires region- and temperature-specific thermal tissue properties due to the strong thermo-regulatory response of H&N tissues. The purpose of our work was to develop a technique for patient-group specific optimization of thermal tissue properties based on invasively measured temperatures, and to evaluate the accuracy achievable.*

Materials and methods: *Data from 17 treated patients were used to optimize the perfusion and thermal conductivity values for the Pennes-bioheat-equation-based thermal model. A leave-one-out approach was applied to accurately assess the difference between measured and simulated temperature (ΔT). The improvement in ΔT for optimized thermal tissue property values was assessed by comparison with the ΔT for values from literature, i.e. baseline and under thermal stress.*

Results: *The optimized perfusion and conductivity values of tumor, muscle and fat leads to an improvement of simulation accuracy (ΔT: $2.1 \pm 1.2^{\circ}C$) compared with the accuracy for baseline (ΔT: $12.7 \pm 11.1^{\circ}C$) or thermal stress (ΔT: $4.4 \pm 3.5^{\circ}C$) property values.*

Conclusions: *The presented technique leads to patient-group-specific temperature property values that effectively improve simulation accuracy for the challenging H&N region, thereby making simulations an elegant addition to invasive measurements. The rigorous leave-one-out assessment indicates that improvements in accuracy are required to rely only on temperature-based HTP in the clinic.*

4.1   Introduction

Phase-III clinical evidence shows a substantially improved clinical outcome when hyperthermia, i.e. induced elevation in tissue temperature to $39-44$ºC, is added to radiotherapy treatment of head and neck (H&N) tumors, without inducing additional toxicity[51,53,100]. Based on this evidence, we developed the HYPERcollar applicator system to extend the treatment of H&N tumors to regions deeper than 4cm from the skin[78]. The HYPERcollar is a ring-shaped phased array hyperthermia applicator consisting of twelve antennas uniformly divided over two rings of six antennas, which can be individually controlled and operate at a frequency of 434MHz. Treatments with this applicator are pre-planned using hyperthermia treatment planning (HTP) for settings optimization and decision making, and to apply our real-time adaptive hyperthermia strategy[15,69,89]. Currently, HTP is based on electromagnetic (EM) simulations for predicting the energy deposition, i.e. specific absorption rate (SAR), in the patient. However, clinical outcome is related to the thermal-dose[38,94], which advocates using temperature predictions. In clinical practice, temperature simulations are not used for H&N HTP due to the absence of a sound validation.

Various simulation models to predict temperature have been developed[80]. In hyperthermia, temperature modeling is commonly based on the Pennes bioheat equation (PBHE)[82]. The PBHE models perfusion by a heat sink; but the direction of blood flow and heat exchange between large vessels and tissues are not included. The discrete vascular (DIVA) model[63] is a more physiologically correct model as it includes vessel networks. However, the integration of representative vessel networks in the simulation is a lengthy and tedious procedure, which prevents application of this approach in clinical practice.

Thermal tissue parameters of normal[47] and tumor[55,59,76] tissue, at rest and under thermal stress[95], are used as input for the temperature model. These parameters are usually taken from literature. The reported values vary substantially, especially regarding perfusion and thermal conductivity, which have been shown to deteriorate temperature simulation accuracy[8,16].

The purpose of this study is to develop a technique for rigorous optimization of thermal tissue properties, and to establish the accuracy of temperature simulations for H&N hyperthermia patients when applying these patient-group specific properties.

4.2   Methods

4.2.1   Patient selection

Over the past 7 years, 45 patients have been treated with H&N hyperthermia in our institution. In 18 patients, catheters for invasive temperature monitoring were inserted for measurements using a fiber-optic temperature probe system (FISO evolutions: www.fiso.com). One patient with an anaplastic carcinoma of the thyroid gland was excluded from this study, since this tumor is too heterogeneous to allow assuming homogen-

eity in tissue properties in the tumor. In total 17 patients (25 treatments) were included in the study and the tumors were in the following locations: thyroid gland, trachea, parotid gland, larynx, oropharynx and nasopharynx (Table 4.3).

4.2.2 Computed Tomography (CT) Images

Two CT scans were made for each patient[79]: CT1) for treatment planning, acquired approximately one week before treatment (CT_{HTP}); CT2) for reconstruction of the temperature measurement points from the catheter track, acquired at the day of catheter placement (CT_{Tcat}). CT_{Tcat} has a higher resolution (in-plane between 0.3x0.3mm 1.0x1.0mm, slice thickness between 0.5-3.0mm) than CT_{HTP} (in-plane between 0.8x0.8mm 1.0x1.0mm, slice thickness between 1.5-3.0mm).

4.2.3 Reconstruction of Temperature Measurement Points

The catheter track was reconstructed by manually clicking points on CT_{Tcat}, from the skin towards the tip of the catheter. Then, the points were transformed to CT_{HTP} using an image-based registration strategy[34]. A cubic spline was fitted through the points on CT_{HTP} to determine the length of the catheter track. The insertion depth was measured prior to treatment. During treatment, a FISO probe with measurement points spaced 2cm apart, were inserted in the catheter. The locations of these points, the spline and the insertion depth allowed to reconstruct the location of the measurement points and to import them into our treatment planning software SEMCAD X (v. 14.8.4, Schmid & Partner Engineering AG, Zurich, Switzerland). The sensitivity of this procedure was assessed using CTs of 13 patients and showed an inter-observer reproducibility of 2.5±1.3mm.

4.2.4 Hyperthermia Treatment Planning (HTP)

CT_{HTP} was converted into a 3D patient model by automatically segmenting normal and critical tissues using a multi-atlas approach combined with intensity modeling[34]. The tumor and the target were both manually segmented by an H&N radiation oncologist, as in[106]. EM and thermal tissue properties were assigned according to the values reported in Table 4.1. HTP was performed as described by Rijnen et al.[89].

4.2.5 Temperature simulation

The steady state PBHE-based thermal solver (grid size: 2mm, maximum iterations: 1000, relative tolerance: 1e-8) in SEMCAD X was used to simulate the temperature in the tissues listed in Table 4.1. To account for energy losses, we applied a mix of convective and Neumann (fixed flux) boundary conditions at interfaces of tissue-surrounding air (convection coefficient: 8 [W m^{-2} °C^{-1}],[8]), tissue-internal air and tissue-lung (convection

Table 4.1: EM and thermal tissue properties at 37°C, baseline. For normal tissue we used the database from [47] and for tumor tissue we used the average values reported in [55,56,59,76,78].

Tissue	ϵ_r	σ_{eff}	ρ	c	k	Q	ω
internal air	1.0	0.0	1.2	-	-	-	-
lung	23.6	0.38	394	-	-	-	-
muscle	56.9	0.81	1090	3421	See Table 4.2	0.96	See Table 4.2
fat	11.6	0.08	911	2348	See Table 4.2	0.51	See Table 4.2
bone	13.1	0.09	1908	1313	0.32	0.15	10.0
cerebrum	56.8	0.75	1045	3696	0.55	15.5	763.3
cerebellum	55.1	1.05	1045	3653	0.51	15.7	770.0
brainstem	41.7	0.45	1046	3630	0.51	11.4	558.6
myelum	35.0	0.46	1075	3630	0.51	2.48	160.3
sclera	57.4	1.01	1032	4200	0.58	5.89	380.0
lens	37.3	0.38	1076	3133	0.43	-	-
vitreous humor	69.0	1.53	1005	4047	0.59	-	-
optical nerve	35.0	0.46	1075	3613	0.49	2.48	160.3
cartilage	45.1	0.60	1100	3568	0.49	0.54	35.0
thyroid gland	61.3	0.89	1050	3609	0.52	87.1	5624.3
tumor	59.0	0.89	1050	3950	See Table 4.2	-	See Table 4.2

ϵ_r: relative permittivity [-], σ_{eff}: effective conductivity [S m^{-1}], ρ: density [kg m^{-3}], c: specific heat capacity [J kg^{-1} °C^{-1}], k: thermal conductivity [W m^{-1} °C^{-1}], Q: metabolic heat generation rate [W kg^{-1}], ω: perfusion rate [ml min^{-1} kg^{-1}], GTV: gross tumor volume, Blood heat capacity $(\rho_b c_b) = 4.1 \cdot 10^6$ [J m^{-3} °C^{-1}].

coefficient: 50 [W m^{-2} °C^{-1}],[8]), and tissue-waterbolus (convection coefficient: 82 [W m^{-2} °C^{-1}],[102]). The initial temperature in the tissues was set to 37°C while the temperature of the surrounding air and the waterbolus was set to 20°C. By definition, a steady state temperature (T_{SS}) was reached when the temperature did not change more than 0.2°C in maximal 40 seconds before a power-off. The power and phase settings at T_{SS} were applied to each antenna and the resulting SAR served as a source to the temperature simulation, assuming an antenna efficiency of 100%. Throughout this paper, we used four sets of values for thermal tissue properties, i.e. perfusion (ω) and thermal conductivity (k): 1) baseline values from literature; 2) thermal stress values from literature; 3) patient-group optimized values; and 4) patient-specific optimized values. In figure 4.1, for one patient, the treatment power, measured temperature with T_{SS} points and CT with simulated temperature distribution at one T_{SS} for patient-group optimized values is shown.

4.2.6 Parameter optimization

Perfusion (ω) and thermal conductivity (k) were simultaneously optimized for muscle, fat and tumor by minimizing the cumulative error between measured and simulated temper-
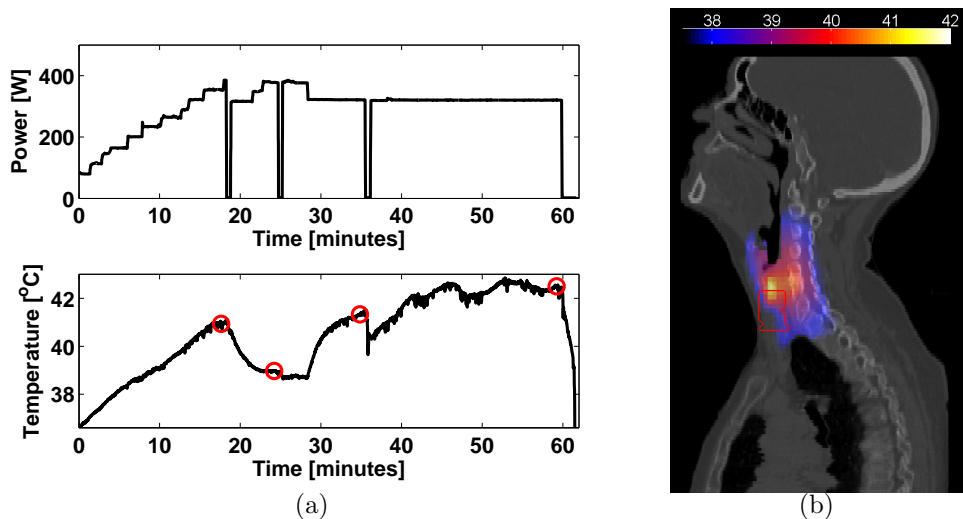
Figure 4.1: Example (patient 4) of the total power applied to the 12 antennas and measured temperature for one probe during treatment. The red circles indicate occasions where the temperature profile was relatively flat, i.e., the steady-state temperature (T_{SS}) points. On the right, the temperature distribution at T_{SS}=59min for optimized thermal tissue properties is shown on top of the CT HTP. The red line indicates the target region. Note: the target region is not completely covered, which might have been corrected for when temperature predictions were clinically available.

ature points at T_{SS}. A constrained non-linear optimization function[66] '*fminsearchbnd*' in MATLAB (v. R2013a, MathWorks, Natick, Massachusetts, USA) was used with a lower bound perfusion: 1 [ml min^{-1} kg^{-1}], lower bound thermal conductivity: 0.01 [J kg^{-1} °C^{-1}], maximum iterations: 150, relative tolerance: 1e-1. Figure 4.2 shows an example of the optimization and its results. Note that one optimization, including 150 iterations, took approximately 1.5 hours.

Per patient, we aimed for an equal number (± 20) of measurements points as input for the optimization ($T_{opt-input}$), but this was not possible for all patients due to a limited number of probe measurement points (T_{meas}). The number of $T_{opt-input}$ points was increased by including multiple T_{SS} points were we chose to include the T_{SS} points with the most T_{meas} points. The optimized patient-specific thermal tissue parameters were obtained by averaging over all these T_{SS}. Note that T_{SS} could be taken from different treatments, causing a change in T_{meas} due to different insertion depth or broken probes (thus $\#T_{meas} \times \#T_{SS} \neq \#T_{opt-input}$). For all patients, this resulted in a total of 313 $T_{opt-input}$ points. These points were distributed over muscle (56%), fat (27%) and tumor (17%) tissue, of which 42% are located superficial (probe depth < 1cm), 46% intermediate (1cm < probe depth < 4cm) and 12% deep (probe depth > 4cm), relative to the skin surface. Examples of the exact measurement locations were indicated in Paulides et al.[79].
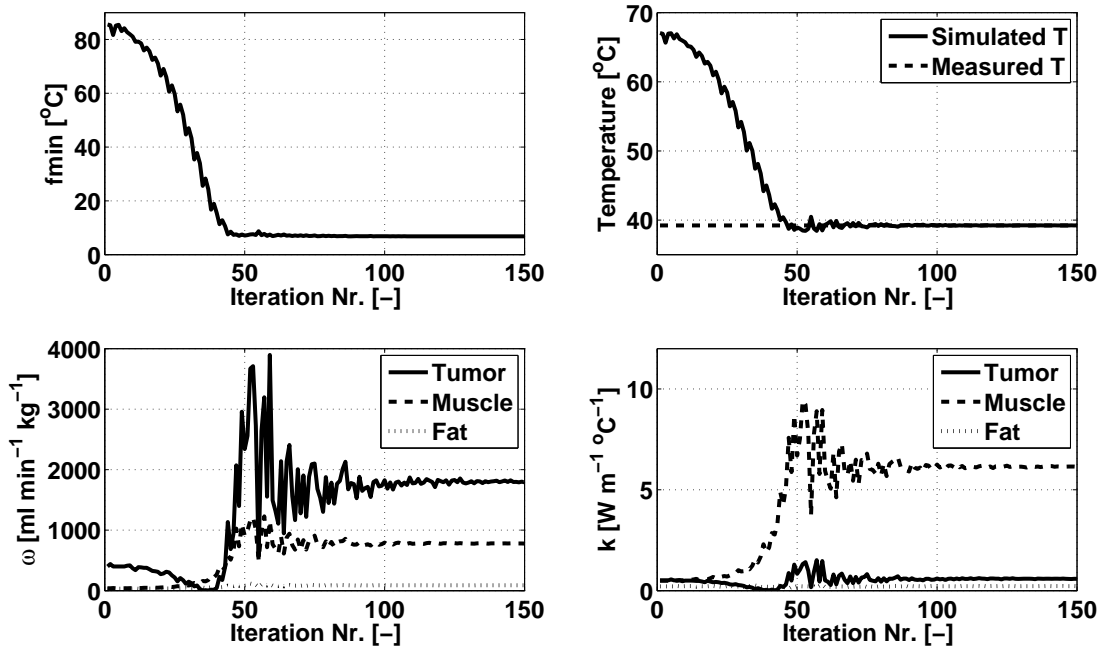
Figure 4.2: Example (patient 8) of the optimization process to show the convergence
rate. Reduction in the cumulative error for all measured and simulated
probes at T_{SS} (top left), and measured and simulated temperatures for
one measurement point (top right), at each iteration in the optimization.
Perfusion (ω) (bottom left) and thermal conductivity (k) (bottom right)
versus iteration number for tumor, muscle and fat tissue.

4.2.7   Parameter validation

The optimized perfusion and thermal conductivity parameters in muscle, fat and tumor
were validated in a leave-one-out experiment. In this experiment we used the data of a
single patient as the test data, and the data of the remaining patients as the training
data. This was repeated such that each single patient data was used once as the test data.
In this way, we could use all patients in our limited patient group for training and testing,
while we avoided over-tuning of the parameters with respect to our group of patients,
such that the validation holds for new patients.

To the test-set, we applied the average patient-specific perfusion and thermal conduct-
ivity over all patients, except its own. With these patient-group thermal tissue parameters
we determined the average temperature error for the evaluated measurement and simu-
lated temperature points (ΔT_{group}). The improvement in ΔT_{group} was assessed by com-
parison to the temperature error for tissue property values from literature, i.e. baseline
($\Delta T_{baseline}$) as well as under thermal stress (ΔTTstress).

In addition, we determined the average temperature error between the evaluated
measurement and simulated temperature points using patient-specific optimized para-

Table 4.2: Literature values for baseline[47,55,59,76] and thermal stress[95], as well as the optimized patient group values from this study for perfusion (ω) and thermal conductivity (k) in tumor, muscle and fat tissue.

	ω_{tumor}	ω_{muscle}	ω_{fat}	k_{tumor}	k_{muscle}	k_{fat}
Literature: baseline	400.0	39.1	32.7	0.51	0.49	0.21
Literature: thermal stress	80.0	300.0	200.0	0.64	0.64	0.21
Optimized (this study)	1146.0	563.6	76.7	0.97	5.75	0.38

ω: perfusion rate [ml min^{-1} kg^{-1}], k: thermal conductivity [W m^{-1} $^{\circ}$C^{-1}]

meters ($\Delta T_{patient}$). $\Delta T_{patient}$ represents the maximum accuracy you can attain with this technique. Furthermore, it was used to compare our results to other studies. We report the average temperature difference, and the averaged absolute temperature difference.
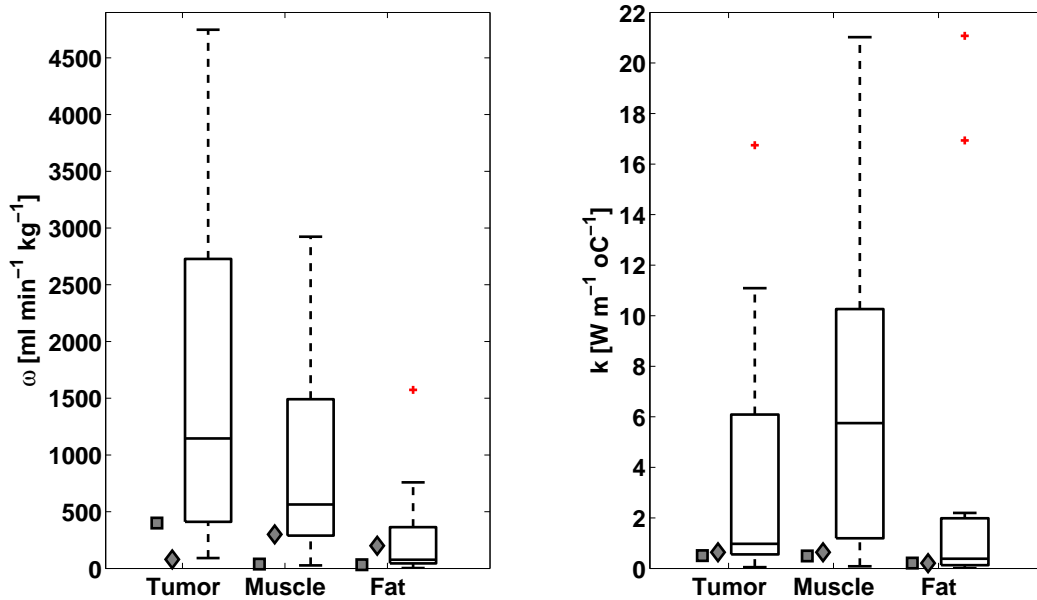
Figure 4.3: The range of patient-specific optimized perfusion (left) and thermal conductivity (right) values for tumor, muscle and fat. In addition, the baseline (squares) and thermal stress (diamonds) literature values are shown. On each box of the boxplot, the central mark is the median, i.e., the patient group values, the edges are the 25th and 75th percentiles, the whiskers extend to the most extreme data points not considered outliers (99.3%) and outliers are plotted individually (+).

Table 4.3: Results of the leave-one-out experiment. Per patient we report the tumor location, number of probe measurement points (T_{meas}) in a patient, number of optimizations (T_{SS}) and the number of probe measurement points used as input for the optimization ($T_{opt-input}$). For all probes per patient, the average error between measured and simulated temperature (ΔT) is given. In addition, the patient-averaged difference and patient-averaged absolute difference are given together with their one standard deviation.

Patient nr.	Tumor location	nr. T_{meas}	nr. T_{SS}	nr. $T_{opt-input}$	$\Delta T_{literature}[^{\circ}C]$ $\Delta T_{baseline}$	$\Delta T_{T-stress}$	$\Delta T_{optimized}[^{\circ}C]$ ΔT_{group}	$\Delta T_{patient}$
1	Larynx	3	3	5	1.3	0.6	1.1	-0.5
2	Oropharynx	5	5	23	-31.0	-12.2	-2.6	-0.2
3	Nasopharynx	4	7	28	-5.2	-5.9	0.2	0.2
4	Thyroid gland	7	4	28	-1.6	0.5	2.3	-0.7
5	Trachea	2	2	4	-1.1	-5.2	1.1	0.1
6	Oropharynx	5	4	17	-17.1	-1.9	-0.5	-0.3
7	Nasopharynx	2	7	14	-4.1	-0.9	0.8	-0.1
8	Parotid gland	4	5	20	-15.2	-2.4	0.0	0.4
9	Oropharynx	11	2	21	-27.2	-9.6	-3.0	0.4
10	Oropharynx	3	6	12	-0.9	1.6	2.9	-0.4
11	Oropharynx	6	4	23	-15.0	-3.8	-1.6	0.3
12	Thyroid gland	5	4	20	-24.0	-3.7	-0.5	-1.3
13	Oropharynx	7	3	21	-36.4	-11.8	-5.2	0.2
14	Thyroid gland	6	4	23	-4.2	-0.7	1.5	0.1
15	Thyroid gland	6	4	21	-6.6	-0.4	0.9	1.0
16	Nasopharynx	5	6	23	-2.0	-3.9	-0.3	-0.1
17	Oropharynx	1	10	10	-12.8	-1.5	2.3	-0.0
Average difference ± one standard deviation					-12.0±11.7	-3.6±4.2	0.0±2.1	0.0±0.5
Average absolute difference ± one standard deviation					12.7±11.1	4.4±3.5	2.1±1.2	1.0±0.7

$\Delta T_{baseline}$ simulated temperature based on literature baseline values, $\Delta T_{T-stress}$ simulated temperatures based on literature thermal stress values, ΔT_{group} simulated temperatures based on patient group optimized values, using a leave-one-out approach, $\Delta T_{patient}$ simulated temperatures based on patient-specific optimized values.
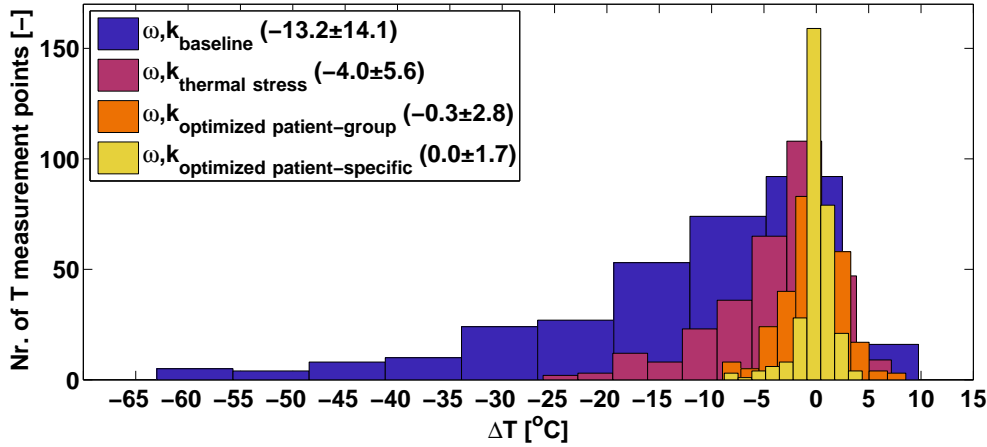
Figure 4.4: Histogram of the error between measured and simulated temperature (ΔT) when using the baseline (blue), thermal stress (pink), patient group optimized (orange), or patient specific optimized (yellow) perfusion (ω) and thermal conductivity (k) values including all 313 evaluated points. In the inset the mean $\pm$ one standard deviation of each histogram is given.

4.3   Results

Figure 4.3 shows the spread of the average patient-specific optimized perfusion and thermal conductivity values for tumor, muscle and fat. Most of the optimized median, i.e. patient-group, values were in the same range as the literature baseline and thermal stress values, but the tumor perfusion and muscle thermal conductivity were considerably larger, as shown in Table 4.2. When these patient-group optimized tissue property values for tumor, muscle and fat were used in a simulation, the average absolute difference between measured and simulated temperatures (ΔT_{group}: 2.1±1.2°C, mean $\pm$ one standard deviation) was reduced compared to using literature baseline ($\Delta T_{baseline}$: 12.7±11.1°C) or thermal stress ($\Delta T_{T-stress}$: 4.4±3.5°C) values in the simulation, as shown in Table 4.3. The maximum accuracy that can be obtained with this technique, when using the patient-specific optimized property values, is even higher ($\Delta T_{patient}$: 1.0±0.7°C). For the literature baseline and thermal stress values the average differences are below 0°C, i.e. for literature values the simulations yield higher temperatures than the measurements. Figure 4.4 summarizes the results of Table 4.3 by showing for all 313 evaluated temperature measurement points the distribution of the average ΔT for literature baseline, literature thermal stress, patient-group and patient-specific optimized tissue property values.

4.4   Discussion

A technique to determine thermal tissue property values using temperature simulations was introduced and the effect of using these values in temperature simulations is evalu-

ated in H&N hyperthermia patients. Most of the optimized values were in the same range as the baseline and thermal stress values in literature; however the tumor perfusion and muscle thermal conductivity were considerably larger. The discrepancy in tumor perfusion can be caused by differences in tumor pathology and physiology: baseline literature values were from brain tumors[76] and tumor (and normal tissue) values under thermal stress were from abdominal tumors, i.e. cervix, prostate, rectum[95]. The deviation in muscle thermal conductivity may be caused by the high vascularization of muscles in the H&N area, which may result in a higher perfusion and, especially during thermal stress, also in higher thermal conduction compared to the abdomen. Another explanation is the temperature dependence of the muscle properties; causing a large spread in the obtained patient-specific optimized values and the increased temperature may have increased the median patient-group optimized value. However, in the presented study, we were aiming to improve accuracy of temperature simulations and not necessarily with physiological correct thermal tissue parameters.

A number of items have an impact on the performance of the technique. Firstly, 100% transfer of power from the antenna connectors into the patient is assumed, which is not valid since parameters like the waterbolus shape affect this applicator efficiency. This might also explain the high optimized thermal tissue property values in muscle and fat, because a lower efficiency results in a lower predicted applied SAR resulting in lower optimized thermal tissue property values. Secondly, temperature measurement points are assumed to be accurately reconstructed. However, manual tracking of the catheter on CT_{Tcat} (2.5±1.3mm) and errors from the registration (<1.5mm[34]) affect reconstruction accuracy. A third limitation is the number of measurement points included (313); we aimed for around 20 measurement points for the evaluation (training and testing) per patient since this led to a reasonable optimization time (on average 7.5h/patient). Time constraints also hamper the use of the entire time-temperature profile, but increase in computational power will allow optimizations using the temperature profiles of the entire treatment. Lastly, since we included only H&N patient data as input, the optimized thermal tissue property values only hold for PBHE simulations at these settings and for H&N patients. However, it is possible to use another model for simulations, i.e. extending the PBHE simulations with DIVA to increase simulation accuracy, or to apply it to another patient-group, since the presented technique is generic and provides the means to re-optimize thermal tissue properties when temperature measurements and simulations are available for the respective patient-group, leading to optimal temperature prediction accuracy.

With the presented technique, temperature simulation can become more accurate and it therefore has a strong potential in the field of hyperthermia, i.e. to improve pre-treatment optimization, pre-treatment decision making and real-time adaptive application of hyperthermia. Figure 4.1 shows that there is room for improvement in the SAR-based target coverage, which can hopefully be improved using temperature instead of SAR-based treatment control. In addition, the technique can be useful in other applications where temperature simulations are important and probe or 3D thermometry data is available, e.g. EM radiation exposure assessment or high intensity focused ultrasound (HIFU).

As an alternative to our technique, Waterman et al. and Roemer et al. described a technique[91,108] that allows to determine the effective perfusion, i.e. a combination of perfusion and thermal conductivity, from the measured temperature decay at power off, e.g. at the end of treatment. This technique has been applied to superficial hyperthermia only, however, the application to head and neck hyperthermia is subject of an ongoing study. This technique has been used by Raaymakers et al[87] to iteratively optimize the tissue perfusion for the temperature simulation of each single patient. Over seven patients, they found a patient-averaged temperature difference of -0.1±1.7ºC (average ± one standard deviation) and absolute difference of 1.3±1.1ºC. We found a patient-averaged temperature difference of 0.0±0.5ºC and absolute temperature difference of 1.0±0.7ºC over 17 patients if we use patient-specific thermal tissue property values. However, when using patient-group specific parameters the error increases, as verified with the leave-one-out experiment. This difference in ΔT, using either patient-specific or patient-group parameters, indicates that there is room for improvement in our temperature predictions. In future studies, thermal tissue properties could be optimized at the first treatment, and then be used to predict the temperature for the following treatments. This approach requires invasive thermometry probes for the first treatment only, instead of the complete treatment series. Thus, although the current technique outperforms existing techniques, further improvement of simulation accuracy is required to warrant introduction of temperature-based HTP for dosimetry in the clinic as replacement of invasive thermometry.

4.5   Conclusion

We presented a technique for patient-group specific optimization of thermal tissue properties. Application of this technique to invasive temperature measurement data of patients treated with H&N hyperthermia led to patient-group specific tissue property values that effectively improved temperature simulation accuracy. Current accuracy makes simulations a valuable tool as additive to invasive measurements; improvements in accuracy are required to rely on only temperature-based HTP in the clinic.

3D temperature dosimetry using probes and simulations

Abstract

Purpose: *Dosimetry during deep-local hyperthermia treatments in the head and neck currently relies on a limited number of invasively placed temperature sensors. The purpose of this study was to assess the feasibility of 3D dosimetry based on patient-specific temperature simulations and sensory feedback.*

Materials and methods: *This study included ten patients in which invasive thermometry was applied in at least two treatments. Based on the invasive thermometry, we optimized patient-group thermal conductivity and perfusion values for muscle, fat and tumor using a leave-one-out approach. Next, we compared the accuracy of the predicted temperature (ΔT) and the hyperthermia treatment quality ($\Delta T50$) of these patient-group properties to patient-specific properties, which were optimized using previous treatment measurements. As a robustness check, and to enable comparisons with previous studies, we optimized the parameters not only for an applicator efficiency factor of 40%, but also for 100% efficiency.*

Results: *The accuracy of predicted temperature (ΔT) improved significantly using patient-specific properties, i.e. $1.0^o C$ (inter-quartile range (IQR): $0.8^o C$) compared to $1.3^o C$ (IQR: $0.7^o C$) for patient-group averaged tissue properties for 100% applicator efficiency. A similar accuracy was found for optimizations using an applicator efficiency factor of 40%, indicating the robustness of the optimization method. Moreover, in eight patients with repeated measurements in the target region, $\Delta T50$ significantly improved, i.e. $\Delta T50$ reduced from $0.9^o C$ (IQR: $0.8^o C$) to $0.4^o C$ (IQR: $0.5^o C$) using an applicator efficiency factor of 40%.*

Conclusions: *This study shows that patient-specific temperature simulations combined with tissue property reconstruction from sensory data provides accurate minimally invasive 3D dosimetry during hyperthermia treatments: T50 in sessions without invasive measurements can be predicted with a median accuracy of $0.4^o C$.*

5.1   Introduction

Patients with a tumor in the head and neck (H&N) region are often treated with radiotherapy and/or chemotherapy. At our institute H&N patients can also be treated with radiotherapy combined with hyperthermia, i.e. elevating tissue temperature to $39-44$ºC. For this combined treatment, phase III clinical evidence shows a substantially improved clinical outcome without inducing additional toxicity[51,53,100]. For the hyperthermia treatments we used the HYPERcollar applicator system, which is specifically designed to treat tumors in the H&N region that are located deeper than 4cm from the skin[79]. The HYPER-collar is a ring-shaped phased array hyperthermia applicator consisting of 12 antennas uniformly divided over two rings of six antennas, which can be individually controlled and operate at a frequency of 434MHz[78].

Prior to the first treatment with this applicator, a hyperthermia treatment plan (HTP) is made for system settings optimization, for decision-making, and to apply our real-time adaptive hyperthermia strategy[89]. In our current HTP, electromagnetic (EM) simulations are used to predict the energy deposition, i.e. the specific absorption rate (SAR), in the patient. Clinical studies have shown that treatment outcome is related to thermal dose[38,94], which advocates the use of temperature predictions instead of SAR predictions. In a previous study[107] a technique was presented that optimizes temperature simulation parameter values by fitting the simulated temperatures to the measured temperatures during treatment. The technique used only temperatures at steady state, while for evaluation of the complete treatment a transient temperature simulation is required.

The great strength of temperature simulations over the sparse data from the currently applied invasive thermometry is the possibility of generating temperature maps for the entire 3D volume. Further, temperature simulations provide an economic alternative for 3D magnetic resonance temperature imaging (MRTI)[45], which has not been demonstrated in the head and neck and which might prove challenging due to motion and susceptibility artefacts[81].

The purpose of this study was to assess the feasibility of 3D dosimetry based on patient-specific temperature simulations and sensory feedback. In addition, we established the accuracy of replacing invasive temperature measurements in each hyperthermia session by temperature predictions combined with invasive temperature data of the first session. First, we optimized the thermal conductivity and perfusion patientgroup parameter values for muscle, fat and tumor, and assessed the accuracy of the transient temperature simulation in a leave-one-out approach. Next, we compared the accuracy of the predicted temperature (ΔT) and the hyperthermia treatment quality (ΔT50) of the optimizations based on the patient-group parameter values to those based on patient-specific parameter values. The parameters were optimized using an applicator efficiency factor of 40% and 100%. The accuracy of the optimization with an applicator efficiency factor of 100% was used only for comparison with previous studies and as a robustness check of the optimization technique.

5.2   Methods

In our view there are two approaches to validate the 3D simulated temperature using sensory measurements. The first approach is to validate within one treatment by applying a leave-one-out experiment on the measurements points in the 3D volume. In such an experiment, the simulated 3D temperature can be optimized on a number of measurement probes and tested on a measurement probe that is not used in the optimization. In theory, for the best accuracy this approach requires at least two measurement points per tissue, i.e. six or more for fat, muscle and tumor, to provide validation of the 3D temperature distribution for one treatment only. In an alternative approach we optimized the patient-specific 3D temperature using all probes of the first treatment to predict the temperature for subsequent treatments. This approach not only provides an estimate of the 3D temperature prediction accuracy, including repeatability uncertainty, but also allows for improving patient comfort since at subsequent treatments it provides the accuracy of replacing invasive probes by predictions.

5.2.1   Treatment procedure

Patients were treated once or twice a week with deep, local H&N hyperthermia depending on the radiotherapy radiation schedule. Before the hyperthermia treatment, closed-tip thermometry catheters were placed interstitially, intraluminally and/or at the skin. The interstitial catheters were assumed to be located in tumor, muscle or fat tissue. They were placed under computed tomography (CT) guidance or under anaesthesia in an operating room. In the hyperthermia treatment room the patient was positioned in the same orientation with respect to the applicator as in the HTP. After patient positioning, fibre-optic temperature sensors (FISO, Quebec, Canada) were inserted into the closed-tip catheters. The hyperthermia treatment was started by applying 200W of total input power with antenna phase and power settings from the HTP. Power was increased in steps of 30W, till one of the tolerance limits was reached[79] or when the patient indicated a hot-spot at a site without thermometry. During the treatment, two phases were defined: 1) power-up phase, and 2) plateau-phase, and the transition was assumed to be always after 15min of heating.

5.2.2   Patient data

Over the past 7 years, 45 patients have been treated with deep local H&N hyperthermia in our institution. From these patients we selected the patients that had invasive temperature monitoring for at least two treatments. In total 10 patients (35 treatments) were included in the study with tumors in the oropharynx, nasopharynx, parotid gland and thyroid gland (Table 5.1).

Table 5.1: Patient and treatment characteristics, i.e. tumor location, number of treat-
ments and number of probes per tissue as used in the evaluation, thus ex-
cluding the first treatment since this data was already used for parameter
optimization. Note that for all treatments invasive probe measurements
were available.

patient no.	tumor location	no. of treatments	total no. of probes		
			tumor	muscle	fat
1	Oropharynx	2	4	7	0
2	Nasopharynx	2	4	4	0
3	Parotid gland	3	0	9	3
4	Oropharynx	6	8	29	4
5	Oropharynx	1	0	1	1
6	Oropharynx	4	4	17	1
7	Thyroid gland	3	0	7	6
8	Oropharynx	1	1	4	2
9	Thyroid gland	1	0	2	1
10	Thyroid gland	2	0	2	4

5.2.3 EM-based hyperthermia treatment planning (HTP)

Approximately 1 week before treatment a CT scan was acquired for EM-based HTP
purposes. This CT was converted into a 3D patient model by automatically segmenting
normal and critical tissues using a multi-atlas-based approach[34]. Then the tumor and the
target were manually segmented by an H&N radiation oncologist, as in Verhaart et al.[106].
EM tissue property values were assigned as indicated in Table 5.2. The EM-based HTP
procedure was applied using simulation settings as in Rijnen et al.[89].

The locations of the closed-tip catheters were reconstructed using a second CT scan.
The measurement points were distributed over muscle (65%), fat (18%) and tumor (17%)
tissue, of which 28% are located superficially (probe depth < 1cm), 62% intermediately
(1cm ≤ probe depth ≤ 4cm) and 10% deep (probe depth > 4cm), relative to the skin
surface. An example of the reconstructed probe location can be seen in Figure 5.1a, further
examples can be found in the report of Paulides et al.[79] and a detailed description of the
reconstruction can be found in the report of Verhaart et al.[107].

5.2.4 Temperature simulations

SEMCAD X (version 14.8.5, Schmid & Partner Engineering, Zurich, Switzerland) was used
to predict the 3D temperature distribution according to the Pennes bioheat equation[82]:

$$\rho c \frac{\partial T}{\partial t} = \nabla \cdot (k \nabla T) + \rho Q + \rho S - \rho_b c_b \rho \omega (T - T_b) \qquad (5.1)$$

where T [ºC] is the temperature, t [s] is the time, ρ [kg m^{-3}] is the volume density of mass,
c [J kg^{-1} ºC^{-1}] is the specific heat capacity, k [W m^{-1} ºC^{-1}] is the thermal conductivity,
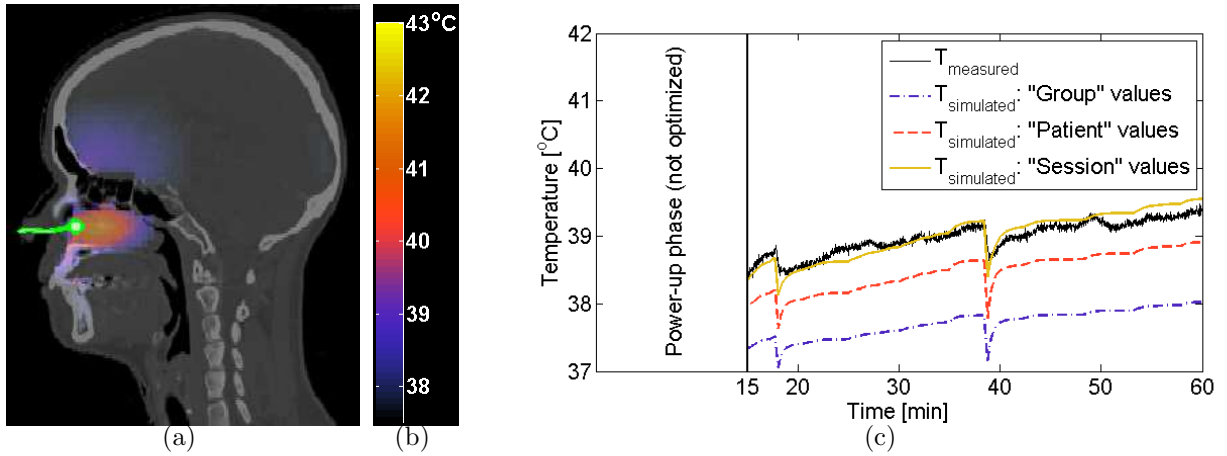
Figure 5.1: Predicted 3D temperature distribution on the planning CT shown together with the catheter track (solid green line) with a measurement probe at the tip inside the challenging-to-heat nasopharynx tumor (a). The temperature colormap is also included (b). As illustration, we show the temperature during treatment (c) for the temperature measured at the tip (solid black) compared with the predicted temperatures using Group (dash-dot purple), Patient (dashed red) and Session (solid orange) parameter values, when six parameters were optimized using an applicator efficiency factor of 100%. Results for an applicator efficiency factor of 40% were similar and therefore not shown.

ω [mL min^{-1} kg^{-1}] is the volumetric blood perfusion rate, Q [W kg^{-1}] is the metabolic heat generation rate, S [W kg^{-1}] is the SAR and the subscript $_b$ denotes a blood property. To account for temperature losses, we applied a mix of convective and Neumann (fixed flux) boundary conditions:

$$k\frac{dT}{dn} + h(T - T_{outside}) = F \qquad (5.2)$$

where n is the direction normal to the surface [m], $T_{outside}$ is the temperature outside the boundary [ºC], h is the heat transfer coefficient due to convective and radiative losses [W m^{-2} ºC^{-1}] and F is the fixed heat flux due to perspiration [W m^{-2}]. The boundary conditions were applied at the following interfaces: tissue − surrounding air ($h_{surroundingair}$ = 8W m^{-2} ºC^{-1}, [7]), tissue − waterbolus (h_{WB} = 82W m^{-2} ºC^{-1}, [102]), tissue − internal air, tissue − lung and tissue − metal implants ($h_{internalair/metal}$ = 50W m^{-2} ºC^{-1}, [7]). The initial temperature in the tissues was set to 37ºC while the temperature of the surrounding air and the waterbolus was set to 20ºC, as measured during hyperthermia treatments.

To apply actual treatment power steering in the temperature simulation, user-defined sources were created when the applied treatment power and/or phase changed more than ±5W or 5ºC respectively. For the user-defined source, the treatment phase and amplitude settings were applied to each antenna and the combined EM field was used to compute

Table 5.2: Literature values of EM and thermal tissue properties for T simulations at 37°C, baseline[47,55,56,59,76,78]. See Table 5.3 for 'thermal stress'(T-stress) and 'steady state optimized' (SS$_{\text{opt}}$) values.

Tissue	ϵ_{r}	σ_{eff}	ρ	c	k	Q	ω
internal air	1.0	0.0	1.2	-	-	-	-
lung	23.6	0.38	394	-	-	-	-
muscle	56.9	0.81	1090	3421	0.49	0.96	39.1
fat	11.6	0.08	911	2348	0.21	0.51	32.7
bone	13.1	0.09	1908	1313	0.32	0.15	10.0
cerebrum	56.8	0.75	1045	3696	0.55	15.5	763.3
cerebellum	55.1	1.05	1045	3653	0.51	15.7	770.0
brainstem	41.7	0.45	1046	3630	0.51	11.4	558.6
myelum	35.0	0.46	1075	3630	0.51	2.48	160.3
sclera	57.4	1.01	1032	4200	0.58	5.89	380.0
lens	37.3	0.38	1076	3133	0.43	-	-
vitreous humor	69.0	1.53	1005	4047	0.59	-	-
optical nerve	35.0	0.46	1075	3613	0.49	2.48	160.3
cartilage	45.1	0.60	1100	3568	0.49	0.54	35.0
thyroid gland	61.3	0.89	1050	3609	0.52	87.1	5624.3
tumor	59.0	0.89	1050	3950	0.51	-	400.0

ϵ_{r}: relative permittivity [-], σ_{eff}: effective conductivity [S m^{-1}], ρ: density [kg m^{-3}], c: specific heat capacity [J kg^{-1} °C^{-1}], k: thermal conductivity [W m^{-1} °C^{-1}], Q: metabolic heat generation rate [W kg^{-1}], ω: perfusion rate [ml min^{-1} kg^{-1}], GTV: gross tumor volume, Blood heat capacity ($\rho_{\text{b}}c_{\text{b}}$) = $4.1 \cdot 10^6$ [J m^{-3} °C^{-1}].

the SAR. The scaling factor of the source was the applicator efficiency factor (η). Thus, η determines the fraction of the power from the antenna connectors that is transferred into the patient.

5.2.5 Optimization procedure of thermal tissue parameter values

To optimize thermal tissue parameter values we started with the initial temperature simulation parameter values that solved the Pennes bioheat equation. The resulting simulated temperatures (T$_{\text{simulated}}$) were compared with the measured temperatures (T$_{\text{measured}}$). At each iteration of the optimization procedure the parameter values were modified in order to minimise the difference (ΔT) between T$_{\text{measured}}$ and T$_{\text{simulated}}$. Figure 5.2 shows a block scheme of this procedure.
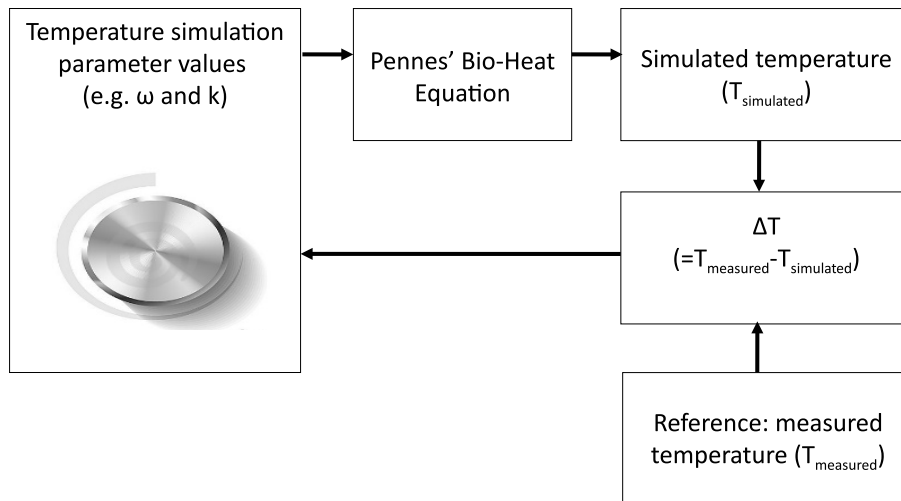
Figure 5.2: Block scheme of the optimization procedure

Optimizations based on transient temperature simulations were run using two different applicator efficiencies:

- $\text{Tr}_{\text{opt}}\ \eta : 40\%$

- $\text{Tr}_{\text{opt}}\ \eta : 100\%$

In both optimizations six thermal tissue parameters were optimized, i.e. ω_{tumor}, ω_{muscle}, ω_{fat}, k_{tumor}, k_{muscle} and k_{fat}. In the first optimization an applicator efficiency of 40% was used, which was obtained for the HYPERcollar applicator by Adibzadeh et al.[4] using the power-off method[91,108]. Since the patients included in our study were all treated with the HYPERcollar applicator we used the result of this optimization to determine the feasibility of 3D dosimetry. In the second optimization a perfect applicator efficiency of 100% was assumed. The result of this optimization was used only for comparison with previous studies and as a robustness check of the optimization technique.

The temperature simulation parameter values were optimized by minimising the cumulative differences between measured and simulated temperature points over all probes and the complete treatment time, excluding the first 15min of the power−up phase. A constrained non−linear optimization function[66] '*fminsearchbnd*' in MATLAB (version R2013a, MathWorks, Natick, MA, USA) was used with a maximum number of iterations 300, relative tolerance 0.1 and constraints $\omega \in (1, \infty)$ mL min^{-1} kg^{-1}, $\text{k} \in (0.01, \infty)$ W m^{-1} °C^{-1}. The initial values for ω and k were chosen as in Verhaart et al.[107] (Table 5.3: baseline values). Each simulation took on average 48±28min for $\text{Tr}_{\text{opt}}\ \eta : 100\%$ and 28±15min for $\text{Tr}_{\text{opt}}\ \eta : 40\%$ at a standard desktop computer with i7 3930K processor for a simulation consisting of 15MCells using a double precision solver.

5.2.6   Evaluation of optimized thermal tissue parameter values

Patient−group values   To quantify the predicted temperature accuracy using transient temperature simulations we validated the patient−group optimized temperature simulation parameter values (Group) in a leave-one-out experiment. In this experiment the data of a single patient was used as the test data, and the data of the remaining patients as the training data to optimize the parameter values. During the test the median value of the optimized parameter values of the training set was applied to the test set. This procedure was repeated such that each single patient data was used once as the test data. The advantage of this experiment was that all patients in our limited patient group could be used for training and testing, while we avoided over-tuning of the parameter values with respect to our group of patients, such that the validation held for new patients.

Patient−specific values   Patient-specific optimized thermal tissue property values (Patient) were obtained by applying the optimization procedure to the first treatment. These patient−specific optimized values were applied to the next treatments (Table 5.1) to investigate the accuracy of temperature simulation.

Session−specific values   The session−specific optimized values (Session) were obtained by applying the optimization procedure to a treatment and using the resulting optimized thermal tissue parameter values to the same treatment. These session−specific optimized values result in the best accuracy you could obtain with the optimization procedure, i.e. it describes how well the (optimized) model fits the data.

Overview of analysis   First, the accuracy of the patient-group optimized parameter values of $\mathrm{Tr_{opt}}\ \eta : 100\%$ and $\mathrm{Tr_{opt}}\ \eta : 40\%$ were compared with the accuracy of using literature parameter values, i.e. from steady-state temperature simulations using six parameters $(\mathrm{SS_{opt}})$, baseline values at 37ºC (Baseline) and values scaled due to the thermal stress (T-stress). Second, the accuracy of temperature simulation was compared between Patient, Group and Session parameter values. Third, the accuracy between $\mathrm{Tr_{opt}}\ \eta : 100\%$ and $\mathrm{Tr_{opt}}\ \eta : 40\%$ was compared to check the robustness of the optimization technique. Since the patients included in our study were all treated with the HYPERcollar applicator, we used the result of $\mathrm{Tr_{opt}}\ \eta : 40\%$ to determine the feasibility of 3D dosimetry.

The accuracy of temperature simulation was reported by the median and the interquartile range (IQR) of the absolute temperature difference $(\Delta\mathrm{T})$ between measured and simulated temperature points over all treatments, all probes and the complete treatment duration, excluding the first 15min of the power-up phase. IQR is the difference between the 75th and the 25th percentiles of the samples in $\Delta\mathrm{T}$, as indicated by the edges of the box-plots in Figures 5.3 and 5.4. The feasibility of 3D dosimetry is quantified by $\Delta\mathrm{T}50$, defined as the difference between the measured and simulated T50 in the target. T50 is a frequently used hyperthermia treatment quality parameter and is defined as the temperature exceeded by 50% of the monitored probes in the whole target and averaged over

Table 5.3: Patient-group optimized values of transient temperature simulations using an applicator efficiency factor of $\eta : 100\%$ and $\eta : 40\%$. For comparison, we also show literature values for these thermal tissue properties for T simulations at 37ºC: Baseline[47,55,56,59,76,78], thermal stress (T-stress)[95] and steady-state optimized (SS_{opt}) values[107].

	$\eta : 100\%$	$\eta : 40\%$	Baseline	T-stress	SS_{opt}
ω_{tumor}	2933.1	848.0	400.0	80.0	1146.0
ω_{muscle}	785.6	442.8	39.1	300.0	563.6
ω_{fat}	524.4	255.0	32.7	200.0	76.7
k_{tumor}	3.3	1.5	0.51	0.64	0.97
k_{muscle}	4.1	0.4	0.49	0.64	5.75
k_{fat}	2.3	0.5	0.21	0.21	0.38

ω: perfusion rate [ml min^{-1} kg^{-1}], k: thermal conductivity [W m^{-1} ºC^{-1}], η : applicator efficiency factor.

all treatments per patient[38]. Note that ΔT and $\Delta T50$ are in fact measures of inaccuracy; however, for readability reasons we used the term accuracy. We tested for statistical significance ($p < 0.05$) using the non-parametric Wilcoxon signedrank test[109].

5.3   Results

Table 5.3 shows the patient-group optimized values for transient temperature simulations using an applicator efficiency factor of $\eta : 100\%$ and $\eta : 40\%$. The values of $\eta : 40\%$ agree most with the literature values.

      Figure 5.3 shows three results. First, it compares the accuracy of the predicted temperature using Group parameter values optimized using either steady-state temperature simulations (SS_{opt}) or transient temperature simulations (Tr_{opt} $\eta : 100\%$ and Tr_{opt} $\eta : 40\%$). The accuracy improved when replacing steady-state by transient optimized parameters, i.e. ΔT reduces from 1.6ºC (IQR 1.2ºC) for SS_{opt} to 1.3ºC (IQR 0.7ºC) for Tr_{opt} $\eta : 100\%$ and 1.4ºC (IQR 0.9ºC) Tr_{opt} $\eta : 40\%$. Overall, our optimized parameter values strongly improved the accuracy compared to the accuracy based on literature values: 10.9ºC (IQR 11.5ºC) for baseline values and 2.9ºC (IQR 3.4ºC) for T-stress values (not shown). Second, Figure 5.3 provides the accuracy of the optimization procedure using either Group, Patient or Session parameter values for transient temperature simulations using an applicator efficiency factor of $\eta : 100\%$ and $\eta : 40\%$. A significant improvement in accuracy was found when using patient−specific parameter values of the first treatment for temperature predictions in following treatments for Tr_{opt} $\eta : 100\%$, i.e. ΔT significantly reduced from 1.3ºC (IQR 0.7ºC) to 1.0ºC (IQR 0.8ºC). Although not significant, Tr_{opt} $\eta : 40\%$ shows a similar improvement, i.e ΔT reduced from 1.4ºC (IQR 0.9ºC) to 1.1ºC (IQR 1.4ºC). Third, Figure 5.3 compares Tr_{opt} $\eta : 100\%$ with Tr_{opt} $\eta : 40\%$. In general, the optimized parameter values resulted in similar accuracies, indicating the robustness of the optimization method.
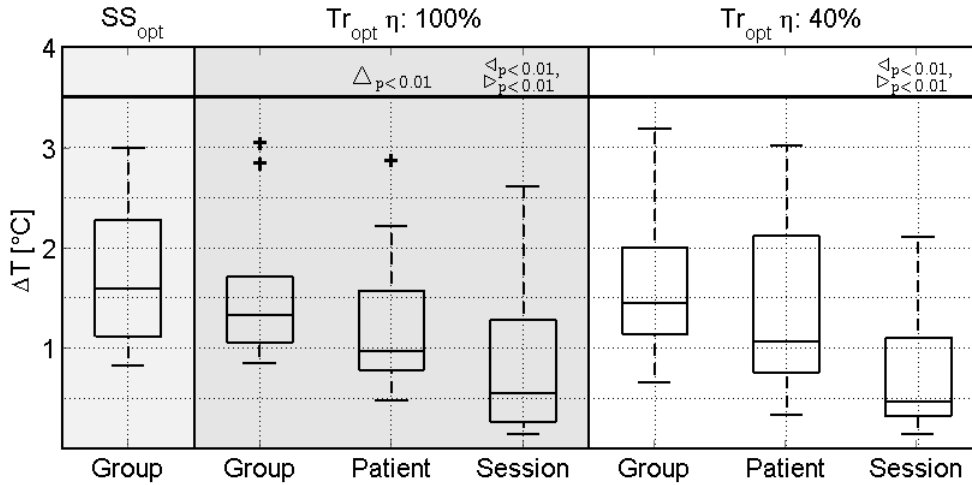
Figure 5.3: Comparison of the transient temperature simulation accuracy (ΔT) when applying Group, Patient or Session parameter values from transient simulations using an applicator efficiency factor of 100% (Tr_{opt} η : 100%) or 40% (Tr_{opt} η : 40%). As a cross-check, the Group parameter values from steady-state simulations (SS_{opt}) are given. Statistically significant differences are indicated for Group versus Patient ($\triangle$), Group versus Session ($\triangleleft$) and Patient versus Session ($\triangleright$). In the box-plots, the central mark is the median, the edges are the 25th and 75th percentiles, the whiskers extend to the most extreme data points not considered outliers (99.3%), and outliers are plotted individually ($+$).

Figure 5.1a illustrates the improvement in simulation accuracy when using patient-specific parameter values of the first treatment for temperature predictions in following treatments, since it clearly shows that the Patient values predicted the measured temperature better than the Group parameter values. Note that the Session parameter values resulted in an almost complete match with the measured temperatures.

Figure 5.4 further stresses the improvement in 3D temperature simulation with the frequently used hyperthermia treatment quality parameter T50 in the target, for the eight patients that had invasive measurements available inside the target. It shows a significantly reduced median difference between measured and predicted T50 in the target when comparing the application of Group versus Patient parameters, i.e. ΔT50 significantly reduced from 0.9ºC (IQR 0.8ºC) to 0.4º (IQR 0.5ºC).
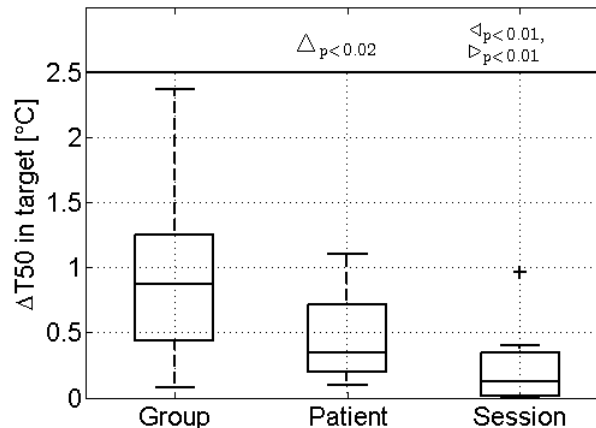
Figure 5.4: The feasibility of 3D dosimetry quantified by the difference in measured and simulated T50 in the target (ΔT50) using transient temperature simulations with an applicator efficiency of 40% when applying Group, Patient or Session parameter values. Note that the T50 could only be computed for eight patients since they received invasive measurements inside the target. Statistically significant differences are indicated for Group versus Patient ($\triangle$), Group versus Session ($\triangleleft$) and Patient versus Session ($\triangleright$). In the box-plots, the central mark is the median, the edges are the 25th and 75th percentiles, the whiskers extend to the most extreme data points not considered outliers (99.3%), and outliers are plotted individually (+).

5.4   Discussion

5.4.1   3D temperature simulation accuracy

In this study we assessed the feasibility of 3D dosimetry based on patient-specific temperature simulations and sensory feedback. The temperature simulations using patient-specific tissue properties in combination with patient-specific 3D models significantly improved temperature prediction accuracy compared to patient-group averaged properties. In a set of eight patients, the 3D median tumor temperature (T50) can be predicted with a median accuracy of 0.4ºC (IQR 0.5ºC) using these patient−specific properties. This makes our patient-specific temperature simulations a promising tool for minimally invasive 3D dosimetry during hyperthermia treatments.

Other approaches that investigated accuracy of 3D temperature dosimetry were based on the power-off method[91,108] or MRTI. The power-off technique allows SAR or the effective perfusion to be determined, i.e. a combination of perfusion and thermal conduction from the measured temperature decay at power-off, e.g. at the end of the treatment. Raaymakers et al.[87] used this technique to iteratively optimize the tissue perfusion parameter value for the temperature simulation of each single patient. For seven patients they found

a patient average absolute temperature difference of 1.3±1.1°C (68% of data values). We should compare this with our accuracy of the Session values: median: 0.5°C (IQR 1.0°C) for Tr_{opt} $\eta : 100\%$, and median: 0.5°C (IQR 0.8°C) for Tr_{opt} $\eta : 40\%$ (50% of data values). There are several possible explanations for this difference between both studies: the difference in the region of interest: prostate versus head and neck, difference in the less accurate probe reconstruction due to a courser imaging (ultrasound 5mm versus CT 0.3x0.3x0.5mm − 1x1x3mm) and a less accurate temperature simulation due to a less detailed patient-model (MRI versus CT+MRI).

MRTI is a non-invasive temperature imaging technique, which provides an accuracy in the extremities or in the pelvic lower than 1°C[21,44]. However, accuracy has not been demonstrated for the H&N and MRTI in this region is expected to be challenging due to motion and susceptibility artefacts[81]. Hence, our transient temperature simulation optimization technique combined with limited invasive thermometry currently provides the best option for 3D temperature dosimetry during head and neck hyperthermia.

A number of limitations may have affected our results. Firstly, to reduce simulation time, metal implants were not modelled as volumes with metal properties, but instead as inactive while mimicking their impact by a mixed boundary condition. An additional investigation in one patient model showed that this only affected the predicted temperatures <0.5cm from metal, and hence only a small impact on overall simulation accuracy can be expected. Secondly, the reconstruction of the temperature sensor locations was assumed to be 100% accurate. However, earlier we showed that manual tracking and registration errors affect reconstruction accuracy[107], and thus possibly also the optimized parameter values and reported accuracy. Thirdly, most measurement sensors were available in oropharynx patients, where reconstruction and measurement accuracy is the poorest[79]. Since this region is a worst-case estimate, measurements in other regions should be better. Fourthly, temperature dependency of perfusion is to be expected, but not incorporated in our study. Therefore our optimized values are expected to be less accurate for higher temperatures. Lastly, our results and conclusions are based on H&N hyperthermia treatment data only, but the optimization of temperature simulations using sensory data is a generic method that can be applied to other sites as well.

5.4.2   Optimized tissue property values

The six optimized parameter values (ω and k for tumor, muscle and fat tissue) using an applicator efficiency factor of 100% (Tr_{opt} $\eta : 100\%$) were all much larger, i.e. one or two orders of magnitude, than previously reported in literature[47,55,59,76,95]. However, they are in agreement with the values previously found with the steady-state simulation-based technique[107]. The values of these parameters became lower and closer to physiological values when an applicator efficiency factor of 40% (Tr_{opt} $\eta : 40\%$) was used (Table 5.3). In this optimization the largest deviations in tissue properties were found in tumor tissue. This discrepancy in tumor tissue properties could be caused by differences in tumor pathology and physiology. Baseline literature values were from brain tumors[76] and thermal stress values were from pelvic tumors, i.e. cervix, prostate, rectum[95]. Nevertheless, note that in

the present study we aimed to assess the feasibility of 3D dosimetry using patient-specific temperature simulation and not necessarily with physiological thermal tissue parameter values.

Despite the variation in optimized tissue property values using an applicator efficiency factor of 40% or 100%, a similar T50 accuracy was found. As treatment decisions are based on T50, these decisions will not be dependent of the applicator efficiency used. However, note that a re-optimization of the tissue property values is needed when a different applicator efficiency factor than 40% or 100% is used.

In one of our optimizations we used an applicator efficiency factor of 40%. Applicator quality assurance measurements showed that 30% can be explained by mismatches and heat generation in the antenna and connector. Hence, a large proportion of SAR modeling uncertainty is caused by an incorrectly modelled water-bolus shape. In our new applicator the HYPERcollar3D[99], we therefore implemented a much more reproducible and conformable waterbolus shape in order to substantially improve the accuracy of simulations. Such a reproducible set-up should further improve the applicability of the method presented here, and hence the clinical potential of this procedure.

5.5   Conclusion

In this study we assessed the feasibility of 3D dosimetry based on patient-specific temperature simulations and sensory feedback. The hyperthermia T50 treatment quality parameter in the target can be predicted with a median accuracy of 0.4°C (IQR 0.5°C) using patient-specific properties. Our analysis clearly shows the potential of patient-specific temperature simulations combined with sensory data as a promising tool for minimally invasive 3D dosimetry during hyperthermia treatments.

CHAPTER 6

General discussion and future perspectives

6.1   3D patient model generation

6.1.1   Evaluation of the approach

In our approach we used advanced image processing tools for tissue segmentation. To these segmented tissue regions, literature based tissue property values are applied as input for EM and temperature simulations. We exploited our experience with image processing tools to make the HTP proces similar to the radiotherapy treatment planning proces, making it more straight foreward to implement in the clinical routine. Our approach differed from other studies as they do not discriminate tissues based on the contrast in the image, but on the dielectric tissue property that is measured in a certain region. This is for example possible with a MRI scanner using a technique called electrical property tomography (MRI-EPT). An advantage of MRI-EPT is that it uses patient-specific dielectric properties [9,10] instead of general, literature based tissue property values. Several studies [43,110] have shown that surface models, i.e. tissue segmentation, each with assigned homogenous dielectric properties, shows benefits compared to models that attempt to derive heterogeneous dielectric properties directly from CT data. Similar results were obtained from attempts that use MRI-derived heterogeneous tissue models [33,71]. Of course, when research continues, it has a potential to become an adequate technique to obtain patient specific dielectric tissue property values. However, at this moment, MRI-derived heterogeneous tissue models (e.g. using MRI-EPT) has some more drawbacks. First, a clinical validation is missing. Second, an analysis on the effect of the required extra MRI scans and extra scan time on the clinical routine is missing. Last, definition of optimization regions, e.g. organs as risk, remains required for HTP, hence tissue segmentation remains needed. Therefore, surface models are the current standard for HTP.

6.1.2   Future work and perspectives

In my work a 3D patient model was created by stacking segmented tissues that are segmented from routinely acquired scans. At the start of my project, this model was created by manually segmenting numerous organs from CT and occasionally additionally also from MRI. Manually segmenting these organs for each patient requires many man-hours, which hinders clinical acceptance. For this reason, an automatic segmentation tool was developed and clinically validated that increased segmentation speed and reduced operator times, i.e. a 3D patient model can be generated within one hour. At this moment our automatic segmentation tool is successfully used in hyperthermia treatment planning for treatments with the HYPERcollar and HYPERcollar3D applicator.

A possible application of the segmentation tool in the future is to combine it with techniques that measure dielectric tissue properties, e.g. MRI-derived heterogeneous tissue models using MRI-EPT. Although the use of heterogeneous tissue models have been shown to have drawbacks as discussed before, it remains an adequate technique to obtain patient specific dielectric tissue property values [9,10]. One could use measured patient specific tissue-averaged property values and apply these to the tissues segmented using our automatic

segmentation tool. Of course, the exact influence and impact of this approach on additional scanning time, patient discomfort and HTP accuracy remains to be determined.

In theory, H&N hyperthermia is not the only application for our automatic segmentation tool. In the future, it might for example also be used for superficial or deep hyperthermia or in radiotherapy treatment planning. Further, it can also be used in studies that assess the exposure by electromagnetic sources of the human body, since those studies also use 3D human models. Since the tool is based on a multiatlas approach combined with intensity modeling, a requirement for the use of our tool is a library of accurately segmented patient models that incorporate all the relevant tissue-shape variations. When other tissues than the current tissues are added to the library, an optimization of the intensity model parameters is needed for these tissues to obtain accurate patient models, i.e. 1% variation in HTP quality for our tool (chapter 2). Ideally, also a clinical validation should be done as described for the current tool in chapter 2.

6.2 Temperature modeling

6.2.1 Evaluation of the approach

After development and clinical validation of the CT and MRI based segmentation tool to create patient models, the tools were ready to improve temperature modeling by optimizing thermal tissue property values using the temperature sensor data and simulations.

In our approach, we focussed on improving temperature simulations instead of EM simulations as in our view temperature is a better measure for treatment outcome since clinical studies[38,94] have shown that treatment outcome is related to thermal-dose. An approach to obtain temperature information is to use invasive thermometry. A drawback of invasive thermometry is that usually only sparse measurement points are available. The great strength of temperature simulations over the sparse data from invasive thermometry is the possibility of generating temperature maps for the entire 3D volume. Another way of generating 3D temperature maps is by using magnetic resonance temperature imaging (MRTI)[45]. MRTI is a non-invasive imaging technique to measure temperature. It has shown to provide a good accuracy in the extremities and in the pelvic[21,44]. However, accuracy has not been demonstrated in the H&N and MRTI in this region might prove challenging due to motion and susceptibility artefacts[75,81]. Hence, currently the best option for 3D temperature dosimetry during H&N hyperthermia is our temperature simulation optimisation technique combined with limited invasive thermometry.

6.2.2 Future work and perspectives

Various simulation models to predict temperature have been developed[80]. In hyperthermia, temperature modeling is commonly based on the Pennes Bioheat equation (PBHE)[82]. The PBHE models perfusion by a heat sink, but the direction of blood flow and the heat exchange between large vessels and tissues are not included. The discrete vascular

(DIVA) model is a more physiologically correct model as it includes vessel networks[61]. Unfortunately, the integration of representative vessel networks in the simulation is a lengthy and tedious procedure, which prevents application of this approach in clinical practice upto now. In the future, vessel segmentation methods could be developed and integrated into our segmentation tool. It is important that specific CT and/or MRI protocols are used to be able to improve vessel contrast on these images, which improves vessel (auto)segmentation. With current imaging techniques it is possible to segment vessels with a diameter of upto 0.6mm[20], whereas heat exchange is thermally significant in vessels down to 0.2mm in diameter. Therefore, several attempts have been made to generate artificial vessels or to combine vessel tree data with perfusion maps[19,64,85,86,104]. Since the probes of my investigation were always distant from large vessels, the improvement on temperature prediction by DIVA could be studied by comparing temperature predictions based on our current patient-specific models with and without blood vessels. These approaches have upto now never been applied to the challenging and well perfused H&N region. Thus, future research should focus on adding DIVA to the PBHE model to incorporate influences of large vessels.

Since measurement-guided (MRTI) and simulation-guided (temperature simulations) temperature dosimetry supply complementary information it might be wise to make use of each others advantages. An advantage of MRTI is that it supplies many measurement points, while our technique uses only sparse thermometry points. A second advantage of MRTI is that MRTI is non-invasive, while our temperature simulation optimisation technique uses invasive thermometry measurement points. An advantage of simulation-guided temperature dosimetry is that it is more comfortable for the patient because family and friends can be close to the patient during treatment, while in a MRI room the patient is alone. Also the hyperthermia staff appreciates direct contact with the patient for example to have better control over the patient, which is easier in simulation-guided temperature dosimetry as with MRTI. A second advantage of simulation-guided temperature dosimetry is that claustrophobic patients have no problem with this technique, while those patients generally have problems going into the bore of the MRI scanner. A third advantage of simulation-guided temperature dosimetry is that it is easier to apply a combined hyperthermia and radiotherapy treatment, which is a challenge when this combined treatment is given in the MRI scanner. Nevertheless, studies are ongoing that investigate the integration of a linear accelerator inside a MRI scanner[22] which gives us in the future the possibility to apply radiotherapy in a MRI scanner. A fourth advantage of simulation-guided temperature dosimetry is its cost-efficiency. A prerequisite for MRTI is a MRI scanner, which is commercially available and allows simultaneous treating and measuring. An MRI scanner, and especially a hybrid MRI, is still rather expensive to purchase, making MRTI a capital intensive technique. Therefore, temperature simulations provide an economic alternative for MRTI. In the future, a combination of both techniques could be used to make use of each others advantages. Our technique can be used to optimise simulated temperatures based on measured temperatures from MRTI. When doing so for the first session of the hyperthermia treatment, the MRTI can be avoided for the next sessions of the patient, since our optimization technique could provide the 3D predicted

temperatures. In case of a claustrophobic patient that is unable to go into the MRI scanner, simulation-guided temperature dosimetry with invasive measurement points remains the only option. An additional and interesting reason to combine both techniques is to investigate how thermal tissue properties of the target might change during the series of a treatment session with radiotherapy and/or chemotherapy and/or hyperthermia. Eventually when all temperature related characteristics of tissues and especially tumor tissue is collected, future scenarios might be to better predict the 3D temperature-time profile for these tissues with no or minimal verification required.

In the future, temperature modeling will continue to mature and will be used to prospectively compare treatment options, optimise treatments and to enrich temperature measurement data. In the case that MRTI is a possibility for a treatment, a temperature model can be improved with fast optimisation feedback control algorithms to correct for the model errors and uncertainties. In the case that MRTI is not possible, temperature modeling will be critical to improve treatment quality since it is the only instrument available for treatment guidance. Since both temperature modeling and MRTI obtain overlapping and complementary information that is crucial for a successfull hyperthermia treatment, further innovation in temperature modeling should and will go hand in hand with developments in MRTI.

Summary

The prognosis for patients with advanced head and neck (H&N) cancer is very poor and treatment is challenging[18,70]. These patients are standardly treated with radiotherapy with or without chemotherapy. These treatments are associated with a high treatment related late toxicity that affects the quality of life and social contacts in 20% of the patients[113]. Side effects reported in all studies concern loss of swallowing and salivary function leading to difficulties in speaking and eating[18,68]. Clinical studies[23,51,53,100,113] have shown that the addition of a local hyperthermia treatment to a (chemo)radiation treatment signifcantly improve the treatment outcome without increasing treatment related late toxicity. Application of hyperthermia in the challenging H&N region using multi antenna-element applicators requires hyperthermia treatment planning (HTP). This thesis focuses on the development of an accurate and efficient patient model generation for patient-specific HTP based on electromagnetic (EM) and temperature modeling. The first two chapters include the automatic generation of 3D patient-models from Computed Tomography (CT) scans (chapter 2) or CT and Magnetic Resonance Imaging (MRI) scans (chapter 3). Chapter 4 and 5 include temperature simulation guided H&N hyperthermia using optimized thermal tissue property values.

3D patient model generation

Crucial input for accurate hyperthermia treatment planning is an accurate 3D patient model. This model is created by manually segmenting numerous organs from CT and/or MRI. Manual segmenting these organs for each patient requires many man-hours, which hinders clinical acceptance. For this reason, we developed an automatic segmentation tool.

In chapter 2, we validated the tool by comparing the manual- and automatic segmented tissues. We showed that despite geometrical variations, manual and automatic generated 3D patient models have a similar impact (1%) on variation in HTP quality. This impact was low with respect to the other sources of patient model uncertainties (11.7%). Furthermore, a considerable reduction in operator time per patient was achieved when using the automatic segmentation (± 1 hour) instead of the manual segmentation (5-6 hours). Thus, it was decided to introduce the recently developed automatic-segmentation algorithm in the clinic for pre-treatment and real-time treatment optimization. In the future, this tool can also be extended to other regions than H&N hyperthermia. Since the tool is based on a multiatlas approach combined with intensity modeling, a requirement for the use of our tool is a library of accurately segmented patient models that incorporate all the relevant tissue-shape variations. When other tissues than the current tissues are added to the library, an optimization of the intensity model parameters is needed for these tissues for accurate patient models. Ideally, also a validation of the new tool should be done as described for the current tool in this chapter.

In chapter 3, we investigated the relevance of using MRI in addition to CT for patient modeling in simulation guided hyperthermia. Hereto, we compared the impact of CT and CT & MRI based patient models on predicted temperatures, using tissue properties as optimized in chapter 4. We showed that although MRI reduced segmentation variation

in most tissues, it does not affect simulated local tissue temperatures in thermo-sensitive tissues. However, the improved soft-tissue contrast provided by MRI allows generating a detailed brain segmentation, which has a strong impact on the predicted local temperatures in the thermo-sensitive tissues. For that reason, a detailed brain segmentation based on MRI was also integrated in the automatic segmentation tool[36].

Temperature modeling

Currently, in our clinical practise HTP is based on EM simulations for predicting the energy deposition (i.e. SAR) in the patient, but clinical outcome is related to the thermal dose[38,94]. In clinical practice, temperature simulations are not used for H&N HTP due to the absence of a sound validation. This lack is caused by the sparse measurement points available for validation and the uncertainties in the thermal properties of tissue, which vary between patients, within the patient, within each tissue, over time, and is dependent on tissue temperature. To overcome this problem, we developed a technique based on a leave-one-out approach that allows good training and evaluation of the thermal tissue property values with a sparse dataset.

In chapter 4, the technique for patient-group optimization of thermal tissue properties based on invasively measured temperatures is presented and the achievable accuracy is evaluated. The thermal tissue property values for perfusion and thermal conductivity were optimized in fat, muscle and tumor tissue to match predicted and measured temperatures. In a dataset of H&N cancer patients treated with invasively measured temperatures, we applied a leave-one-out approach to assess the difference between measured and simulated steady-state temperature. Since the difference between measured and simulated 'steady-state' temperature (ΔT) for the patient-group optimized properties (ΔT: 2.1$\pm$1.2ºC) was lower than commonly used literature-based tissue property values[47,55,59,76,95] (ΔT: 12.7$\pm$11.1ºC) we were able to show that the optimization technique can be used to improve temperature simulation accuracy.

 In chapter 5, the thermal tissue property optimization technique as presented in chapter 4 was further improved. First, by using transient instead of steady-state temperature simulations to be able to evaluate the complete treatment. As a cross-check, we compared the accuracy of temperature simulations using either transient or steady-state optimized property values. Second, by optimizing patient-specific instead of patient-group tissue property values. We showed that the accuracy of steady-state and transient temperature simulations is similar. The temperature simulations accuracy of patient-specific tissue property values was improved compared to patient-group tissue property values. The study shows that patient-specific temperature simulations combined with tissue property reconstruction from sensory data provides accurate minimally invasive 3D dosimetry during hyperthermia treatments: T50 in sessions without invasive measurements can be predicted with a median accuracy of 0.4ºC. At this moment, when considering the available data and the current accuracy of other approaches[75,81,87], this is the best accuracy achievable for H&N hyperthermia treatments.

Samenvatting

Patiënten met gevorderde tumoren in het hoofd-hals (HH) gebied hebben een slechte prognose en een goede behandeling blijft lastig[18,70]. Meestal worden deze patiënten behandeld met radiotherapie soms in combinatie met chemotherapie. Deze behandelingen gaan vaak samen met aan de behandeling gerelateerde late toxiciteit die de kwaliteit van leven en sociale contacten van 20% van de patiënten aantast[113]. Veel gerapporteerde bijwerken van deze behandelingen zijn verlies van de slikfunctie en een aangetaste speekselproductie wat spraak- en eetproblemen geeft[18,68]. Klinische studies[23,51,53,100,113] hebben aangetoond dat de toevoeging van een hyperthermie behandeling de uitkomst van de behandeling significant verbeterd zonder extra bijwerkingen. De toepassing van hyperthermie in het lastige en uitdagende HH gebied met een systeem dat bestaat uit meerdere antenne elementen vereist hyperthermie behandel planning (HTP). Dit proefschrift beschrijft de ontwikkeling van nauwkeurige en efficiënte tools om een patiënt model te genereren voor patiënt specifieke HTP die gebaseerd is op elektromagnetische (EM) en temperatuur modellering. De eerste twee hoofdstukken gaan over het automatisch genereren van 3D patiënt modellen vanuit Computed Tomography (CT) scans (hoofdstuk 2) of vanuit CT en Magnetic Resonance Imaging (MRI) scans (hoofdstuk 3). Hoofdstuk 4 en 5 gaan over temperatuur simulatie gestuurde HH hyperthermie waarbij gebruik wordt gemaakt van geoptimaliseerde thermische weefsel eigenschappen.

3D patiënt modellen

Cruciale input voor nauwkeurige HTP is een representatief 3D patiënt model. Dit model wordt gemaakt door handmatig een aantal weefsels in te tekenen op CT en/of MRI. De handmatige intekening van weefsels voor iedere patiënt vereist veel tijd waardoor het niet zo snel geaccepteerd wordt in de kliniek. Om deze reden hebben we een tool ontwikkeld waarbij weefsels automatisch ingetekend kunnen worden.

In hoofdstuk 2 hebben we de tool gevalideerd door de automatische intekeningen te vergelijken met handmatige intekeningen. We hebben laten zien dat ondanks kleine geometrische variaties, handmatig en automatisch gegenereerde 3D patiënt modellen een vergelijkbare impact (1%) hebben op de variatie in HTP kwaliteit. Deze impact was klein als je het vergelijkt met andere mogelijke onzekerheden in het patiënt model (11.7%). Verder verkort de automatische segmentatie tool de benodigde tijd van de intekenaar, namelijk van 5-6 uur voor handmatige intekeningen naar ongeveer 1 uur voor de automatische intekening. Om deze redenen is besloten de automatische inteken tool te gaan gebruiken in de kliniek. In de toekomst kan de tool ook uitgebreid worden voor gebruik in andere locaties dan HH hyperthermie. Een vereiste is dan wel dat dan ook een bibliotheek van nauwkeurig ingetekende patiënt modellen aanwezig is waarin alle relevante variaties van de weefsels zitten. Als andere weefsels toegevoegd worden dan degene die nu al in de bibliotheek zitten, dan moet een heroptimalisatie van de parameters van de autosegmentatie methode plaatsvinden voor nauwkeurige patiënt modellen. Idealiter moet er ook weer een validatie gedaan worden zoals gedaan is voor de huidige tool en zoals beschreven in dit hoofdstuk.

In hoofdstuk 3 hebben we onderzocht wat de relevantie is van de toevoeging van MRI beelden bij patiënt modellering voor simulatie gestuurde hyperthermie. Om dit te onderzoeken hebben we de impact op de voorspelde temperatuur verdeling vergeleken voor CT gebaseerde patiënt modellen en patiënt modellen gebaseerd op CT & MRI. Voor de temperatuur simulaties hebben we gebruik gemaakt van de weefseleigenschappen zoals we die geoptimaliseerd hebben in hoofdstuk 4. We hebben laten zien dat ondanks het feit dat er op MRI minder inteken variatie is, dit geen effect heeft op de lokaal voorspelde weefsel temperaturen in temperatuur gevoelige weefsels. Echter, doordat je op MRI beelden goed zachte weefsels in kan tekenen was het mogelijk om ook de hersenen gedetailleerder in te tekenen. Uit de resultaten bleek dat als de gedetailleerde hersenintekening meegenomen werd in het model dat dit een groot effect had op de voorspelde lokale temperaturen in temperatuur gevoelige weefsels. Om die reden hebben we onze automatische inteken tool uitgebreid met de functionaliteit om op MRI beelden gedetailleerde hersenweefsels automatisch in te kunnen tekenen[36].

Temperatuur modelering

Op dit moment is HTP gebaseerd op EM simulaties waarbij de energie afgifte (ook wel SAR genoemd) in het weefsel wordt bepaald. Echter, klinische studies hebben aangetoond dat het klinische resultaat gerelateerd is aan de thermische dosis[38,94]. In de klinische praktijk worden temperatuur simulaties niet gebruikt voor HH HTP omdat een goede validatie mist. De reden dat temperatuur simulaties nooit gevalideerd zijn is omdat er maar een beperkt aantal meetpunten beschikbaar zijn. Verder zijn er ook veel onzekerheden in de thermische weefsel eigenschappen die variëren tussen patiënten, binnen een patiënt, binnen een weefsel, gedurende de tijd en ze zijn afhankelijk van de weefsel temperatuur. Om dit probleem te verhelpen hebben we een techniek ontwikkeld die gebaseerd is op een 'leave-one-out' aanpak waarbij het mogelijk is om een goede training en evaluatie van thermische weefsel eigenschappen uit te voeren op een beperkte dataset.

In hoofdstuk 4 wordt de techniek, waarbij invasief gemeten temperaturen worden gebruikt voor de optimalisatie van patiënt groep geoptimaliseerde thermische weefsel eigenschappen, gepresenteerd en de nauwkeurigheid geëvalueerd. De thermische weefsel eigenschappen voor perfusie en thermische geleiding werden geoptimaliseerd in vet, spier en tumor weefsel. We gebruikte een dataset van HH kanker patiënten die tijdens de behandeling invasief aangebrachte katheters hadden voor het meten van de temperatuur. Op deze dataset paste we de 'leave-one-out' methode toe om het verschil te bepalen tussen gemeten en gesimuleerde 'steady-state' temperatuur. Uit de resultaten bleek dat het verschil tussen gemeten temperatuur en gesimuleerde 'steady-state' temperatuur (ΔT) waarbij we onze patiënt groep geoptimaliseerde weefseleigenschappen gebruikte veel kleiner was (ΔT: 2.1±1.2ºC) dan bij het toepassen van de algemeen gebruikte literatuur gebaseerde weefseleigenschappen[47,55,59,76,95] (ΔT: 12.7±11.1ºC). Hiermee was dus aangetoond dat deze aanpak de nauwkeurigheid van temperatuur simulaties kan verbeteren.

In hoofdstuk 5 hebben we de techniek uit hoofdstuk 4 verder verbeterd. In eerste

instantie door in plaats van 'steady-state' simulaties nu tijdsafhankelijke temperatuur simulaties te optimaliseren. Dit maakt het namelijk mogelijk om de gehele behandeling te kunnen evalueren. Als een cross-check vergeleken we de nauwkeurigheid van temperatuur simulaties waarbij we 'steady-state' of tijdsafhankelijke geoptimaliseerde weefseleigenschappen gebruikte. Een tweede verbetering van de techniek is dat we in plaats van patiënt groep nu ook patiënt specifiek de weefseleigenschappen optimaliseerde. Uit de resultaten kwam dat de nauwkeurigheid van 'steady-state' en tijdsafhankelijke temperatuur simulaties vergelijkbaar was. De nauwkeurigheid van temperatuur simulaties gebaseerd op patiënt specifieke weefseleigenschappen was beter dan wanneer je patiënt groep weefseleigenschappen gebruikt. In deze studie tonen we dus aan dat je met patiënt specifieke temperatuur simulaties in combinatie met reconstructie van weefseleigenschappen vanuit gemeten temperaturen een nauwkeurige tool hebt voor minimaal invasieve 3D dosimetrie tijdens hyperthermie behandelingen, want de T50 in behandel sessies zonder invasieve metingen kunnen worden voorspeld met een gemiddelde nauwkeurigheid van 0.4°C. Met de huidige beschikbare data en huidige nauwkeurigheid van andere technieken[75,81,87], is dit de beste nauwkeurigheid die je kunt behalen voor HH hyperthermie behandelingen.

PhD portfolio

Summary of PhD training and teaching activities

Name PhD Student: R.F. Verhaart	PhD period: November 2010 - May 2015	
ErasmusMC Department: Radiation Oncology	Promotor: Prof. dr. G.C. van Rhoon	
Research School: Postgraduate School Molecular Medicine	Supervisor: Dr. Ir. M.M. Paulides	

	Year	Workload
1. PhD training		
General academical skills		
- PhD day	2011	0.2 ECTS
- Biomedical English Writing and Communication	2013	4.0 ECTS
- MolMed Presenting Course	2013	1.0 ECTS
- Presentation and voice training	2014	0.7 ECTS
Research skills		
- MRI safety	2012	0.2 ECTS
- Course Scientific Integrity	2014	0.2 ECTS
In-depth courses		
- MolMed Course	2011	0.7 ECTS
- Basic Electromagnetism	2011	3.0 ECTS
- MRI in Radiotherapy	2011	2.5 ECTS
- Current Concepts in Spin Labeling and Contrast Enhanced Perfusion MRI	2011	0.7 ECTS
Presentations		
- Energy loss at rest and in exercise condition in patient specific Fontan geometries	2010	0.2 ECTS
- Hyperthermia treatment planning for head and neck cancer: improving patient models using advanced MRI characteristics	2011	0.2 ECTS
- Patient Modeling for head and neck deep hyperthermia	2012	0.2 ECTS
- MRI for Hyperthermia: a literature overview	2012	0.2 ECTS
- Towards accurate segmentation for planning-guided hyperthermia treatment of head and neck cancer	2012	0.2 ECTS
- Computed Tomography Based Delineation Variation and the Influence on the Planned Head and Neck Hyperthermia Treatment Dose	2013	0.2 ECTS
- Magnetic Resonance Imaging: Basic Principle and Applications for Hyperthermia	2013	0.2 ECTS
- CT Based Delineation Variation and the Influence on the Planned Head and Neck Hyperthermia Dose	2013	0.2 ECTS
- MR perfusion	2013	0.2 ECTS
- Dynamic-contrast-enhanced MR imaging:a phantom for offline parameter optimization and quality assurance	2014	0.2 ECTS
- Accuracy of 3D temperature simulations during a hyperthermia treatment in the head and neck region	2014	0.2 ECTS
- Verbeteren van hyperthermie behandel planning voor hoofd-hals tumoren met behulp van MRI	2014	0.2 ECTS
International conferences		
- The 16th Molecular Medicine Day, Rotterdam, the Netherlands	2012	0.2 ECTS
- The 11th International Congress of Hyperthermic Oncology (ICHO), The 29th Japanese Congress of Thermal Medicine, Kyoto, Japan	2012	1.4 ECTS
- The 29th Annual Scientific Meeting of the European Society for Magnetic Resonance in Medicine and Biology (ESMRMB), Lisbon, Portugal.	2012	1.4 ECTS
- The 2nd Daniel den Hoed Day, Rotterdam, the Netherlands	2013	0.2 ECTS

Continued from previous page
Summary of PhD training and teaching activities

	Year	Workload
- The 4th Dutch Bio-Medical Engineering Conference, Egmond aan Zee, the Netherlands	2013	0.4 ECTS
- The 28th Annual Meeting of the European Society for Hyperthermic Oncology (ESHO), Munich, Germany	2013	1.4 ECTS
- The 33th Annual meeting of the European Society for Radiotherapy and Oncology (ESTRO), Vienna, Austria	2014	1.4 ECTS
- The 29th Annual meeting of the European Society for Hyperthermic Oncology (ESHO), Torino, Italy	2014	0.2 ECTS
Workload: 1. PhD training		**22.2 ECTS**
2. Teaching activities		
Lecturing		
- MRI for Hyperthermia (education for technicians, physicians and physicists)	2013	0.2 ECTS
- Head and Neck Hyperthermia Treatment Planning (education for Electrical Engineering students from Eindhoven University of Technology (TU/e))	2013	0.2 ECTS
- Thermal property optimization (education for technicians, physicians and physicists)	2014	0.2 ECTS
Supervising		
- M. Garcia , Bachelor graduation project, MBRT Fontys Eindhoven	2011-2012	3 ECTS
- I. Wijdeven, Bachelor graduation project, MBRT Fontys Eindhoven	2011-2012	3 ECTS
- S. Overbeek, Bachelor graduation project, MBRT Fontys Eindhoven	2011-2012	3 ECTS
- A.H.W. van den Berg, Bachelor graduation project, MBRT Fontys Eindhoven	2012-2013	3 ECTS
- L. Bouwmans, Bachelor graduation project, MBRT Fontys Eindhoven	2012-2013	3 ECTS
- T.S. van Bastelaar, Bachelor graduation project, MBRT Fontys Eindhoven	2012-2013	3 ECTS
- L.R.S. Verbeek, Bachelor internship project, Health Engineering Hogeschool Rotterdam	2013-2014	3 ECTS
- I. Wijdeven, Volunteer work	2013-2014	1 ECTS
Workload: 2. Teaching activities		**22.6 ECTS**
Total Workload		**44.8 ECTS**

Publications

Publications in international journals

- **RF Verhaart**, V Fortunati, GM Verduijn, T van Walsum, JF Veenland, MM Paulides, "CT-Based Patient Modeling for Head and Neck Hyperthermia Treatment Planning: Manual versus Automatic Normal-Tissue Segmentation", *Radiother Oncol*, Vol. 111, No. 1, pp. 158-163, 2014.

- **RF Verhaart**, V Fortunati, GM Verduijn, A van der Lugt, T van Walsum, JF Veenland, MM Paulides, "The relevance of MRI for patient modeling in head and neck hyperthermia treatment planning: a comparison of CT and CT-MRI based tissue segmentation on simulated temperature", *Med Phys*, Vol. 41, No. 12, pp. 123302, 2014.

- **RF Verhaart**, Z Rijnen, V Fortunati, GM Verduijn, T van Walsum, JF Veenland, MM Paulides, "Temperature simulations in hyperthermia treatment planning of the head and neck region: rigorous optimization of tissue properties", *Strahlenther Onkol*, Vol. 190, No. 12, pp. 1117-1124, 2014.

- **RF Verhaart**, GM Verduijn, V Fortunati, Z Rijnen, T van Walsum, JF Veenland, MM Paulides, "Accurate 3D temperature dosimetry during hyperthermia therapy by combining invasive measurements and patient-specific simulations", *Int J Hyperthermia*, Vol. 31, No. 6, pp. 686-692, 2015 (Yamamoto-Taylor and Francis Editors Award Int J Hyperthermia for best Physics/Engineering Paper 2015).

- V Fortunati, **RF Verhaart**, F van der Lijn, WJ Niessen, JF Veenland, MM Paulides, T van Walsum, "Tissue segmentation of head and neck CT images for treatment planning: a multiatlas approach combined with intensity modeling", *Med Phys*, Vol. 40, No. 7, 071905, 2013.

- V Fortunati, **RF Verhaart**, F Angeloni, A van der Lugt, WJ Niessen, JF Veenland, MM Paulides, T van Walsum, "Feasibility of multimodal deformable registration for head and neck tumor treatment planning", *Int J Radiat Oncol Biol Phys*, Vol. 90, No. 1, pp. 85-93, 2014.

- V Fortunati, **RF Verhaart**, GM Verduijn, A van der Lugt, F Angeloni, WJ Niessen, JF Veenland, MM Paulides, T van Walsum, "MRI integration into treatment planning of head and neck tumors: Can patient immobilization be avoided?", *Radiother Oncol*, Vol. 115, No. 2, pp. 191-194, 2015.

- V Fortunati, **RF Verhaart**, WJ Niessen, JF Veenland, MM Paulides, T van Walsum, "Automatic tissue segmentation of head and neck MR images for hyperthermia treatment planning", *Phys Med Biol*, Vol. 60, No. 16, pp. 6547-6562, 2015.

- F Adibzadeh, **RF Verhaart**, GM Verduijn, V Fortunati, Z Rijnen, M Franckena, GC van Rhoon, MM Paulides, " Association of acute adverse effects with high local SAR induced in the brain from prolonged RF head and neck hyperthermia", *Phys Med Biol*, Vol. 60, No. 3, pp. 995-1006, 2015.

- F Adibzadeh, JF Bakker, MM Paulides, **RF Verhaart**, GC van Rhoon, "Impact of head morphology on local brain specific absorption rate from exposure to mobile phone radiation", *Bioelectromagnetics*, Vol. 36, No. 1, pp. 66-76, 2014.

- P Togni, Z Rijnen, WC Numan, **RF Verhaart**, JF Bakker, GC van Rhoon, MM Paulides, "Electromagnetic redesign of the HYPERcollar applicator: toward improved deep local head-and-neck hyperthermia", *Phys Med Biol*, Vol. 58, No. 17, pp. 5997-6009, 2013.

- SS Bossers, M Cibis, FJ Gijsen, M Schokking, JL Strengers, **RF Verhaart**, A Moelker, JJ Wentzel, WA Helbing, "Computational fluid dynamics in Fontan patients to evaluate power loss during simulated exercise", *Heart*, Vol. 100, No. 9, pp. 696-701, 2014.

- MR Tarasek, R Pellicer, LW Hofstetter, WC Numan, JF Bakker, G Kotek, P Togni, **RF Verhaart**, EW Fiveland, GC Houston, GC van Rhoon, MM Paulides, DT Yeo, "Validation of MR thermometry: method for temperature probe sensor registration accuracy in head and neck phantoms.", *Int J Hyperthermia*, Vol. 30, No. 2, pp. 142-149, 2014.

Publications in international conference proceedings

- V Fortunati, **RF Verhaart**, F van der Lijn, WJ Niessen, JF Veenland, MM Paulides, T van Walsum, "Hyperthermia critical tissues automatic segmentation of head and neck CT images using atlas registration and graph cuts", *Proceedings of international symposium on biomedical imaging (ISBI): from nano to macro*, 2012.

Conference abstracts

- **RF Verhaart**, V Fortunati, T van Walsum, JF Veenland, A van der Lugt, GC van Rhoon, WJ Niessen, MM Paulides, "Accurate Patient Modeling for Planning-Guided Deep Head and Neck Hyperthermia: Variation in Tissue Delineation", 16th Molecular Medicine Day, February 29, 2012, Rotterdam, the Netherlands. (Poster)

- **R.F. Verhaart**, JJ Bluemink, JF Bakker, P Togni, AJE Raaijmakers, GC van Rhoon, CAT van den Berg, MM Paulides, "Hybrid head and neck hyperthermia and 7T MR imaging: a pilot study", The 11th International congress of hyperthermic oncology (ICHO), The 29th Japanese congress of thermal medicine, August 28-31, 2012, Kyoto, Japan (Poster)

- **RF Verhaart**, JJ Bluemink, JF Bakker, P Togni, AJE Raaijmakers, GC van Rhoon, CAT van den Berg, MM Paulides, "Validation of the predicted B1+ of a radio-frequency hyperthermia applicator using a 7T MR scanner", European Society for Magnetic Resonance in Medicine and Biology (ESMRMB), 29th Annual Scientific Meeting, October 4-6, 2012, Lisbon, Portugal. (Poster + Poster highlight session presentation)

- **RF Verhaart**, V Fortunati, JF Veenland, T van Walsum, WJ Niessen, GC van Rhoon, MM Paulides, "Sensitivity of head and neck hyperthermia treatment planning to observer variations in 3D patient model generation", 4th Dutch Bio-Medical Engineering Conference 2013, Egmond aan Zee, the Netherlands (Poster)

- **RF Verhaart**, GM van de Velde-Verduijn, V Fortunati, GC van Rhoon, JF Veenland, MM Paulides, "Importance of Bone Segmentation for head and neck hyperthermia treatment planning", 28th Annual Meeting of the European Society for Hyperthermic Oncology (ESHO), 2013, Munich, Germany (Poster)

- **RF Verhaart**, V Fortunati, GM van de Velde-Verduijn, T van Walsum, JF Veenland, MM Paulides, "Automatic generation of 3D patient models for real-time simulation guided head and neck hyperthermia", 2nd Daniel den Hoed Day 2013, Rotterdam, the Netherlands (Presentation)

- **RF Verhaart**, V Fortunati, F Adibzadeh, GM Verduijn, JF Veenland, T van Walsum, MM Paulides, "Patient modelling in head and neck hyperthermia treatment planning: is CT-based auto-segmentation sufficient?", 33th Annual meeting of the European society for radiotherapy and oncology (ESTRO 33) 2014, Vienna, Austria. (Young Scientist Poster Session)

- **RF Verhaart**, R Pellicer, A van der Lugt, MM Paulides, G Kotek, "Dynamic contrast enhanced MR imaging: a phantom for offline parameter optimization and quality assurance", 33th Annual meeting of the European society for radiotherapy and oncology (ESTRO 33) 2014, Vienna, Austria. (Presentation)

- **RF Verhaart**, Z Rijnen, V Fortunati, GM Verduijn, T van Walsum, JF Veenland, MM Paulides, "Towards temperature-based hyperthermia treatment planning: a technique for tissue property optimization and its robustness for probe-location", 29th Annual meeting of the European Society for hyperthermic Oncology (ESHO) 2014, Torino, Italy. (Poster)

- V Fortunati, **RF Verhaart**, WJ Niessen, GC van Rhoon, JF Veenland, MM Paulides, T van Walsum, "Automatic 3D patient model generation for head and neck hyperthermia treatment planning", 28th Annual Meeting of the European Society for Hyperthermic Oncology (ESHO), 2013, Munich, Germany.

- V Fortunati, **RF Verhaart**, WJ Niessen, JF Veenland, MM Paulides, T van Walsum, "Critical tissue segmentation of head and neck CT images for hyperthermia treatment planning", 4th Dutch Bio-Medical Engineering Conference 2013, Egmond aan Zee, the Netherlands.

- V Fortunati, **RF Verhaart**, F Angeloni, WJ Niessen, A van der Lugt, JF Veenland, MM Paulides, T van Walsum, "Rigid and non-rigid registration for integrated MR and CT-based head and neck radiotherapy and hyperthermia treatment planning",

European Society for Magnetic Resonance in Medicine and Biology (ESMRMB), 29th Annual Scientific Meeting, October 4-6, 2012, Lisbon, Portugal.

- V Fortunati **RF Verhaart**, F Angeloni, A van der Lugt, WJ Niessen, JF Veenland, MM Paulides, T van Walsum, "MRI integration into treatment planning of the head and neck: can we avoid patient immobilization?", 33th Annual meeting of the European society for radiotherapy and oncology (ESTRO 33) 2014, Vienna, Austria.

- CAT van den Berg, JJ Bluemink, ALHMW van Lier, MM Paulides, JF Bakker, **RF Verhaart**, JJW Lagendijk, FFJ Simonis, A Raaijmakers, "MR and hyperthermia", European microwave week, Amsterdam, The Netherlands, 2012.

Awards

- **RF Verhaart** Young Investigator Travel Award for the contribution "Hybrid head and neck hyperthermia and 7T MR imaging: a pilot study" to The 11th International congress of hyperthermic oncology, The 29th Japanese congress of thermal medicine, August 28-31, 2012, Kyoto, Japan.

- Yamamoto-Taylor and Francis Editors Award Int J Hyperthermia for best Physics/Engineering Paper 2015 for the following international journal publication: **RF Verhaart**, GM Verduijn, V Fortunati, Z Rijnen, T van Walsum, JF Veenland, MM Paulides, "Accurate 3D temperature dosimetry during hyperthermia therapy by combining invasive measurements and patient-specific simulations", *Int J Hyperthermia*, Vol. 31, No. 6, pp. 686-692, 2015.

Curriculum Vitae

Renatus Franciscus Verhaart was born on August 17, 1987 in Rockanje, The Netherlands.

- 1991-1999: Primary school, Kennedy School, Fijnaart, The Netherlands.

- 1999-2005: Secondary school, Norbertus College, Roosendaal, The Netherlands.

- 2005-2008: Bachelor in BioMedical Engineering, Eindhoven University of Technology, The Netherlands.

- 2008-2010: Master of Medical Engineering, Eindhoven University of Technology, The Netherlands.

- 2010-2015: PhD student at Erasmus MC - Cancer Institute, Rotterdam, The Netherlands.

- 2015-...: Trainee Medical Informatics at Maasstad Hospital, Rotterdam, The Netherlands.

Dankwoord

Zo, ik ben erg blij dat je nu het resultaat vast hebt van een aantal jaren hard werken als onderzoeker in opleiding bij de hyperthermie unit van het ErasmusMC. Ook al staat mijn naam op de voorkant van dit boekje, ik heb dit werk natuurlijk niet helemaal alleen gedaan. Daarom wil ik iedereen die een bijdrage (groot of klein) heeft geleverd heel erg hartelijk danken. Ik verontschuldig mij alvast voor de mensen die ik vergeten ben hieronder te benoemen, maar in het bijzonder wil ik onderstaande mensen bedanken.

Als eerste wil ik iedereen bij de hyperthermie unit bedanken voor de leuke en leerzame tijd. Uiteraard Gerard, Prof. van Rhoon, je enthousiasme voor elektromagnetisme en hyperthermie was een erg goede stimulans voor mijn onderzoek. Jij maakt de hyperthermie groep tot de groep die het is: een fijne, gezellige club dat soms echt aanvoelde als een tweede familie. En natuurlijk Maarten, je bent een fijne co-promotor, altijd in voor discussie, je bent een perfectionist als het op het schrijven van papers aankomt en door je goede visie wist je me de goede kant op te sturen. Tomas, Wouter, Zef, Fatemeh, Jurriaan, Richard, Paolo, Roel, Citlalli, en Daniel ik zal de koffiepauzes, lunch bij de donnerzaak en de borrels bij Locus-Publicus missen. Astrid en Sandra, jullie bedankt voor de hulp bij al mijn (praktische) vragen. En als laatste Cobi, Marianne, Netteke, Ali, Heleen, Pia, Greta, Aleida, Audrey, bedankt voor jullie uitleg van de klinische werkwijze en ik hoop dat jullie de tools die ontwikkeld zijn goed kunnen gebruiken in de praktijk!

During my project I worked in close collaboration with the biomedical imaging group rotterdam (BIGR) part of Erasmus MC. Special thanks to Jifke, Theo and Valerio. Jifke you are a real researcher, very accurately checking the details of my results and always giving positive feedback. I also want to thank you for being part of the committee during my defense. Theo, you contributed a lot with your knowledge and ideas during project meetings and provided good feedback on the papers. Valerio, we did most of the work together. I admire your (italian) passion and you are a very hard worker. We started this project almost at the same time, and now, as a paranympf, we will also complete it together. Grazie!

Graag bedank ik ook Prof. Dr. Heijmen, Prof. Dr. van der Lugt, Prof. Dr. Raaymakers, Prof. Dr. Moonen en Prof. Dr. Martens omdat ze zitting willen nemen in de commissie en mijn proefschrift beoordelen.

Als laatste wil ik uiteraard ook mijn familie bedanken: Pa, Ma, Rob (ik vind het leuk dat je mijn paranimf bent!), Rosana, Peter, Lian, bedankt voor alle leuke afleidingen en uitjes (oa. natuurlijk naar Zoutelande) waardoor ik even niet met mijn promotie bezig hoefde te zijn. En Sanne, jij hebt misschien wel het meeste afgezien en ik denk dat jij waarschijnlijk net zo blij bent met dit resultaat als ik. Bedankt!

René Verhaart
Steenbergen, Juni 2016

References

1. Globocan 2012: Estimated cancer incidence, mortality, and prevalence worldwide in 2012. Accessed 13-12-2015. URL http://globocan.iarc.fr/Pages/fact_sheets_population.aspx.

2. Nederlandse kankerregistratie. Accessed 13-12-2015. URL http://www.cijfersoverkanker.nl/.

3. World health organization: The top 10 causes of death. Accessed 13-12-2015. URL http://www.who.int/mediacentre/factsheets/fs297/en/.

4. F Adibzadeh, RF Verhaart, GM Verduijn, V Fortunati, Z Rijnen, M Franckena, GC van Rhoon, and MM Paulides. Association of acute adverse effects with high local SAR induced in the brain from prolonged RF head and neck hyperthermia. *Phys Med Biol*, 60(3):995–1006, 2015.

5. M Ahmed, M Schmidt, A Sohaib, C Kong, K Burke, C Richardson, M Usher, S Brennan, A Riddell, M Davies, K. Newbold, KJ Harrington, and CM Nutting. The value of magnetic resonance imaging in target volume delineation of base of tongue tumours–a study using flexible surface coils. *Radiother Oncol*, 94(2):161–167, 2010.

6. M Amichetti, M Romano, L Busana, A Bolner, G Fellin, G Pani, L Tomio, and R Valdagni. Hyperfractionated radiation in combination with local hyperthermia in the treatment of advanced squamous cell carcinoma of the head and neck: a phase I-II study. *Radiother Oncol*, 45(2):155–158, 1997.

7. JF Bakker, MM Paulides, A Christ, N Kuster, and GC van Rhoon. Assessment of induced SAR in children exposed to electromagnetic plane waves between 10 MHz and 5.6 GHz. *Phys Med Biol*, 55(11):3115–3130, 2010.

8. JF Bakker, MM Paulides, E Neufeld, A Christ, N Kuster, and GC van Rhoon. Children and adults exposed to electromagnetic fields at the ICNIRP reference levels: theoretical assessment of the induced peak temperature increase. *Phys Med Biol*, 56 (15):4967–4989, 2011.

9. E Balidemaj, CAT van den Berg, J Trinks, ALHMW van Lier, AJ Nederveen, LJA Stalpers, H Crezee, and RF Remis. CSI-EPT: A contrast source inversion approach for improved MRI-based electric properties tomography. *IEEE Trans Med Imaging*, 34(9):1788–1796, 2015.

10. E Balidemaj, ALHMW van Lier, H Crezee, AJ Nederveen, LJA Stalpers, and CAT van den Berg. Feasibility of electric property tomography of pelvic tumors at 3T. *Magn Reson Med*, 73(4):1505–1513, 2015.

11. JWJ Bergs, PM Krawczyk, T Borovski, R ten Cate, HM Rodermond, J Stap, JP Medema, J Haveman, J Essers, C van Bree, LJA Stalpers, R Kanaar, JA Aten, and NAP Franken. Inhibition of homologous recombination by hyperthermia shunts early

double strand break repair to non-homologous end-joining. *DNA Repair (Amst)*, 12 (1):38–45, 2013.

12. CL Brouwer, RJHM Steenbakkers, A Navran, and HP Bijl. 3D variation in delineation of head and neck organs at risk. *Radiother Oncol*, 13:7–32, 2012.

13. EC Burdette, PG Friederich, RL Seaman, and LE Larsen. In situ permittivity of canine brain: Regional variations and postmortem changes. *IEEE Transactions on Microwave Theory and Techniques*, 34(1):38–50, 1986.

14. RAM Canters, M Franckena, MM Paulides, and GC Van Rhoon. Patient positioning in deep hyperthermia: influences of inaccuracies, signal correction possibilities and optimization potential. *Phys Med Biol*, 54(12):3923–3936, 2009.

15. RAM Canters, MM Paulides, MF Franckena, J van der Zee, and GC van Rhoon. Implementation of treatment planning in the routine clinical procedure of regional hyperthermia treatment of cervical cancer: an overview and the Rotterdam experience. *Int J Hyperthermia*, 28(6):570–581, 2012.

16. RAM Canters, MM Paulides, M Franckena, JW Mens, and GC van Rhoon. Benefit of replacing the sigma-60 by the sigma-eye applicator. a monte carlo-based uncertainty analysis. *Strahlenther Onkol*, 189(1):74–80, 2013.

17. CA Cocosco, AP Zijdenbos, and AC Evans. A fully automatic and robust brain MRI tissue classification method. *Med Image Anal*, 7(4):513–527, 2003.

18. BA Conley. Treatment of advanced head and neck cancer: what lessons have we learned? *J Clin Oncol*, 24(7):1023–1025, 2006.

19. OI Craciunescu, SK Das, RL McCauley, JR MacFall, and TV Samulski. 3D numerical reconstruction of the hyperthermia induced temperature distribution in human sarcomas using DE-MRI measured tissue perfusion: validation against non-invasive MR temperature measurements. *Int J Hyperthermia*, 17(3):221–239, 2001.

20. OI Craciunescu, BW Raaymakers, AN Kotte, SK Das, TV Samulski, and JJ Lagendijk. Discretizing large traceable vessels and using DE-MRI perfusion maps yields numerical temperature contours that match the MR noninvasive measurements. *Med Phys*, 28(11):2289–2296, 2001.

21. OI Craciunescu, PR Stauffer, BJ Soher, CR Wyatt, O Arabe, P Maccarini, SK Das, K Cheng, TZ Wong, EL Jones, MW Dewhirst, Z Vujaskovic, and JR MacFall. Accuracy of real time noninvasive temperature measurements using magnetic resonance thermal imaging in patients treated for high grade extremity soft tissue sarcomas. *Med Phys*, 36(11):4848–4858, 2009.

22. S Crijns and B Raaymakers. From static to dynamic 1.5T MRI-linac prototype: impact of gantry position related magnetic field variation on image fidelity. *Phys Med Biol*, 59(13):3241–3247, 2014.

23. NR Datta, AK Bose, HK Kapoor, and S Gupta. Head and neck cancers: results of thermoradiotherapy versus radiotherapy. *Int J Hyperthermia*, 6(3):479–486, 1990.

24. NR Datta, SG Ordóñez, US Gaipl, MM Paulides, H Crezee, J Gellermann, D Marder, E Puric, and S Bodis. Local hyperthermia combined with radiotherapy and-/or chemotherapy: Recent advances and promises for the future. *Cancer Treat Rev*, 41 (9):742–753, 2015.

25. R de Boer, HA Vrooman, F van der Lijn, MW Vernooij, MA Ikram, A van der Lugt, MMB Breteler, and WJ Niessen. White matter lesion extension to automatic brain tissue segmentation on MRI. *Neuroimage*, 45(4):1151–1161, 2009.

26. M de Bruijne, DHM Wielheesen, J van der Zee, N Chavannes, and GC van Rhoon. Benefit of superficial hyperthermia treatment planning: five case studies. *Int J Hyperthermia*, 23(5):417–429, 2007.

27. M de Greef, HP Kok, D Correia, A Bel, and J Crezee. Optimization in hyperthermia treatment planning: the impact of tissue perfusion uncertainty. *Med Phys*, 37(9): 4540–4550, 2010.

28. M de Greef, HP Kok, D Correia, P Borsboom, A Bel, and J Crezee. Uncertainty in hyperthermia treatment planning: the need for robust system design. *Phys Med Biol*, 56(11):3233–3250, 2011.

29. WC Dewey. Arrhenius relationships from the molecule and cell to the clinic. *Int J Hyperthermia*, 25(1):3–20, 2009.

30. LR Dice. Measures of the amount of ecologic association between species. *Ecology*, 26(3):297–302, 1945.

31. M Dubuisson and AK Jain. A modified Hausdorff distance for object matching. *Proc. International Conference on Pattern Recognition*, 1:566–568, 1994.

32. B Emami, A Sethi, and GJ Petruzzelli. Influence of MRI on target volume delineation and IMRT planning in nasopharyngeal carcinoma. *Int J Radiat Oncol Biol Phys*, 57 (2):481–488, 2003.

33. P Farace, R Pontalti, L Cristoforetti, R Antolini, and M Scarpa. An automated method for mapping human tissue permittivities by MRI in hyperthermia treatment planning. *Phys Med Biol*, 42(11):2159–2174, 1997.

34. V Fortunati, RF Verhaart, F van der Lijn, WJ Niessen, JF Veenland, MM Paulides, and T van Walsum. Tissue segmentation of head and neck CT images for treatment planning: a multiatlas approach combined with intensity modeling. *Med Phys*, 40 (7), 2013.

35. V Fortunati, RF Verhaart, F Angeloni, A van der Lugt, WJ Niessen, JF Veenland, MM Paulides, and T van Walsum. Feasibility of multi-modal deformable registration for head and neck tumor treatment planning. *Int. J. Radiation Oncology Biol. Phys*, 90(1):85–93, 2014.

36. V Fortunati, RF Verhaart, WJ Niessen, JF Veenland, MM Paulides, and T van Walsum. Automatic tissue segmentation of head and neck MR images for hyperthermia treatment planning. *Phys Med Biol*, 60(16):6547–6562, 2015.

37. M Franckena, LJA Stalpers, PCM Koper, RGJ Wiggenraad, WJ Hoogenraad, Jan DP van Dijk, CC Wárlám-Rodenhuis, JJ Jobsen, GC van Rhoon, and J van der Zee. Long-term improvement in treatment outcome after radiotherapy and hyperthermia in locoregionally advanced cervix cancer: an update of the Dutch Deep Hyperthermia Trial. *Int J Radiat Oncol Biol Phys*, 70(4):1176–1182, 2008.

38. M Franckena, D Fatehi, M de Bruijne, RAM Canters, Y van Norden, J Mens, GC van Rhoon, and J van der Zee. Hyperthermia dose-effect relationship in 420 patients with cervical cancer treated with combined radiotherapy and hyperthermia. *Eur J Cancer*, 45(11):1969–1978, 2009.

39. C Gabriel and A Peyman. Dielectric measurement: error analysis and assessment of uncertainty. *Phys Med Biol*, 51(23):6033–6046, 2006.

40. S Gabriel, RW Lau, and C Gabriel. The dielectric properties of biological tissues: III. Parametric models for the dielectric spectrum of tissues. *Phys Med Biol*, 41(11): 2271–2293, 1996.

41. S Gabriel, RW Lau, and C Gabriel. The dielectric properties of biological tissues: II. Measurements in the frequency range 10 Hz to 20 GHz. *Phys Med Biol*, 41(11): 2251–2269, 1996.

42. X Geets, J Daisne, S Arcangeli, E Coche, M De Poel, T Duprez, G Nardella, and V Grégoire. Inter-observer variability in the delineation of pharyngo-laryngeal tumor, parotid glands and cervical spinal cord: comparison between CT-scan and MRI. *Radiother Oncol*, 77(1):25–31, 2005.

43. J Gellermann, P Wust, D Stalling, M Seebass, J Nadobny, R Beck, H Hege, P Deufl-hard, and R Felix. Clinical evaluation and verification of the hyperthermia treatment planning system hyperplan. *Int J Radiat Oncol Biol Phys*, 47(4):1145–1156, 2000.

44. J Gellermann, W Wlodarczyk, A Feussner, H Fhling, J Nadobny, B Hildebrandt, R Felix, and P Wust. Methods and potentials of magnetic resonance imaging for monitoring radiofrequency hyperthermia in a hybrid system. *Int J Hyperthermia*, 21 (6):497–513, 2005.

45. J Gellermann, B Hildebrandt, R Issels, H Ganter, W Wlodarczyk, V Budach, R Felix, P Tunn, P Reichardt, and P Wust. Noninvasive magnetic resonance thermography of soft tissue sarcomas during regional hyperthermia: correlation with response and direct thermometry. *Cancer*, 107(6):1373–1382, 2006.

46. AR Gordon, LA Loevner, A Shukla-Dave, RO Redfern, AI Sonners, AM Kilger, MA Elliott, M Machtay, RS Weber, JD Glickson, and DI Rosenthal. Intraobserver variability in the MR determination of tumor volume in squamous cell carcinoma of the pharynx. *AJNR Am J Neuroradiol*, 25(6):1092–1098, 2004.

47. PA Hasgall, E Neufeld, MC Gosselin, A Klingenböck, and N Kuster. ITIS database for thermal and electromagnetic parameters of biological tissues, July 30th 2013. URL www.itis.ethz.ch/database.

48. J Haveman, P Sminia, J Wondergem, J van der Zee, and MCCM Hulshof. Effects of hyperthermia on the central nervous system: what was learnt from animal studies? *Int J Hyperthermia*, 21(5):473–487, 2005.

49. M Hofer. *CT Teaching Manual: A Systematic Approach to CT Reading*. Thieme, 3th edition, Stuttgard edition, 2007.

50. MR Horsman. Angiogenesis and vascular targeting: relevance for hyperthermia. *Int J Hyperthermia*, 24(1):57–65, 2008.

51. Y Hua, S Ma, Z Fu, Q Hu, L Wang, and Y Piao. Intracavity hyperthermia in nasopharyngeal cancer: a phase III clinical study. *Int J Hyperthermia*, 27(2):180–186, 2011.

52. NG Huilgol, S Gupta, and R Dixit. Chemoradiation with hyperthermia in the treatment of head and neck cancer. *Int J Hyperthermia*, 26(1):21–25, 2010.

53. NG Huilgol, S Gupta, and SR Sridhar. Hypertheria with radiation in the treatment of locally advanced head and neck cancer: a report of randomized trial. *Journal of Cancer Research and Therapeutics*, 6(4):492–496, 2010.

54. RD Issels. Hyperthermia adds to chemotherapy. *Eur J Cancer*, 44(17):2546–2554, 2008.

55. RK Jain, FH Grantham, and PM Gullino. Blood flow and heat transfer in walker 256 mammary carcinoma. *J Natl Cancer Inst*, 62(4):927–933, 1979.

56. WT Joines, Y Zhang, C Li, and RL Jirtle. The measured electrical properties of normal and malignant human tissues from 50 to 900 MHz. *Med Phys*, 21(4):547–550, 1994.

57. EL Jones, JR Oleson, LR Prosnitz, TV Samulski, Z Vujaskovic, D Yu, LL Sanders, and MW Dewhirst. Randomized trial of hyperthermia and radiation for superficial tumors. *J Clin Oncol*, 23(13):3079–3085, 2005.

58. HH Kampinga. Cell biological effects of hyperthermia alone or combined with radiation or drugs: a short introduction to newcomers in the field. *Int J Hyperthermia*, 22(3):191–196, 2006.

59. M Knudsen and L Heinzl. Two-point control of temperature profile in tissue. *Int J Hyperthermia*, 2(1):21–38, 1986.

60. HP Kok, PMA van Haaren, JB van de Kamer, and J Crezee. Theoretical comparison of intraluminal heating techniques. *Int J Hyperthermia*, 23(4):395–411, 2007.

61. HP Kok, J Gellermann, CAT van den Berg, PR Stauffer, JW Hand, and J Crezee. Thermal modelling using discrete vasculature for thermal therapy: A review. *Int J Hyperthermia*, 29(4):336–345, 2013.

62. HP Kok, CAT van den Berg, A Bel, and J Crezee. Fast thermal simulations and temperature optimization for hyperthermia treatment planning, including realistic 3D vessel networks. *Med Phys*, 40(10):103303, 2013.

63. AN Kotte, G van Leeuwen, J de Bree, J van der Koijk, H Crezee, and J Lagendijk. A description of discrete vessel segments in thermal modelling of tissues. *Phys Med Biol*, 41(5):865–884, 1996.

64. AN Kotte, GM van Leeuwen, and JJ Lagendijk. Modelling the thermal impact of a discrete vessel tree. *Phys Med Biol*, 44(1):57–74, 1999.

65. PM Krawczyk, B Eppink, J Essers, J Stap, H Rodermond, H Odijk, A Zelensky, C van Bree, LJ Stalpers, MR Buist, T Soullié, J Rens, HJM Verhagen, MJ O'Connor, NAP Franken, TLM Ten Hagen, R Kanaar, and JA Aten. Mild hyperthermia inhibits homologous recombination, induces BRCA2 degradation, and sensitizes cancer cells to poly (ADP-ribose) polymerase-1 inhibition. *Proc Natl Acad Sci U S A*, 108(24): 9851–9856, 2011.

66. JC Lagarias, JA Reeds, MH Wright, and PE Wright. Convergence properties of the nelder-mead simplex method in low dimensions. *SIAM J Optim*, 9(1):112–147, 1998.

67. JJ Lagendijk. Hyperthermia treatment planning. *Phys Med Biol*, 45(5):R61–R76, 2000.

68. PC Levendag, DN Teguh, P Voet, H van der Est, I Noever, WJM de Kruijf, I Kolkman-Deurloo, J Prevost, J Poll, PIM Schmitz, and BJ Heijmen. Dysphagia disorders in patients with cancer of the oropharynx are significantly affected by the radiation therapy dose to the superior and middle constrictor muscle: a dose-effect relationship. *Radiother Oncol*, 85(1):64–73, 2007.

69. M Linthorst, T Drizdal, H Joosten, GC van Rhoon, and J van der Zee. Procedure for creating a three-dimensional (3D) model for superficial hyperthermia treatment planning. *Strahlenther Onkol*, 187(12):835–841, 2011.

70. JH Machiels, LF Licitra, RI Haddad, M Tahara, and EE Cohen. Rationale and design of LUX-head & neck 1: a randomised, phase III trial of afatinib versus methotrexate in patients with recurrent and/or metastatic head and neck squamous cell carcinoma who progressed after platinum-based therapy. *BMC Cancer*, 14:473, 2014.

71. M Mazzurana, L Sandrini, A Vaccari, C Malacarne, L Cristoforetti, and R Pontalti. A semi-automatic method for developing an anthropomorphic numerical model of dielectric anatomy by MRI. *Phys Med Biol*, 48(19):3157–3170, 2003.

72. RL Mcintosh. A comprehensive tissue propperties database provided for the thermal assessment of a human at rest. *Biophysical Reviews and Letters*, 5(3):129–151, 2010.

73. M Murbach, E Neufeld, W Kainz, KP Pruessmann, and N Kuster. Whole-body and local RF absorption in human models as a function of anatomy and position within 1.5T MR body coil. *Magn Reson Med*, 71(2):839–845, 2014.

74. BE Nelms, WA Tom, G Robinson, and J Wheeler. Variations in the contouring of organs at risk: test case from a patient with oropharyngeal cancer. *Int J Radiat Oncol Biol Phys*, 82(1):368–378, 2012.

75. WCM Numan, LW Hofstetter, G Kotek, JF Bakker, EW Fiveland, GC Houston, G Kudielka, DTB Yeo, and MM Paulides. Exploration of MR-guided head and neck hyperthermia by phantom testing of a modified prototype applicator for use with proton resonance frequency shift thermometry. *Int J Hyperthermia*, 30(3):184–191, 2014.

76. J Olesen and OB Paulson. The effect of intra-arterial papaverine on the regional cerebral blood flow in patients with stroke or intracranial tumor. *Stroke*, 2(2):148–159, 1971.

77. MM Paulides, DHM Wielheesen, J Van der Zee, and GC Van Rhoon. Assessment of the local SAR distortion by major anatomical structures in a cylindrical neck phantom. *Int J Hyperthermia*, 21(2):125–140, 2005.

78. MM Paulides, JF Bakker, E Neufeld, J van der Zee, PP Jansen, PC Levendag, and GC van Rhoon. The HYPERcollar: a novel applicator for hyperthermia in the head and neck. *Int J Hyperthermia*, 23(7):567–576, 2007.

79. MM Paulides, JF Bakker, M Linthorst, J van der Zee, Z Rijnen, E Neufeld, PMT Pattynama, PP Jansen, PC Levendag, and GC van Rhoon. The clinical feasibility of deep hyperthermia treatment in the head and neck: new challenges for positioning and temperature measurement. *Phys Med Biol*, 55(9):2465–2480, 2010.

80. MM Paulides, PR Stauffer, E Neufeld, PF Maccarini, A Kyriakou, RAM Canters, CJ Diederich, JF Bakker, and GC Van Rhoon. Simulation techniques in hyperthermia treatment planning. *Int J Hyperthermia*, 29(4):346–357, 2013.

81. MM Paulides, JF Bakker, LW Hofstetter, WCM Numan, R Pellicer, EW Fiveland, M Tarasek, GC Houston, GC van Rhoon, DTB Yeo, and G Kotek. Laboratory prototype for experimental validation of MR-guided radiofrequency head and neck hyperthermia. *Phys Med Biol*, 59(9):2139–2154, 2014.

82. HH Pennes. Analysis of tissue and arterial blood temperatures in the resting human forearm. *J Appl Physiol*, 1(2):93–122, 1948.

83. A Peyman and C Gabriel. Cole-Cole parameters for the dielectric properties of porcine tissues as a function of age at microwave frequencies. *Phys Med Biol*, 55 (15):N413–N419, 2010.

84. A Peyman, C Gabriel, EH Grant, G Vermeeren, and L Martens. Variation of the dielectric properties of tissues with age: the effect on the values of SAR in children when exposed to walkie-talkie devices. *Phys Med Biol*, 54(2):227–241, 2009.

85. M Prishvin, R Zaridze, G Bit-Babik, and A Faraone. Improved numerical modelling of heat transfer in human tissue exposed to RF energy. *Australas Phys Eng Sci Med*, 33(4):307–317, 2010.

86. BW Raaymakers, AN Kotte, and JJ Lagendijk. How to apply a discrete vessel model in thermal simulations when only incomplete vessel data are available. *Phys Med Biol*, 45(11):3385–3401, 2000.

87. BW Raaymakers, M Van Vulpen, JJ Lagendijk, AA De Leeuw, J Crezee, and JJ Battermann. Determination and validation of the actual 3D temperature distribution during interstitial hyperthermia of prostate carcinoma. *Phys Med Biol*, 46(12):3115–3131, 2001.

88. CRN Rasch, RJHM Steenbakkers, I Fitton, JC Duppen, PJCM Nowak, FA Pameijer, A Eisbruch, JHAM Kaanders, F Paulsen, and M van Herk. Decreased 3D observer variation with matched CT-MRI, for target delineation in nasopharynx cancer. *Radiat Oncol*, 5(21):1–8, 2010.

89. Z Rijnen, JF Bakker, RAM Canters, P Togni, GM Verduijn, PC Levendag, GC Van Rhoon, and MM Paulides. Clinical integration of software tool VEDO for adaptive and quantitative application of phased array hyperthermia in the head and neck. *Int J Hyperthermia*, 29(3):181–193, 2013.

90. Z Rijnen, P Togni, R Roskam, SG van de Geer, RHM Goossens, and MM Paulides. Quality and comfort in head and neck hyperthermia: A redesign according to clinical experience and simulation studies. *Int J Hyperthermia*, 31(8):823–830, 2015.

91. RB Roemer, AM Fletcher, and TC Cetas. Obtaining local SAR and blood perfusion data from temperature measurements: steady state and transient techniques compared. *Int J Radiat Oncol Biol Phys*, 11(8):1539–1550, 1985.

92. G Schmid and R Uberbacher. Age dependence of dielectric properties of bovine brain and ocular tissues in the frequency range of 400 MHz to 18 GHz. *Phys Med Biol*, 50(19):4711–4720, 2005.

93. G Schmid, G Neubauer, UM Illievich, and F Alesch. Dielectric properties of porcine brain tissue in the transition from life to death at frequencies from 800 to 1900 MHz. *Bioelectromagnetics*, 24(6):413–422, 2003.

94. M Sherar, FF Liu, M Pintilie, W Levin, J Hunt, R Hill, J Hand, C Vernon, GC van Rhoon, J van der Zee, DG González González, J van Dijk, J Whaley, and D Machin. Relationship between thermal dose and outcome in thermoradiotherapy treatments for superficial recurrences of breast cancer: data from a phase III trial. *Int J Radiat Oncol Biol Phys*, 39(2):371–380, 1997.

95. G Sreenivasa, J Gellermann, B Rau, J Nadobny, P Schlag, P Deuflhard, R Felix, and P Wust. Clinical use of the hyperthermia treatment planning system HyperPlan to predict effectiveness and toxicity. *Int J Radiat Oncol Biol Phys*, 55(2):407–419, 2003.

96. VL Stakhursky, O Arabe, K Cheng, J Macfall, P Maccarini, O Craciunescu, M Dewhirst, P Stauffer, and SK Das. Real-time MRI-guided hyperthermia treatment using a fast adaptive algorithm. *Phys Med Biol*, 54(7):2131–2145, 2009.

97. B Taylor and C Kuyatt. *Guidelines for evaluating and expressing the uncertainty of NIST measurement results*. NIST Technical Note 1297, 1994.

98. A Thiagarajan, N Caria, H Schder, NG Iyer, S Wolden, RJ Wong, E Sherman, MG Fury, and N Lee. Target volume delineation in oropharyngeal cancer: impact of PET, MRI, and physical examination. *Int J Radiat Oncol Biol Phys*, 83(1):220–227, 2012.

99. P Togni, Z Rijnen, WCM Numan, RF Verhaart, JF Bakker, GC van Rhoon, and MM Paulides. Electromagnetic redesign of the HYPERcollar applicator: toward improved deep local head-and-neck hyperthermia. *Phys Med Biol*, 58(17):5997–6009, 2013.

100. R Valdagni and M Amichetti. Report of long-term follow-up in a randomized trial comparing radiation therapy and radiation therapy plus hyperthermia to metastatic lymphnodes in stage IV head and neck patients. *Int J Radiat Oncol Biol Phys*, 28 (1):163–169, 1994.

101. JB Van de Kamer, N Van Wieringen, A A De Leeuw, and JJ Lagendijk. The significance of accurate dielectric tissue data for hyperthermia treatment planning. *Int J Hyperthermia*, 17(2):123–142, 2001.

102. ML Van der Gaag, M De Bruijne, T Samaras, J Van der Zee, and GC Van Rhoon. Development of a guideline for the water bolus temperature in superficial hyperthermia. *Int J Hyperthermia*, 22(8):637–656, 2006.

103. J van der Zee, D Gonzlez Gonzlez, GC van Rhoon, JD van Dijk, WL van Putten, and AA Hart. Comparison of radiotherapy alone with radiotherapy plus hyperthermia in locally advanced pelvic tumours: a prospective, randomised, multicentre trial. *Lancet*, 355(9210):1119–1125, 2000.

104. GM Van Leeuwen, AN Kotte, BW Raaymakers, and JJ Lagendijk. Temperature simulations in tissue with a realistic computer generated vessel network. *Phys Med Biol*, 45(4):1035–1049, 2000.

105. GC van Rhoon, T Samaras, PS Yarmolenko, MW Dewhirst, E Neufeld, and N Kuster. CEM43degC thermal dose thresholds: a potential guide for magnetic resonance radio-frequency exposure levels? *Eur Radiol*, 23(8):2215–2227, 2013.

106. RF Verhaart, V Fortunati, GM Verduijn, T van Walsum, JF Veenland, and MM Paulides. CT-based patient modeling for head and neck hyperthermia treatment planning: Manual versus automatic normal-tissue-segmentation. *Radiother Oncol*, 111(1):158–163, 2014.

107. RF Verhaart, Z Rijnen, V Fortunati, GM Verduijn, T van Walsum, JF Veenland, and MM Paulides. Temperature simulations in hyperthermia treatment planning of the head and neck region: rigorous optimization of tissue properties. *Strahlenther Onkol*, 190(12):1117–1124, 2014.

108. FM Waterman, L Tupchong, RE Nerlinger, and J Matthews. Blood flow in human tumors during local hyperthermia. *Int J Radiat Oncol Biol Phys*, 20(6):1255–1262, 1991.

109. F Wilcoxon. Individual comparison by ranking methods. *Biometrics Bulletin*, 1(6):80–83, 1945.

110. P Wust, J Nadobny, M Seebass, D Stalling, J Gellermann, HC Hege, P Deuflhard, and R Felix. Influence of patient models and numerical methods on predicted power deposition patterns. *Int J Hyperthermia*, 15(6):519–540, 1999.

111. P Wust, B Hildebrandt, G Sreenivasa, B Rau, J Gellermann, H Riess, R Felix, and PM Schlag. Hyperthermia in combined treatment of cancer. *Lancet Oncol*, 3(8):487–497, 2002.

112. PA Yushkevich, J Piven, HC Hazlett, RG Smith, S Ho, JC Gee, and G Gerig. User-guided 3D active contour segmentation of anatomical structures: significantly improved efficiency and reliability. *Neuroimage*, 31(3):1116–1128, 2006.

113. C Zhao, J Chen, B Yu, and X Chen. Improvement in quality of life in patients with nasopharyngeal carcinoma treated with non-invasive extracorporeal radiofrequency in combination with chemoradiotherapy. *Int J Radiat Biol*, 90(10):853–858, 2014.